

ABSTRACT

Title of Document: EXPERIMENTAL STUDY OF CAPILLARY-
FED ENHANCED-SURFACE TUBULAR
EVAPORATORS -- APPLICATIONS TO LOW
GRADE THERMAL ENERGY CONVERSION

Joshua Matthew Fody
Master of Science in Mechanical Engineering
2013

Directed By: Dr. Michael Ohadi
Professor of Mechanical Engineering

A novel capillary feed concept was developed for deployment on an enhanced tubular evaporator intended for low grade thermal energy conversion applications. The concept was applied to both vertical and horizontal evaporator orientations. The capillary feed mechanism was developed, and research was conducted using this feed on closed loop single tube evaporators using anhydrous ammonia. A 2" one foot long proof of concept evaporator was tested along with two different 3/4" five foot long (half-length) aluminum tubes. The target test LMTD was around 2 [K]. Results varied with test conditions, enhancement geometry, refrigerant flow rate, and evaporator orientation. Heat transfer performance of the evaporator, as well as water and refrigerant flow rates and pressure drops are assessed. Test operational

constraints and uncertainty limitations are investigated. The capillary feed mechanism advantages and limitations are surveyed, and future works are recommended along with discussions about relevant operational considerations.

EXPERIMENTAL STUDY OF CAPILLARY-FED ENHANCED-SURFACE
TUBULAR EVAPORATORS -- APPLICATIONS TO LOW GRADE THERMAL
ENERGY CONVERSION.

By

Joshua Matthew Fody

Thesis submitted to the Faculty of the Graduate School of the
University of Maryland, College Park in partial fulfillment
of the requirements for the degree of
Master of Science
2013

Advisory Committee:

Professor Michael Ohadi, Chair

Dr. Marino di Marzo

Dr. Amir Riaz

© Copyright by
Joshua Matthew Fody
2013

Dedication

To my friends for all of their companionship.

To my family for all of their support and love.

To my wife for all of the above.

Acknowledgements

There were significant contributions from many people in my life who made this work possible. First, my advisor, Dr. Michael Ohadi, generously supported me throughout the years that I spent working in his lab, and helped me to make the unusual transition from an undergraduate degree in psychology to engineering graduate school. I also received significant support in many forms from many of my family members and friends. Without this support, it simply would not have been possible for me to complete my studies. Also, I would like to thank the Abel Foundation and OTEC International, LLC for their sponsorship of this research. Their financial support was critical to the realization of this study.

The contributions that Dr. Serguei Dessiatoun has made to my success cannot easily be overstated. He readily shared his considerable knowledge and experience at every opportunity. He was a constant source of motivation and a pleasure to work with. His generosity has been humbling. Over the past four years he has been my supervisor, my mentor, and I am proud to call him my friend.

Finally, many of my colleagues provided notable contributions to this work. Dr. Amir Shooshtari has an impressive capacity for problem solving and a penchant for computations and technical writing. He never hesitates to make himself available for questions or assistance. Raphael Mandel is a graduate research assistant who is years beyond his position in technical prowess and capability. He contributed directly to several of the correlational and analytical concepts in this work. Many other colleagues contributed knowledge and assistance over the years too numerous to mention specifically. I would like to especially acknowledge, in no particular order, Meera Mahadevan, Rohit Andhare, Jan Muehlbauer, Arjun Sharma, Song Li, and Howard Grossenbacher. Also, thank you to my colleagues who became friends and made coming to work each day a pleasure. I will always fondly remember David Boyea, Bikash Acharya, Vibhash Jha, Ratnesh Tiwari, Justin Di Palo, Valentin Solotych, Edwin Cetegen, Harish Ganapathy, James Daniel Spencer, and Bracha Mandel.

Table of Contents

List of Tables	vii
List of Figures	viii
Nomenclature	xii
List of Abbreviations	xv
Chapter 1: Introduction	1
Low Grade Thermal Energy (LGTE)	1
LGTE Defined:	1
LGTE Applications:	1
LGTE Thermodynamic Design Considerations.....	3
The Organic Rankine Cycle (ORC):	3
Working Fluid Selection:	3
Case Study: Ocean Thermal Energy Conversion (OTEC):	5
Description of the Current Study	7
Research Objectives:.....	7
The Capillary-Fed Enhanced Tubular Evaporator:	8
General Evaporator Design Considerations Specific to LGTE:	8
Current Research Operating Targets and Conditions:	9
Evaporator Design Considerations Specific to This Research:	11
Chapter 2: Literature Review	13
Existing Enhanced Tubular Evaporator Feed Mechanisms	13
Top Performers:	13
Factors Affecting Performance:	16
Capillary Feed/Rising Film:.....	24
Chapter 3: Experimental Methods	26
Summary of Testing.....	26
Vertical Capillary Feed Development Loop	26
Ethanol Test Loop.....	31
Ammonia Integrated Test Loop	35
Ammonia Independent Test Loop	36
2” One Foot Proof of Concept Tube Test Section	41

$\frac{3}{4}$ " Half-length Surfaces Tested	43
Half-length Large Casing Test Section (Vertical Feed)	45
Half-length Small Casing Test Section (Horizontal Feed)	47
General	48
Uncertainty in Results:	48
Wilson Plot:	52
Chapter 4: Experimental Results and Analysis	55
Ethanol Testing	55
Vertical Capillary Feed Design:	55
2" One Foot Proof of Concept Tube:	56
$\frac{3}{4}$ " Half-length Tube Vertical Testing:	57
Ammonia Testing	58
2" One Foot Proof of Concept Tube - Integrated NH ₃ Loop:	58
2" One Foot Proof of Concept Tube – Independent NH ₃ Loop:	59
$\frac{3}{4}$ " Half-length Horizontal Plain Fin – Independent NH ₃ Loop:	62
$\frac{3}{4}$ " Half-length Horizontal ISTF (Small) – Independent NH ₃ Loop:	63
$\frac{3}{4}$ " Half-length Horizontal ISTF (Large) – Independent NH ₃ Loop:	64
$\frac{3}{4}$ " Half-length Vertical ISTF – Independent NH ₃ Loop:	65
Wilson Plot Results:	66
Pressure Drop:	69
Chapter 5: Discussion and Analysis	71
Performance Comparisons	71
Factors in Performance	73
Feed Tubes:	73
LMTD:	74
Refrigerant Flow Rate:	77
Refrigerant Flow Distribution:	84
Water Flow Rate:	84
Correlational Heat Transfer Mode Characterization	88
Chapter 6: Conclusion	94
Chapter 7: Potential Applications and Future Work	98
Applications for the Capillary Feed Concept	98

Future Work Suggestions.....	100
Feed Tube Optimization:	100
Test Casing Variation and Bundle:	101
Additional Surface Geometry Tests:.....	101
Below Nucleate Boiling Application Test:	101
Appendix.....	102
Illustrations	102
Correlational Derivations.....	106
Onset of Nucleate Boiling – Liu (2005):	106
Onset of Nucleate Boiling – Hsu (1962):	107
Onset of Nucleate Boiling – Kandlikar Pool Boiling:	108
Onset of Nucleate Boiling – Kandlikar Flow Boiling:	108
Pool Boiling:	108
Flow Boiling:	111
Thin Film Evaporation:.....	111
Critical Heat Flux.....	114
Works Cited	115

List of Tables

Table 1: ORC working fluid properties [7].....	4
Table 2: Comparison of some candidate ORC working fluid properties [14].....	5
Table 3: OTEC operating targets for the current research using NH ₃	10
Table 4: Actual operating range for current research using NH ₃	10
Table 5: Evaporator conditions specific to the OTEC application	12
Table 6: Abbreviations for literature review delivery mechanisms.....	13
Table 7: Some characteristics of the outlined top results studies.	16
Table 8: Summary of testing.....	26
Table 9: Capillary development loop instrumentation.....	31
Table 10: Ethanol loop instrumentation.....	35
Table 11: Independent loop instrumentation.	40
Table 12: 2" one foot tube and test section critical dimensions.....	43
Table 13: 3/4" Half-length Tube Critical Dimensions.....	43
Table 14: Half-length large casing critical dimensions.	46
Table 15: Half-length small casing critical dimensions.....	48
Table 16: 2" one foot tube with new external outlet separator using ethanol.....	57
Table 17: Configurations tested using the independent ammonia test loop.	59
Table 18: Variables to analyze in a later channel feed optimization study.	74

List of Figures

Figure 1: T-S diagram of steam and some organic working fluids [3]	3
Figure 2: Average annual thermal gradient [K] between 20 and 1000 [m] [10]	6
Figure 3: The OTEC closed cycle (ORC) [7]	7
Figure 4: Illustration of the vertical capillary feed tube concept.	8
Figure 5: Best FF/SF results for Habert (2009) [28].....	14
Figure 6: Top FFM results from Jha (2012) [23].....	15
Figure 7: Top FF/SF results from Moeykens (1994) [15].	16
Figure 8: Pool boiling with single row of Gewa-C +LW [28].....	17
Figure 9: Pool boiling with single row of Turbo-EDE2 [28].....	17
Figure 10: Pool boiling with single row of Gewa-B4 [28].	18
Figure 11: Comparison of single tube performance R134a [46].	19
Figure 12: Comparison of tubes in falling film bundle using R134a (from Moeyken, 1994) [46].....	20
Figure 13: Plain nozzle fed falling film bundle using NH3 [45].	20
Figure 14: Varying nozzle configuration on falling film low fin bundle 25 [kg/min] R134a [15].	21
Figure 15: Description of nozzle configurations for figure above [15].	22
Figure 16: Effect of test rig for bundle vs. single tubes [15].	23
Figure 17: Turbo-B5 falling film single array using R134a, at 5C Tsat, as flow rate varies [25].	23
Figure 18: Results from "rising film" capillary feed using water at 5C Tsat [19].....	24
Figure 19: Results from "rising film" capillary feed as immersion depth is varied [19].	25
Figure 20: Vertical capillary feed development loop schematic	27
Figure 21: Vertical capillary feed development loop. Note open tube configuration.	28
Figure 22: Types of feed mechanisms: Liquid guide (left), wick (center), channel (right).	29
Figure 23: Examples of various feed concepts tested.	29
Figure 24: Half-length 3/4" evaporator and channel feed tube in open test configuration.	30
Figure 25: Ethanol test loop schematic (2" one foot test configuration shown).....	32

Figure 26: Ethanol test loop (3/4" half-length test configuration shown).	33
Figure 27: Ethanol test loop 3/4" half-length liquid inlet/vapor outlet (left) and liquid outlet (right)	34
Figure 28: Ammonia integrated test loop schematic	36
Figure 29: 2" one foot tube in the ammonia integrated test loop configuration, elbow at outlet.....	36
Figure 30: Independent ammonia test loop schematic.....	37
Figure 31: Independent ammonia test loop photograph.	38
Figure 32: Flow visualization window.	39
Figure 33: 2" one foot aluminum tube.	41
Figure 34: 2" one foot test section casing.	42
Figure 35: 2" one foot test section schematic showing capillary feed tube and outlet separator.	42
Figure 36: ISTF surface radial view looking inward.	44
Figure 37: 3/4" ISTF profile with internal rifling visible	44
Figure 38: 3/4" half-length tube external surfacing, plain fin (left) and ISTF (right).	45
Figure 39: Model of the half-length large casing test section inlet.....	46
Figure 40: Illustration of the horizontal feed mechanism [19].	48
Figure 41: An example of a typical T-type thermocouple uncertainty calibration.....	50
Figure 42: A typical example of uncertainty in U and Q.....	51
Figure 43: A typical example of uncertainty in href.	52
Figure 44: Linear relation for Wilson plot using 3/4" half-length tube.	53
Figure 45: A selection of feed tubes tested on the 2" one foot evaporator.	56
Figure 46: Comparison of half-length feed tubes for the 3/4" ISTF evaporator.....	56
Figure 47: Ethanol pre-testing of the half-length vertical tube in the closed configuration.	58
Figure 48: Oscillations in ammonia delivery flow rate due to oversized diaphragm pump and PID control.	59
Figure 49: 2" 1 foot tube independent loop results (oil contaminated).	60
Figure 50: 2" 1 foot tube independent loop results (cleaned).	61
Figure 51: Oil contamination visible on 2" tube surface.	61
Figure 52: Pentane before cleaning independent test loop (left) and after removing oil (right).	62
Figure 53: 3/4" horizontal plain fin (small casing) outlet orientation variation.	63

Figure 54: 3/4" Half-length horizontal plain fin results for side outlet.	63
Figure 55: 3/4" half-length ISTF horizontal small casing results.	64
Figure 56: 3/4" half-length horizontal ISTF large casing results.....	65
Figure 57: 3/4" half-length vertical test results.....	66
Figure 58: Wilson plot results for water side comparing 2" and 3/4" tubes.	67
Figure 59: 3/4" Wilson plot results vs. manufacturer's correlation.	67
Figure 60: 3/4" horizontal half-length plain fin refrigerant side limitation.	68
Figure 61: 3/4" horizontal half-length ISTF refrigerant side limitation.	68
Figure 62: Water side pressure drop for both 2" and 3/4" tubes.....	69
Figure 63: Water side pressure drop measurement validation with manufacturer's correlation.	70
Figure 64: Refrigerant side pressure drop for both half-length feed concepts.	70
Figure 65: Heat transfer results comparing 3/4" tubes using NH3.	71
Figure 66: Overall heat transfer coefficient comparing all tubes using NH3.	72
Figure 67: Refrigerant side heat transfer coefficient comparing all tubes using NH3.	73
Figure 68: 3/4" half-length horizontal ISTF large casing performance with change in LMTD.	75
Figure 69: 3/4" half-length horizontal ISTF small casing performance with change in LMTD.	76
Figure 70: 3/4" half-length vertical tube performance with change in LMTD.....	77
Figure 71: Variation of U as surface-overfeed changes (energy balance method).....	78
Figure 72: Variation of U as surface-overfeed changes (bypass fluid method).	78
Figure 73: Overall heat transfer coefficient vs. overfeed for both horizontal and vertical configurations.	80
Figure 74: Onset of dry out in a falling film tubular bundle [24].	81
Figure 75: Falling film performance as surface overfeed increases [29].....	81
Figure 76: Two phase flow in an enhanced surface using falling film [30].	82
Figure 77: Pool boiling heat transfer as heat flux increases (Webb & Pais 1992) [24].	83
Figure 78: NH3 side performance comparison as delivery rate changes for all tubes.	84
Figure 79: 3/4" half-length tube refrigerant side vs. water side performance (.5 [kg/s] H2O).	85

Figure 80: 2" Vertical tube U vs. water flow rate.	85
Figure 81: 3/4" horizontal plain fin tube U vs. water flow rate.	86
Figure 82: 3/4" horizontal ISTF (small) tube U vs. water flow rate.	87
Figure 83: 3/4" horizontal ISTF (small) contribution to U vs. water flow rate.	87
Figure 84: Illustration of channel dry out caused by bubble nucleation.	88
Figure 85: Onset of nucleate boiling prediction.	89
Figure 86: Onset of nucleate boiling prediction validation.	90
Figure 87: Critical heat flux assessment.	91
Figure 88: Heat transfer regime analysis for horizontal ISTF small casing.	92
Figure 89: Heat transfer regime analysis for horizontal plain fin.	92
Figure 90: Pressure drop and over feed demands on the 3/4" half-length horizontal ISTF (small case) tube.	98
Figure 91: Flow rate in falling film using R134a [29].	99
Figure 92: Falling film over feed requirements for Moeykens' top performer [15]. ..	99
Figure 93: Refrigerant pressure drop for the forced-fed microchannel configuration [23].	100
Figure 94: Large test casing top manifold showing liquid inlet and vapor outlet ports.	102
Figure 95: Large test casing bottom manifold showing bi-pass liquid outlet port. ..	103
Figure 96: Small test casing inlet cross section drawing.	104
Figure 97: Uncertainty propagation for a typical case, independent NH3 loop.	105
Figure 98: h_{ref} for finned and plain tubes is equivalent for 100 [kW/m ²] and .1 [bar] [37].	108
Figure 99: Microchannel thin film profile and dynamics [39].	113

Nomenclature

A_c	Cross sectional area	m^2
A_s	Nominal evaporator surface area	m^2
$A_{s,o}$	Nominal external enhancement evaporator surface area	m^2
$A_{s,i}$	Nominal internal enhancement evaporator surface area	m^2
C_p	Specific heat at constant pressure	$\frac{J}{kgK}$
D	Nominal tube diameter	m
D_h	Hydraulic diameter	m
dP	Differential pressure drop	Pa
EB	Energy balance	%
H_{fin}	Microchannel fin height	m
h_{fg}	Latent heat of vaporization	$\frac{J}{kg}$
h_{ref}	Heat transfer coefficient	$\frac{W}{m^2K}$
Kn	Knudsen number	
k	Thermal conductivity	$\frac{W}{mK}$
L	Evaporator tube length	m
$LMTD$	Log mean temperature difference	K
\dot{m}	Mass flow rate	$\frac{kg}{s}$
Nu	Nusselt number	
P	Pressure	Pa
P_{sat}	Refrigerant saturation pressure	Pa
Pr	Prandtl number	
Q	Total heat transfer	W

q''	Nominal heat flux	$\frac{W}{m^2}$
q''_o	External enhancement evaporator surface heat flux	$\frac{W}{m^2}$
q''_i	Internal enhancement evaporator heat flux	$\frac{W}{m^2}$
r	Radius	m
R	Thermal resistance	$\frac{K}{W}$
Re	Reynolds number	
T	Temperature	C, K
T_c	Condenser inlet temperature	C, K
$T_{c,out}$	Condenser outlet temperature	C, K
T_{sat}	Refrigerant saturation temperature	C, K
T_w	Evaporator inlet temperature	C, K
$T_{w,out}$	Evaporator outlet temperature	C, K
t_{fin}	Microchannel fin thickness	m
u	Average fluid velocity	$\frac{m}{s}$
U	Overall heat transfer coefficient	$\frac{W}{m^2 K}$
W_{chan}	Microchannel width	m
X	Phase quality	

Greek Letters

α	Microchannel aspect ratio	
ϵ	Uncertainty	
λ_{MFP}	Molecular mean free path	m
η	Efficiency	

μ	Dynamic viscosity	$\frac{\text{kg}}{\text{ms}}$
ν	Specific volume	$\frac{\text{m}^3}{\text{kg}}$
ρ	Density	$\frac{\text{kg}}{\text{m}^3}$
σ	Surface Tension	$\frac{\text{N}}{\text{m}}$

Miscellaneous

—	Averaged value
---	----------------

List of Abbreviations

ORC:	Organic Rankine Cycle
LGTE:	Low Grade Thermal Energy
OTEC:	Ocean Thermal Energy Conversion
LMTD:	Log Mean Temperature Difference
NH ₃ :	Anhydrous Ammonia
C ₂ H ₆ O:	Ethanol

Chapter 1: Introduction

Low Grade Thermal Energy (LGTE)

LGTE Defined:

The terms *Low Grade Energy* or *Low Grade Thermal Energy* have been used extensively in literature in recent years; however, these terms are often not well or consistently defined. For the purposes of this study, LGTE will be adapted from an existing definition based on the exergy available for energy conversion [1]. Exergy can be thought of as the maximum amount of theoretical work which can be extracted from the potential energy difference in a system [2]. As it pertains to heat transfer applications, this available energy – which can be converted into mechanical, electrical, or other forms of useful work – exists between two thermal reservoirs. The amount of work which can be extracted from a thermal system is limited by the efficiency of the energy conversion process and the energy difference between the thermal reservoirs. As this research focuses specifically on the subject of the evaporator working within a closed loop, the following definition is used:

“Low grade thermal energy (LGTE) is related to applications where the Log Mean Temperature Difference (LMTD) across an evaporator working in a closed loop is very low, sometimes less than 5 Kelvin”.

LGTE Applications:

In recent years, likely due to rises in energy costs and increased consumption, there has been significant research conducted on developing viable LGTE technologies. By making use of LGTE, existing industrial processes can be made more efficient due to waste heat reclamation, and new alternative energy resources, previously too expensive to harness, can be realized. Some potential sources of LGTE are solar, geothermal, biomass products, naturally occurring thermal gradients (such as those found in ocean or river water), and waste heat from industrial or commercial processes. A natural consequence of LGTE is low overall first and second law thermodynamic efficiencies. For this reason, LGTE represents a niche market for making use of resources where conventional technologies fail. What follows is a brief description of some LGTE applications; much of this material draws heavily from a 2011 review article written by Tchanche, et. al. [3].

Geothermal energy can be harnessed by technologies which make use of the thermal gradient in the earth's crust near the surface. This thermal gradient is not evenly distributed, making some areas more suitable for exploitation than others; however, on average the temperature of the bedrock increases 300 [K/km] with depth. The first working geothermal electrical plant was commissioned in Italy in 1913, but by 2011 there were over 500 producing a combined total of about 10 [GW] of power. Practical resource temperatures for this application range from < 125 – 320 °C, and a

number of cycle designs are available to convert energy depending on local site conditions. The basic binary plant design is best suited to overcome the inefficiencies of the lowest range of available resource temperatures, as it employs a secondary working fluid loop, and is the only viable option for operations below 150 °C. It is also the most common plant type, constituting about 32% by number, but produces only about 4% of all geothermal power due to inherently low thermodynamic cycle efficiencies. As a result, technologies well suited to improve LGTE thermodynamic cycle efficiencies would be able to improve the power output of the most common type of geothermal energy resource.

Solar thermal energy is produced by converting solar energy into usable heat, which drives a secondary mechanical energy conversion system usually resulting in the generation of electrical power. Solar thermal systems can operate at a large range of temperatures, with dish concentrators producing up to 1200 °C, and many LGTE options well below 100 °C. The market on the low end is driven by an increased demand for small modular units which can help combat power distribution issues, make use of lower grade resources (increased geographic range), and provide clean and renewable energy for developing countries. LGTE in the solar thermal world has uses in many areas such as modular solar thermal, solar pond, and solar desalination plants. In 2001, Nguyen et. al. tested a working solar thermal plant, utilizing an organic Rankine cycle, operating at $LMTD < 12$ [K] and producing 1.44 [kW] of electricity. The efficiency of this plant was limited to 4.3%, so better evaporators or other technology which improves this number would result in a more viable implementation to satisfy market demand.

Similar to solar thermal energy, is technology which makes use of naturally occurring solar thermal gradients in ocean or river water. The most common of these concepts is ocean thermal energy conversion (OTEC). OTEC makes use of temperature gradients occurring in tropical ocean waters between the warm surface and cool depths of around 1000 [m]. Like all LGTE applications, the major challenge with OTEC is making useful energy from a small overall temperature gradient with maximum theoretical thermodynamic cycle efficiencies of only 3 – 5%. Highly efficient evaporators and other closed cycle components are a must. OTEC will be covered extensively in a case study detailed in a later section of this writing.

The final LGTE application which will be discussed in this work is waste heat recovery. Contrary to the other applications described above, waste heat recovery targets a market which seeks to increase the energy efficiency of existing processes. Here, overall efficiency is increased by extracting energy from heat which is rejected as a byproduct of an unrelated primary industrial or commercial process. It has been estimated that between 20 – 50% of industrial energy consumption could be targeted for reclamation endeavors. Candidate applications for LGTE technology produce waste heat streams of < 230 °C; examples are cooling water, process steam condensate, and internal combustion engines. Waste heat recovery technology is a well explored market with a variety of existing technologies; however, as with all other LGTE applications, the low end of the thermal spectrum yields conventional

technologies too inefficient for practical use and highly efficient cycles which are still capable of producing meaningful power are seeing increased demand.

LGTE Thermodynamic Design Considerations

The Organic Rankine Cycle (ORC):

Several thermodynamic cycles – such as the Rankine cycle, the Super Critical Rankine Cycle, and the Tri-Lateral Cycle – have been analyzed in literature as it pertains to conversion of LGTE into electricity [4]; however, this study specifically assumes the use of a modified ORC. The ORC has been shown to be a highly efficient option for the LGTE operating environment, with thermal efficiencies as high as 10% for applications with only a 45 [K] cycle thermal gradient, and can perform in an environment where conventional cycles are obsolete [5]. Like the standard Rankine cycle, the ORC is a closed loop consisting of four basic components: the evaporator, turbine/expander, condenser, and refrigerant pump. When a proper working fluid is selected, efficiency is limited by the theoretical cycle maximum expressed below.

$$\eta_{ORC} = \frac{Q_{Turbine} - Q_{Pump}}{Q_{Evaporator}}$$

Working Fluid Selection:

The major difference between a Rankine cycle and an ORC is the working fluid. Water has excellent heat transfer properties, and for medium to high grade cycles, water is among the top choices for a working fluid, as shown in Figure 1.

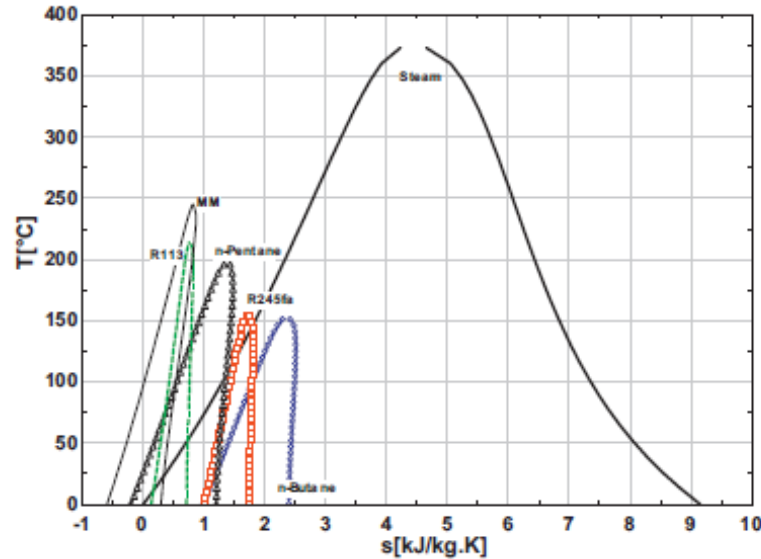


Figure 1: T-S diagram of steam and some organic working fluids [3]

For LGTE cycles, the advantage of water begins to subside due to some other practical problems such as the need to super heat vapor in order to avoid condensation upon expansion, a large amount of heat required for evaporation, high vapor pressure and temperature, expensive and complex turbines, issues with corrosion, and excess pressure in the evaporator [3]. Thus, for LGTE cycles, the ORC is preferred, and different working fluid properties are desired. These properties are listed below in Table 1.

Table 1: ORC working fluid properties [7]

Consideration	Desired for ORC
Toxicity	As low as possible
Chemical Stability	Stable at operating conditions
Boiling Temperature	Should be appropriate to condenser and evaporator set points
Flash Point	A high flash point desired to avoid flammability
Thermodynamics	Vapor saturation curve with zero or positive slope
Latent Heat	High latent heat improves performance
Thermal Conductivity	High thermal conductivity improves heat exchanger performance
Cost/availability	Practical low cost and available working fluid desired
Density/Viscosity	Low vapor and liquid density and viscosity reduce pumping load
Working Pressure	Acceptable evaporation and condensation pressures desired

The working fluid selected for this research was anhydrous ammonia (NH₃); however, many other fluids are acceptable for various LGTE applications using the ORC. Some examples include, but are not limited to, a broad range of hydrocarbons, alcohols, inorganics, and ethers. Ammonia has been shown to be superior for the OTEC LGTE application largely due to its relatively high thermal conductivity [14]. A comparison of important properties of some candidate ORC working fluids is shown in Table 2.

Table 2: Comparison of some candidate ORC working fluid properties [14]

Physical Properties	Ammonia		Propane		R123	
	70°F	50°F	70°F	50°F	70°F	50°F
μ_f (lb _m /hr·ft)	0.341	0.376	0.268	0.298	0.860	0.980
μ_g (lb _m /hr·ft)	0.0268	0.0258	0.021	0.019	0.0278	0.0266
k_f (Btu/hr·ft·°F)	0.2835	0.2982	0.0576	0.0602	0.0378	0.0395
k_g (Btu/hr·ft·°F)	0.0155	0.0140	0.0112	0.0104	0.00588 ^a	0.0055
Cp_f (Btu/lb _m ·°F)	1.128	1.111	0.623	0.603	0.2395	0.2334
Cp_g (Btu/lb _m ·°F)	0.724	0.675	0.498	0.465	0.173	0.168
ρ_f (lb _m /ft ³)	38	39	31.2	32.2	91.6	93.7
ρ_g (lb _m /ft ³)	0.43	0.30	1.17	0.87	0.87	0.61
i_{fg} (Btu/lb _m)	508.6	527.3	145.7	153.2	55.8	57.6
i_{fg}/v_g (Btu/ft ³)	218.7	158.19	170.5	133.3	48.5	35.14
i_f (Btu/lb _m)	120.5	97.9	64.2	51.8	24.4	19.7
i_g (Btu/lb _m)	629.1	625.2	209.9	205	80.3	77.3
α_f (ft ² /hr)	0.00614	0.00688	0.00296	0.00310	0.00172	0.00181
α_g (ft ² /hr)	0.04979	0.06914	0.01922	0.02571	0.03907	0.05367
Pr_f	1.3568	1.4008	2.8987	2.9849	5.4489	5.7907
Pr_g	1.2518	1.2439	0.9337	0.8495	0.8179	0.8125
σ (lb _f /ft)	0.001462	0.001639	0.00046	0.000511	0.000868	0.000962
P_{sat} (psia)	128.80	89.190	124.683	92.185	27.261	18.534
P_{sat} (psig)	114.10	74.500	109.987	77.489	12.561	3.834

Case Study: Ocean Thermal Energy Conversion (OTEC):

The ocean is an enormous solar energy collector and storage medium. With three quarters of the earth's surface covered by ocean, ocean thermal energy is a vast, inexhaustible, and nonpolluting resource which can be used to meet a growing global energy demand, address concerns about climate change, and provide an alternative to rising fossil fuel costs [7]. OTEC creates power by capitalizing on stable thermal gradients in tropical ocean waters. Although much new research and development is being conducted on the subject of OTEC, the fundamental concept is not new.

OTEC was first proposed by French engineer Jacques Arsene d'Arsonval in 1881. His proposed closed cycle plant using NH₃ was never tested; however, nearly 50 years later, his student Georges Claude succeeded in fabricating his design off the coast of Cuba in 1930. This prototype generated about 22 kW of power, but was never able to achieve net positive power production. Later Claude deployed another prototype off the coast of Brazil, but the rig was destroyed by waves. Claude never realized a net positive plant. Other construction, design, and analysis attempts in 1956, the 1960s, and throughout the early 1970s also did not produce a viable result. It wasn't until after the 1973 oil embargo, when the world saw a renewed interest in alternative energy sources, that OTEC first demonstrated real promise. In 1979 a Mini-OTEC plant produced net positive power in Hawaii, and closed cycle heat exchangers were successfully tested the following year in a vessel designated OTEC-1 [7].

The current state of OTEC research and development is vibrant. Literature contains numerous recent publications analyzing OTEC thermodynamic and practical viability and efficiency. In the United States, the Department of Energy (DOE) and the Natural Energy Laboratory of Hawaii Authority (NELHA) publish current opportunities and ventures for OTEC [8, 9]. Elsewhere, a joint venture between Japan and India produced a 1 [MW] plant in 2001, and more projects are scheduled to come online in the Pacific region in coming years [3]. Over 50 Pacific island nations are currently pursuing OTEC as the technology can be used to not only provide inexhaustible power in a region where energy costs are exceptionally high; but, the same resource can be used to simultaneously produce secondary products of regional value such as air conditioning, hydrogen production, and desalinated water [3].

In OTEC, the temperature difference between warm surface water and cool deep water is utilized to drive a modified ORC. Tropical oceans provide the best operating environment for OTEC as they are the locale of large regions of seasonally stable water layers with a temperature difference of around 20 [K] or higher. Figure 2 shows the global OTEC operating environment. Recent research using a 3D general ocean circulation model suggests that approximately 30 TW of potential thermal energy is available in the world's oceans, with at least 7 TW of net OTEC power production possible without adversely affecting the ocean's thermal structure [10]. It is clear that the demand for clean renewable energy will continue to increase in the future, and that the world's oceans contain vast amounts of energy available to meet this demand; therefore, there is an incentive to streamline the OTEC design to ensure competitive power production costs.

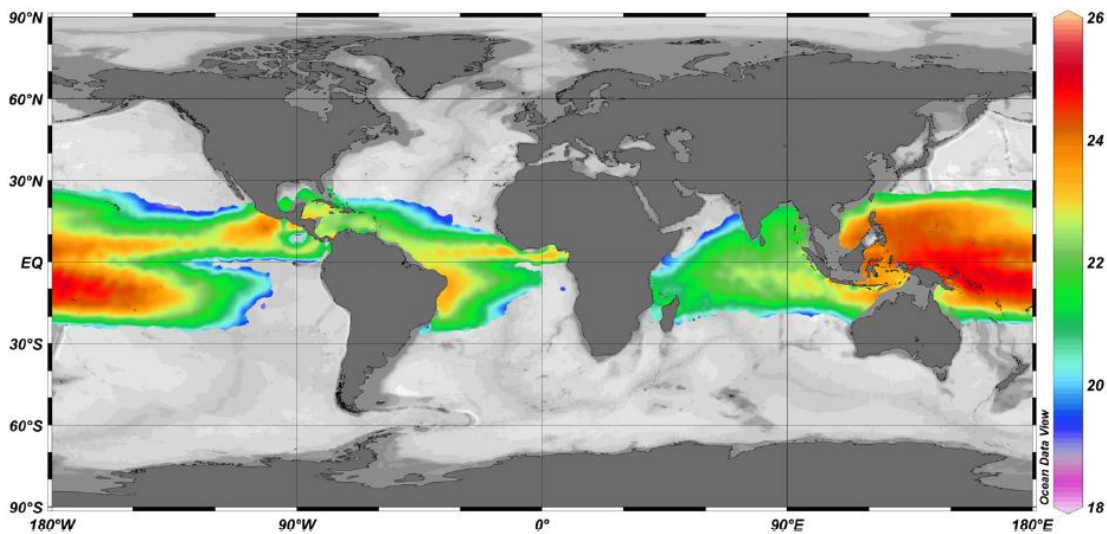


Figure 2: Average annual thermal gradient [K] between 20 and 1000 [m] [10]

Major challenges to designing a cost effective OTEC plant arise from the relatively small overall thermal gradient driving the ORC, as is true with any LGTE application. The most common working fluid in the OTEC application is NH_3 [3, 13]. A schematic of the closed cycle OTEC plant design is found in Figure 3.

Although theoretical maxima for thermodynamic cycle efficiencies are well established, a 1987 paper analyzing the OTEC process asserted that the most accurate practical working limit can be assessed using an irreversible Carnot cycle assuming maximum power production [11]. The resulting simple equation, shown below, estimates a global and seasonal average overall efficiency of about 3.5%.

$$\eta_{OTEC} = 1 - \sqrt{\frac{T_c}{T_w}}$$

Other sources claim 3 – 5% overall efficiency [3, 7]. Such low thermodynamic efficiencies mandate sea water flow rates on the order of several cubic meters per second for every megawatt of power a plant can produce [3, 10]. These high flow rates come at the cost of increased pumping power, and more robust structural components and pipe work. The most effective way to practically mitigate the pumping power issue is to improve the working efficiency of the plant by utilizing highly effective heat exchangers [3]. In fact, the heat exchangers in an OTEC plant have been referred to as a “choke point” in the ORC; and, improvements to the evaporator and condenser performance, such as surface enhancements, have been cited specifically as ways to realize near theoretical maximum plant efficiency [12, 13]. As is specifically relevant to the current research, an effective evaporator surface is imperative in the pursuit to realize viable OTEC and other LGTE technologies.

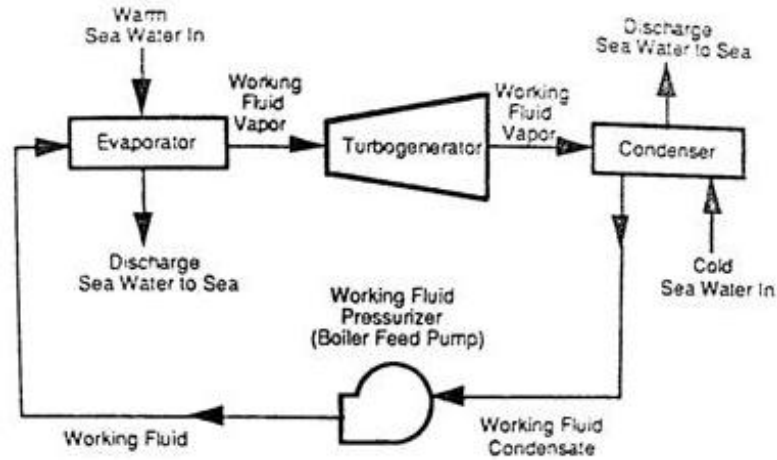


Figure 3: The OTEC closed cycle (ORC) [7]

Description of the Current Study

Research Objectives:

The main objective of this study was to develop and test a novel capillary feed concept for enhanced tubular evaporators operating under OTEC environmental conditions. The capillary feed mechanism was sought out for use in both the horizontal and vertical tubular evaporator orientations. It was necessary for the evaporator to function under very challenging LGTE conditions – the target LMTD

was less than 2 [K] – as a result a high overall heat transfer coefficient was sought with minimal pumping power losses. Two novel capillary feed mechanisms were developed, one for vertical and the other for horizontal, and test results show a proof of concept in performance for both designs. Results were then analyzed, comparisons made for existing alternative technologies applicable to the LGTE market, and future work and other recommendations were given.

The Capillary-Fed Enhanced Tubular Evaporator:

The capillary feed mechanism for the enhanced tubular evaporator is the novel concept on which this research is based. In the most general sense, the capillary feed mechanism simply needs to provide evenly distributed working fluid to the surface of the evaporator. The surface enhancement features induce the capillary wetting; consequently, surface features are required for the capillary feed concept to work. The appropriate microstructure geometry for this concept varies depending on the application and working fluid selected; however, the most important requirement is that the enhancement features are able to adequately supply fluid throughout the surface at the required heat flux without experiencing dry out. The best capillary feed tube design is one which is capable of supplying fluid throughout the surface of the tube and makes the least contact with the evaporator as possible. Minimizing the evaporator surface area contacted by the feed tube maximizes the surface area available for evaporation. Many variables should be accounted for in the design of the capillary feed tube, and are discussed in more detail in the methods section. The vertical feed design is discussed in the section called “Half-length Large Casing Test Section (Vertical Feed)” and the horizontal in “Half-length Small Casing Test Section (Horizontal Feed)”. Figure 4 shows the vertical capillary feed tube design.

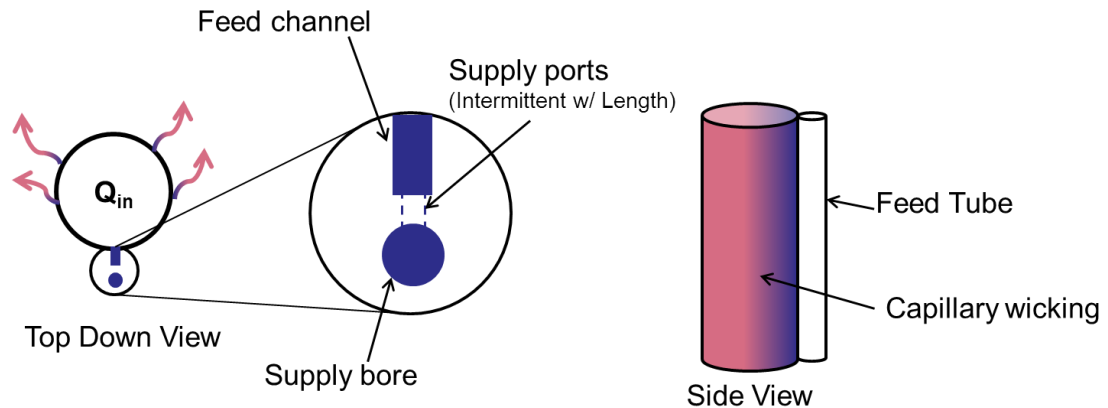


Figure 4: Illustration of the vertical capillary feed tube concept.

General Evaporator Design Considerations Specific to LGTE:

Evaporator design for the LGTE application must address challenges unique to the low heat flux and low LMTD operating environment. Numerous specific considerations may result from these challenges for any given application; however, the most important general factor of top concern for all LGTE evaporator designs is achieving a high overall heat transfer coefficient. Achieving a high overall heat

transfer coefficient increases the meaningful power production of the evaporator by allowing for higher heat flux at a lower pumping power loss. This concept will be discussed now; and, a few additional considerations, specific to the particular evaporator design in this research, are addressed in the following section.

Due to the overall low thermal gradient driving the ORC, the LGTE evaporator must perform well under a low LMTD condition. Practically, the low LMTD condition mandates evaporator designs which exhibit a high overall heat transfer coefficient. This high U value ensures that the evaporator will transfer meaningful energy at the lowest possible flow rates, thus minimizing parasitic pumping power loss. High U values are achieved by decreasing the thermal resistance of the heat supply fluid interface, solid conduction, and working fluid interface of the evaporator. Heat supply fluid, often water, usually transfers heat in the single phase convective mode. In this case, heated side surface enhancements can be highly effective in inducing turbulence and increasing boundary layer mixing, which helps to improve convective heat transfer; however, meaningful decreases on the heat supply fluid thermal resistance are often strongly limited by pumping power losses. Solid conduction through the evaporator surface can be maximized by choosing a highly conductive material, and decreasing the thickness of the solid surfaces. Material compatibility with the adjacent fluids is of concern. Fortunately, conduction resistance through the heat exchanger is usually minimal compared with the convective resistances on either side. Finally, working fluid convective resistance is also important for design efforts to increase the overall U value of the evaporator.

Several factors have a strong effect on the refrigerant side heat transfer performance of the LGTE tubular evaporator. Working fluid selection, refrigerant side surface enhancements, bundle configuration, tube dimensions, fluid delivery rates, and fluid delivery mechanism can all have significant impacts on performance. Currently, the best numbers in literature are reported for falling film tubular bundles which are spray fed using nozzles, and force-fed flow boiling in microchannels. The particular nozzle or manifold configuration, tube dimensions, refrigerant selection, heat flux, and refrigerant flow rate all have effects which can impact the refrigerant side convective resistance considerably [15, 23, 24, 25]. For instances of particularly low LMTD, or when designs require a working fluid which is not likely to experience nucleate boiling during operation, falling film and other boiling dominated fluid delivery configurations are no longer the obvious choice. For these applications, it is best to select a configuration which predominantly relies on thin film evaporation for refrigerant side heat transfer. This is especially true for applications when refrigerant side pumping power losses must be minimal such that single phase convection is not dominant. Configurations which make use of thin film evaporation are likely to deliver the highest refrigerant side heat transfer coefficients for LGTE evaporators when boiling is not possible and refrigerant velocities are low...the ideal application for the capillary feed mechanism.

Current Research Operating Targets and Conditions:

Each individual LGTE evaporator application will have its own unique considerations in addition to achieving a high U value. This section outlines our

current research operating conditions. The goal is to provide some background for the following section which discusses some of the particular challenges which were necessary to address in our design of the evaporator for this study. After some discussion, Table 5 provides a summary of these considerations and our solutions. There was a pre-test design using ethanol, which is not discussed in this section.

Ammonia testing on the capillary fed tubular evaporators for this study was conducted under the constraints which would apply in an OTEC ORC. A summary of operating targets is shown in Table 3. It is important to note that the conditions outlined below are targets for the OTEC application, but in most cases testing was performed on a wider range of conditions so that a more thorough understanding of the performance limitations of the capillary feed technology could be assessed. Table 4 summarizes this wider test range.

Table 3: OTEC operating targets for the current research using NH₃

Constraint Type	Value
Waterside Pressure Drop	$dP_{H_2O} \leq 17.3 \text{ [kPa]}$
Waterside Velocity (Fouling Resistance)	$u \geq 2.2 \left[\frac{m}{s} \right]$
Tube Length	$L \leq 3 \text{ [m]}$
LMTD	1.88 [K]
Chamber NH ₃ Concentration	$\ll 75 \text{ [ppm]}$
Warm Water Temperature	$< 24.9 \text{ [C]}$

For this study, the target test LMTD was 1.88 [K]. LMTD was controlled mostly by manipulating the temperature difference between the condenser and evaporator; however, a secondary control was possible by increasing the evaporator saturation pressure using a vapor outlet valve. Although it would have been desirable to test LMTD values low enough to observe performance before nucleate boiling could occur at target heat fluxes, this data was not able to be collected due to measurement uncertainty. Maximum water flow rate, and consequently heat flux to a large extent, was dictated by the waterside pressure drop constraint of 17.3 [kPa]; although, some testing was performed at higher water flow rates. Minimum water flow rate was constrained by fouling resistance; however, low heat flux and resulting measurement uncertainty ensured that most tests were conducted at the maximum water flow rate. Finally, with the use of NH₃ and sea water, several material compatibility and safety issues were relevant.

Table 4: Actual operating range for current research using NH₃

Constraint Type	Value
-----------------	-------

Waterside Mass Flow Rate	$.33 < \dot{m}_{H_2O} < 1.28 \left[\frac{kg}{s} \right]$
Refrigerant Mass Flow Rate	$.8 < \dot{m}_{NH_3} < 3.25 \left[\frac{kg}{s} \right]$
Tube Length	$L \leq 1.524 [m]$
LMTD	$1.6 < LMTD < 3.6 [K]$
Chamber NH3 Concentration	$\ll 75 [ppm]$
Saturation Temperature	$22.3 < T_{sat} < 27 [C]$

Evaporator Design Considerations Specific to This Research:

In addition to common LGTE design considerations related to increasing the overall U value, there were some issues particular to our application. Working with anhydrous ammonia introduces specific design considerations with respect to the refrigerant side. Anhydrous ammonia is reactive with many materials, many of which are common in the construction of heat exchangers and cooling loops. Copper, which is found in brass, brazing alloys, and is a good conductor, is incompatible with ammonia. Many other materials, including several common plastics, will degrade over time with exposure. As a result, this study utilized heat exchanger surfaces made of aluminum, utilized stainless steel tubing, fittings, and pump parts, and relied on ethylene propylene diene monomer (EPDM) or polytetrafluoroethylene (PTFE also known as Teflon) for seals and other organic parts. Furthermore, anhydrous ammonia has a high vapor pressure at target operating temperatures (1056 [kPa] @ 26.7 [C]). Pressure vessels need to be able to withstand the high pressure, and sealing surfaces need to be precision machined. Anhydrous ammonia vapor is a health hazard and there are regulations which limit the concentration and time of exposure for human beings [16]. For this reason, it is important to keep pressure vessels leak-tight, a formidable task given ammonia's high vapor pressure, small molecular radius (182 pm) [17], and low vapor viscosity ($\approx 9.8E-6$ [kg/ms]).

Finally, there are two maintenance concerns of particular importance on the water side of the OTEC evaporator: fouling and corrosion. Sea water is a particularly corrosive substance. Long term OTEC plant operation success will depend on materials which can withstand the corrosive effects of sea water without significant maintenance costs or safety hazards. In the current study, wetted waterside components were constructed from corrosive resistant stainless steel or aluminum. As it applies to the OTEC plant, aluminum 5052 is a good long term option and it was possible to use in the manufacturing of all tested evaporator geometries. Biological fouling is another water side concern. In many industrial applications, it is common to control bio-fouling by using a biocide such as chlorine [18]; however, although chlorine has been proposed for use with OTEC [22] it is incompatible with ammonia, so fouling in this study had to be controlled by using a waterside velocity constraint instead. This velocity constraint affects the water velocity and internal tube diameter.

Higher water velocity reduces fouling caused by biological growth on heat transfer surfaces [18], but is limited by the pressure drop constraint (pumping power). A larger tube diameter reduces fouling caused by large flow path obstructions, and allows for higher velocities before meeting the pressure drop limit; but it has an adverse impact on the overall heat transfer of the plant due to evaporator tube packing density. As a result, a compromised minimum water velocity constraint and $\frac{3}{4}$ " tubes were implemented in this study. A 2" diameter tube was tested; however, this was as a proof of concept of the vertical capillary feed, and not intended for testing in the OTEC operating conditions.

Table 5: Evaporator conditions specific to the OTEC application

Condition	Consideration	Solutions
Low LMTD (1.88 [K])	Low Heat Transfer Potential	Water-side Surface Enhancements
		Novel Capillary Feed Mechanism
Anhydrous Ammonia	Reactive	Use Al5052, SS316, PTFE, EPDM
	High Vapor Pressure	Compact Pressure Vessels
	Hazardous/Prone to Leaks	Precision Machined Sealing Surfaces Tubular Evaporator – Fewer Seals
Sea Water	Corrosive	Al5052 Evaporator Tubes
	Fouling	Minimum H ₂ O Velocity Constraint $\frac{3}{4}$ " Tube Diameter

Chapter 2: Literature Review

Existing Enhanced Tubular Evaporator Feed Mechanisms

The following sections detail some existing tubular evaporator feed concepts and results. Particular attention was paid to selecting examples which can be applied to the low heat flux LGTE regime. The last section on capillary feed research details some of the differences between the capillary feed and the other concepts. The predominant focus of this section is to survey refrigerant side heat transfer performance whenever possible, as the novel concept in this research is related to refrigerant side delivery. When necessary, delivery mechanism names are abbreviated in this section, and are outlined in Table 1.

Table 6: Abbreviations for literature review delivery mechanisms.

Delivery Mechanism	Abbreviation
Pool Boiling	PB
Falling Film	FF
Spray Feeding	SF
Force Fed Manifold Microchannels	FFM

Top Performers:

Many top performers in literature for LGTE tubular evaporators are configurations which make use of flow boiling. Spray-fed falling film tubular bundles, and manifold force fed microchannels can exhibit very high refrigerant side heat transfer performance.

Habert reported high performance for falling film tests conducted on a Wolverine Turbo-EDE2 horizontal tube bundle Figure 5 [28]. The bundle was spray fed, and R134a was used as the refrigerant. Their lowest tested heat flux performed best; however, this heat flux also exhibited the highest degree of uncertainty in reported results. Habert notes that he can cite no particular reason for the vast difference in performance at the lower tested heat flux, and surmises that performance is very sensitive to certain heat flux and flow conditions.

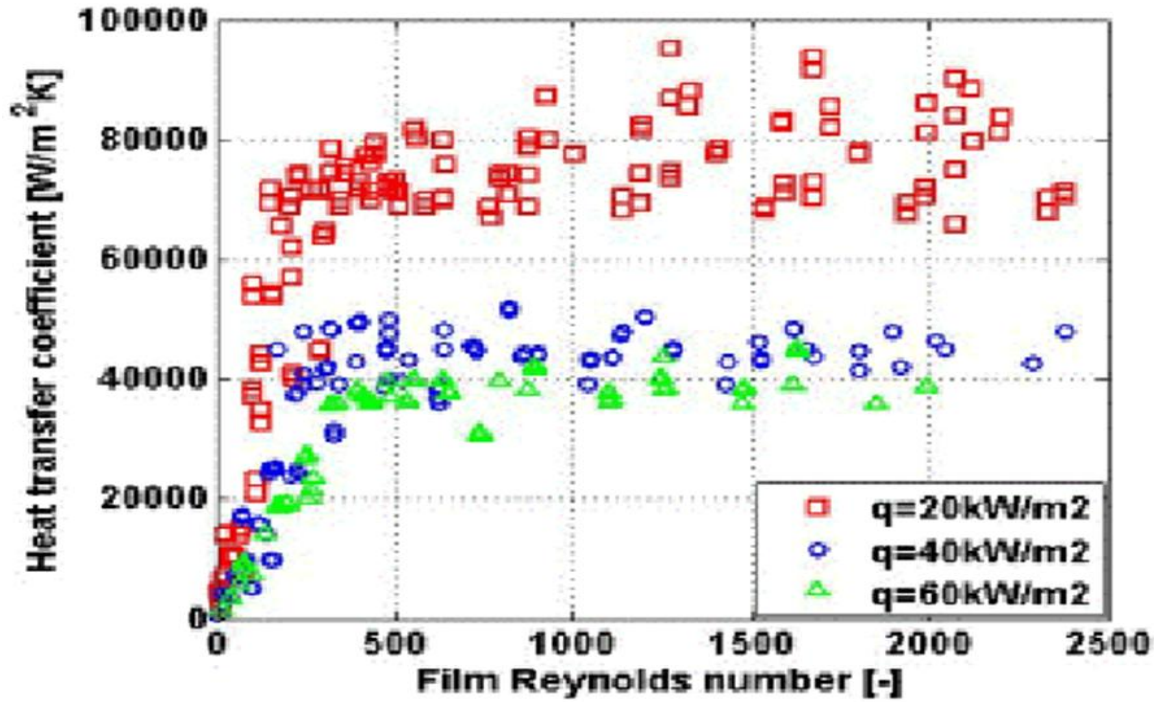


Figure 5: Best FF/SF results for Habert (2009) [28].

Figure 6 shows best performance results from Jha's study on a force fed manifold enhanced tubular evaporator [23]. These best results were achieved for an aluminum tube using R134a. Jha's results were sensitive to the particular geometry of his force fed manifold, and performance was greatly enhanced by the installation of a waterside insert which increased wall velocity on the internal surface of the evaporator.

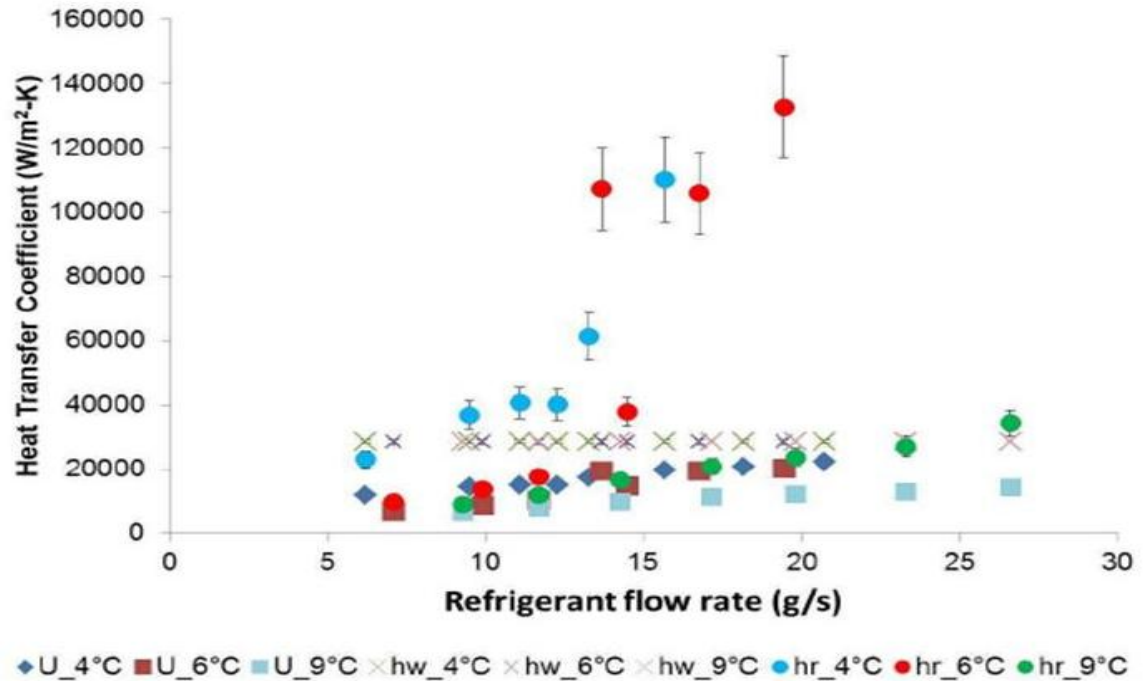


Figure 6: Top FFM results from Jha (2012) [23].

Figure 7 shows top results from Moeykens' 1994 Ph.D thesis [15]. These results were obtained for a bundle of copper evaporator tubes using R134a. The particular spray nozzle configuration had a large impact on Moeykens' results. These tests were conducted using Wolverine Turbo-CII tubes which are designed for use in condensation applications. Moeyken was able to show in his research that these tubes outperformed boiling tubes when used in the falling film application.

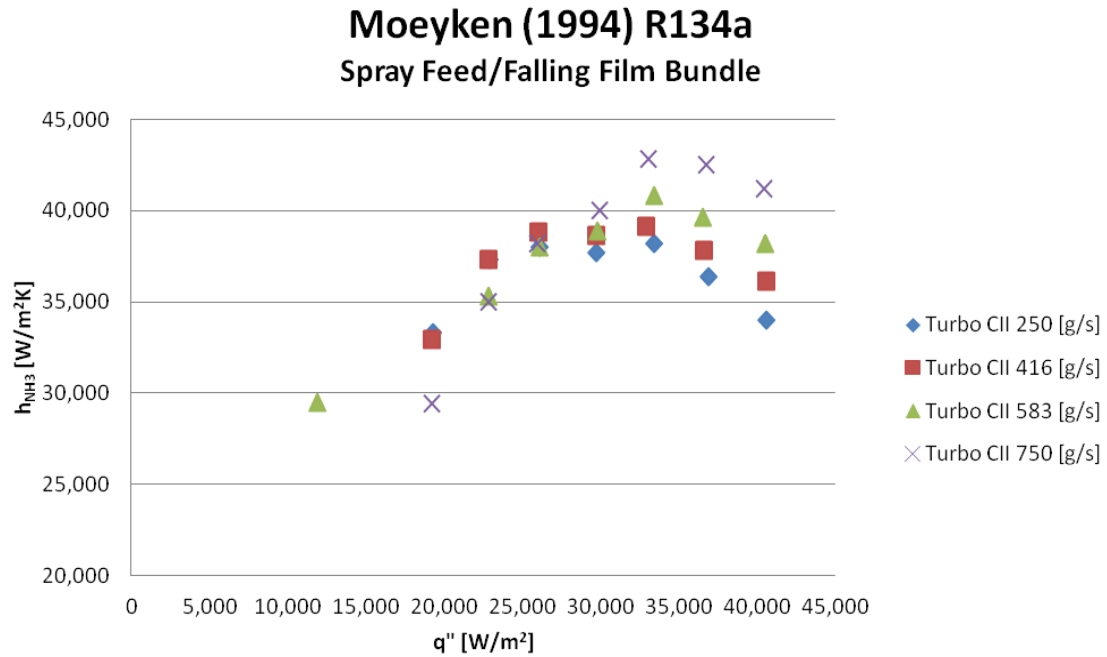


Figure 7: Top FF/SF results from Moeykens (1994) [15].

In all three of these top performing studies, the dominant fluid mode was flow boiling. All of the tests exemplified relatively high refrigerant flow rates, relative to the evaporating heat flux, which enhanced single phase convection and replaced forming bubbles with cool liquid [26]. A summary of some fundamental test characteristics is shown in Table 7.

Table 7: Some characteristics of the outlined top results studies.

	Mode	Fluid	Test	Surface	Dimensions	Ref
Figure 5	FF/SF	R134a	Bundle	Turbo-EDE2	L = .544 D = .0019	[24]
Figure 6	FFM	R134a	Single	212 fins/inch	L = .21 D = .05	[23]
Figure 7	FF/SF	R134a	Bundle	Turbo-CII	L = .394 D = .0019	[15]

Factors Affecting Performance:

Results in literature for LGTE applicable tubular evaporators can vary widely as certain variables change. Identical conditions can yield very different results when the evaporator surface, refrigerant, heat flux, and saturation temperature are varied. This is evident when comparing the results of a pool boiling study conducted on a

single row of $\frac{3}{4}$ " copper evaporator tubes which compared results for R134a and R236fa as saturation temperature and heat flux were parameterized [28]. Figure 8 shows results for the Gewa-C +LW tube, Figure 9 the Turbo-EDE2 (a variation of the boiling Turbo-B2), and Figure 10 for the Gewa-B4.

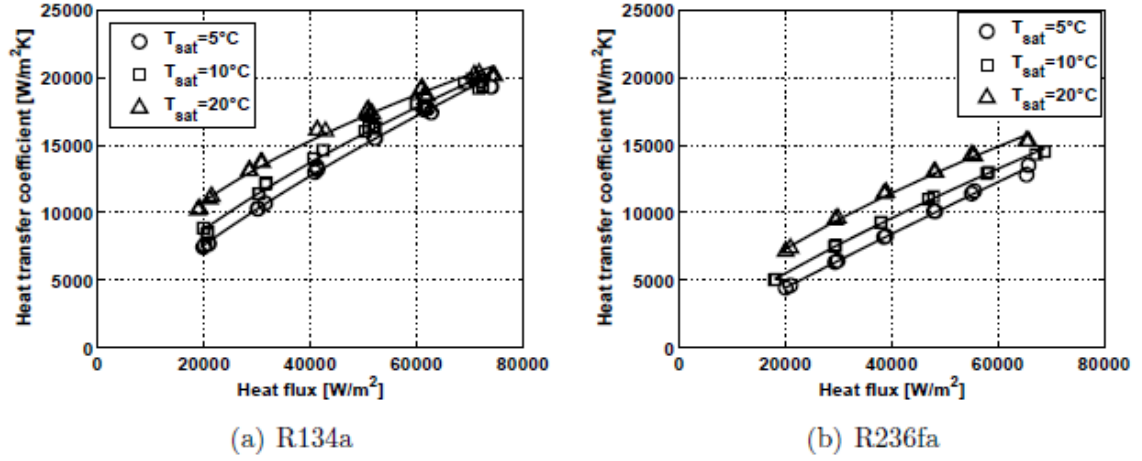


Figure 8: Pool boiling with single row of Gewa-C +LW [28].

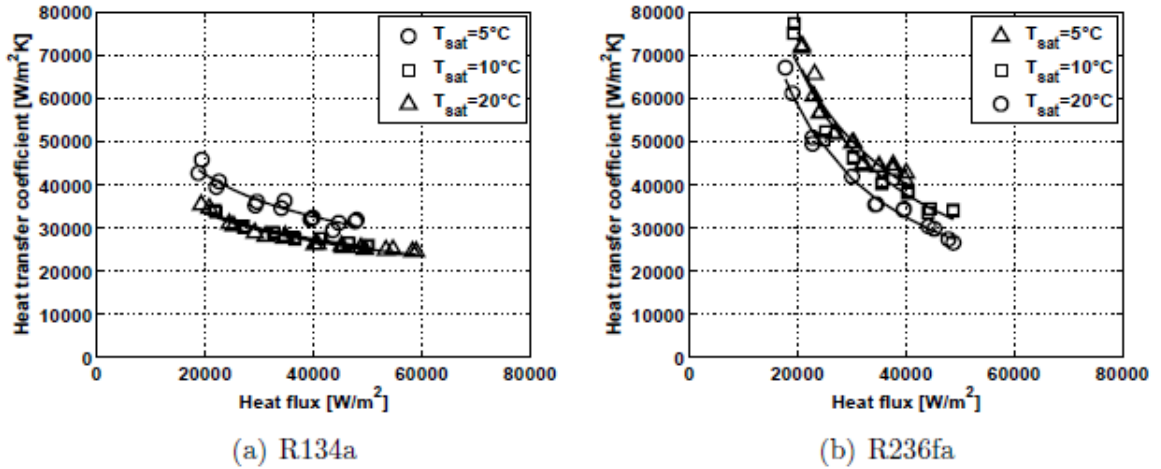


Figure 9: Pool boiling with single row of Turbo-EDE2 [28].

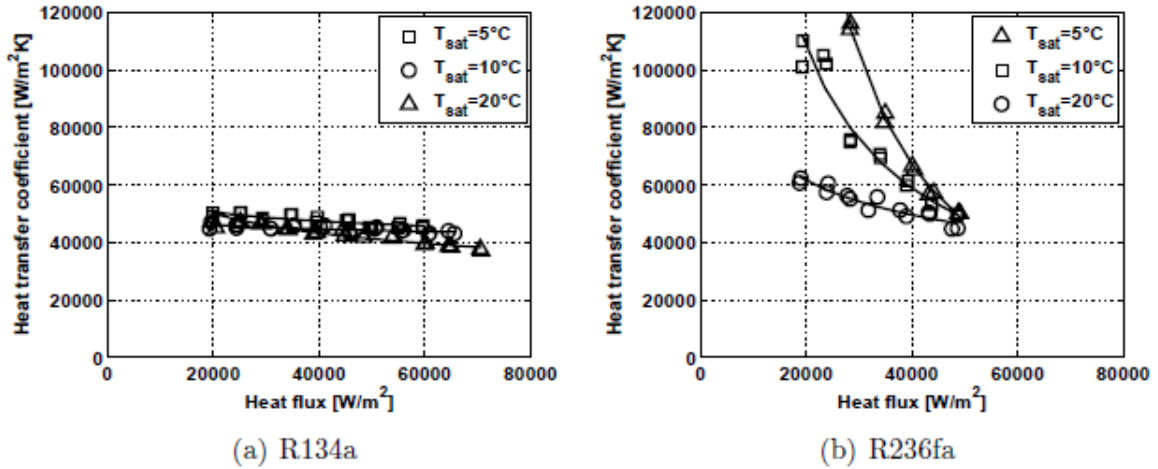


Figure 10: Pool boiling with single row of Gewa-B4 [28].

It is interesting to note that the Turbo-EDE2 and Gewa-B4, both based on the boiling tube format, tended to show decreased performance with increased heat flux. However, the results of these boiling tubes were far better than the Gewa-C +LW tubes, which exhibited an increasing trend in performance with rising heat flux. It is also noteworthy that certain geometry – refrigerant combinations are more sensitive to changes in saturation temperature than others. R134a outperformed R236fa in the Gewa-C +LW bundle, but the opposite was true in the other tubes.

Also, the feed configuration has a significant impact on performance. Figure 11 demonstrates the difference between various tubes tested with falling film compared with pool boiling. The refrigerant used was R134a, and demonstrates a case where performance for the pool boiling mode increases with heat flux. Compare this to Figure 9 where the Turbo-EDE2 has a different trend with heat flux for the same refrigerant as compared with the Turbo-B in the figure below. This is particularly interesting as both tubes are boiling tubes. This difference may be due to flow distribution; the figure above uses a single row of tubes, and the figure below uses only a single tube. It is also interesting to note that, below, increasing heat flux results in higher performance with pool boiling tubes but the enhanced tubes experiencing falling film seem to find a maximum.

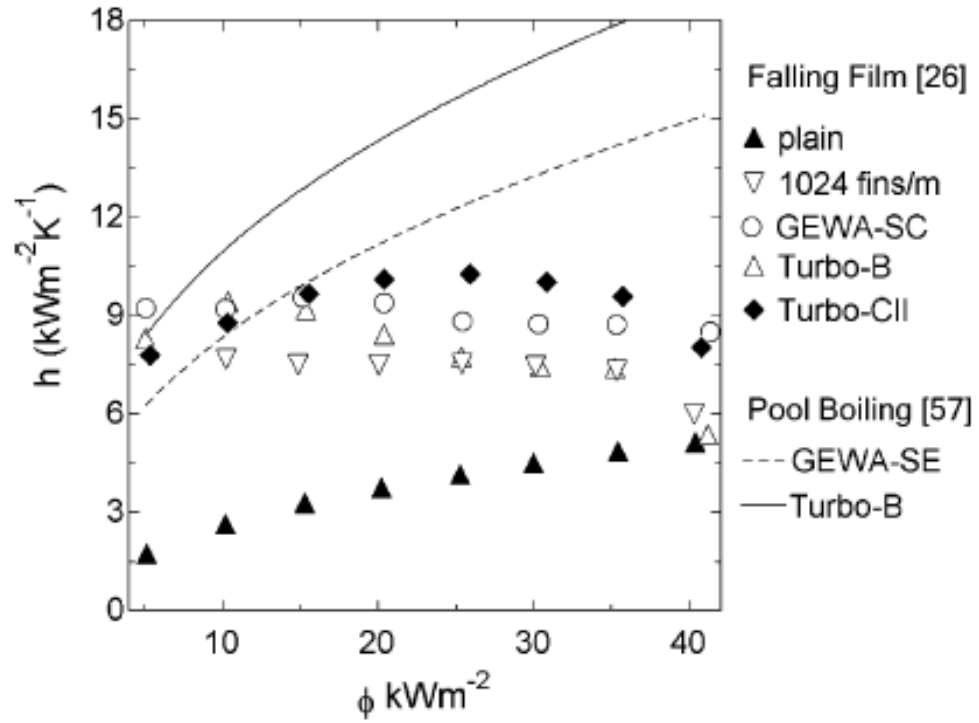


Figure 11: Comparison of single tube performance R134a [46].

The effects of falling film on a bundle of tubes (four rows high) are apparent in Figure 12. Many of the same tubes tested in the single case for falling film perform better in the bundle configuration. Some of this effect may be due to test casing design, as is mentioned shortly. Notice the superior performance of the condensation tubes in the falling film study. In both the single and bundle demonstrations the refrigerant was R134a.

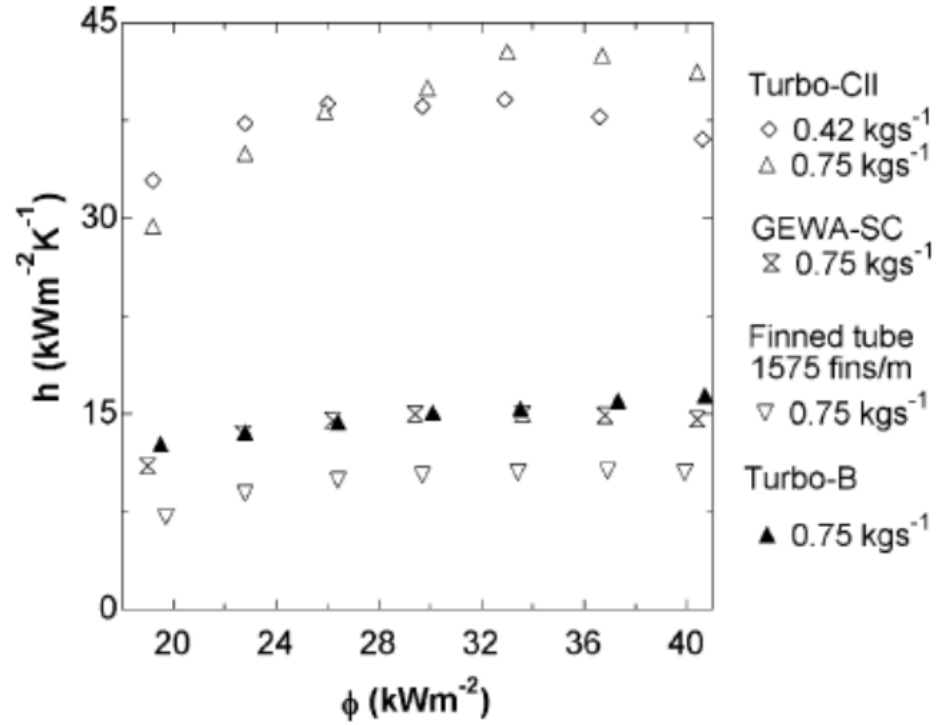


Figure 12: Comparison of tubes in falling film bundle using R134a (from Moeyken, 1994) [46].

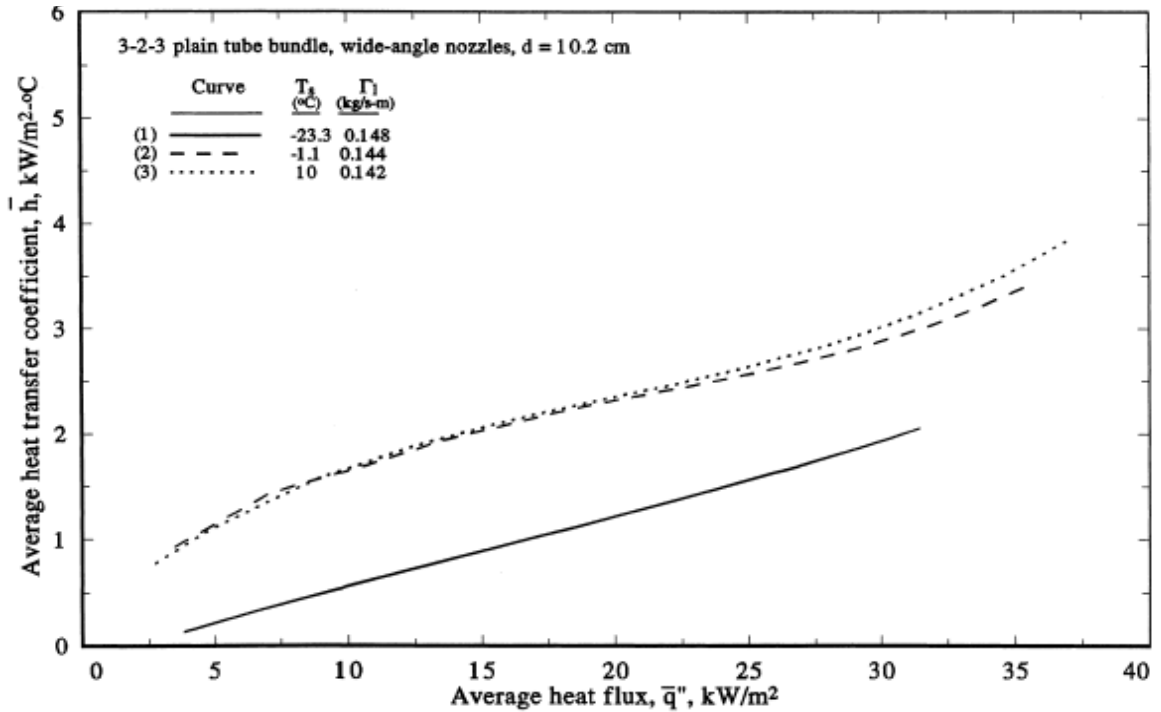


Figure 13: Plain nozzle fed falling film bundle using NH3 [45].

Figure 13 shows the performance of smooth tubes in a falling film bundle using ammonia. The tubes were nozzle fed. The results can be compared with the

result of the smooth single tube tested in Figure 11 using R134a, with the caveat that one is a bundle and the other a single tube. The results seem to indicate similar performance between the two refrigerants. It is hard to tell whether the bundle is improving or degrading performance in this case, as it has been shown to have both effects depending on certain variables [24], so it is difficult to assess whether or not ammonia is advantageous to R134a in this case. Like the “bundle effect”, it has been claimed that ammonia, in LGTE applications, can often be advantageous but sometimes negligibly so [14].

Figure 14 demonstrates the effect of varying the nozzle configuration on a spray fed falling film bundle using R134a and low fin tubes at a constant refrigerant flow rate. Figure 15 provides a description for each nozzle configuration in the caption. The effect of the nozzle configuration seems more pronounced at higher heat fluxes; possibly due to the effect on the ability to more uniformly administer fluid to a surface which is increasingly prone to dry out.

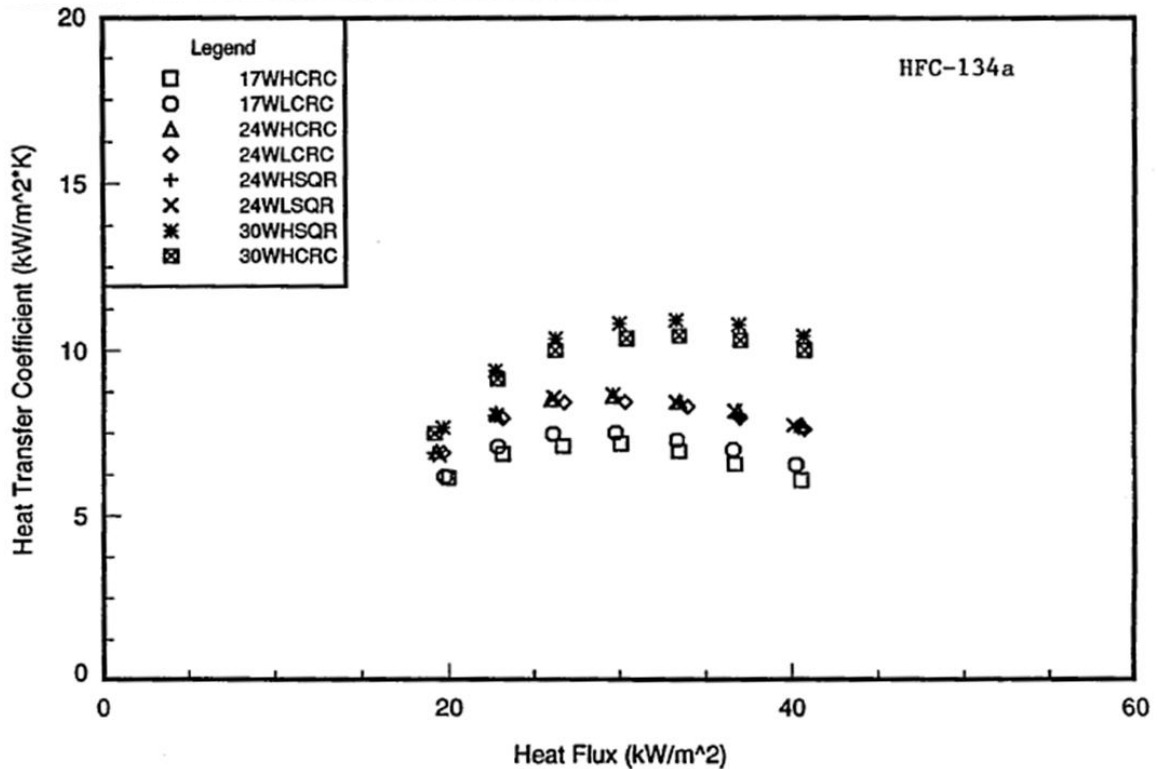


Figure 14: Varying nozzle configuration on falling film low fin bundle 25 [kg/min] R134a [15].

Nozzle Configuration	Orifice Diameter (mm)	Distance Above Bundle (mm)	Spray Pattern	Refrigerant Application
17WHCRC	3.97	66.7	Circular	R-134a
17WLCRC	3.97	41.3	Circular	R-134a
24WHCRC	4.76	66.7	Circular	R-134a
24WLCRC	4.76	41.3	Circular	R-134a
24WHSQR	4.76	66.7	Square	R-134a
24WLSQR	4.76	41.3	Square	R-134a
24WDCRC	4.76	44.3	Circular	R-123
30WHCRC	5.56	66.7	Circular	R-134a, R-22
30WHSQR	5.56	66.7	Square	R-134a
30WDCRC	5.56	44.3	Circular	R-123

Figure 15: Description of nozzle configurations for figure above [15].

Figure 16 shows the difference between a bundle of Turbo-CII tubes - referenced in the previous section on best performers – and the same tube in the single test section. The refrigerant (R134a), tube dimensions and geometry, and falling film mode are the same in all cases. The lower flow rate for the single tube results from lower demand, the surface is fairly well matched to the 416 [g/s] test, as far as over-feeding is concerned. The major difference is in the test casing. The single test case had a more confined vapor flow area and an overall different design when compared with the larger bundle test section.

Finally, Figure 17 demonstrates the effect of varying flow rate on falling film performance. A single array of Turbo-B5 tubes are tested using R134a at 5 °C saturation temperature. It is noteworthy that after film Reynolds numbers exceed the onset of dry-out threshold, further increases in flow rate has a negligible effect on performance.

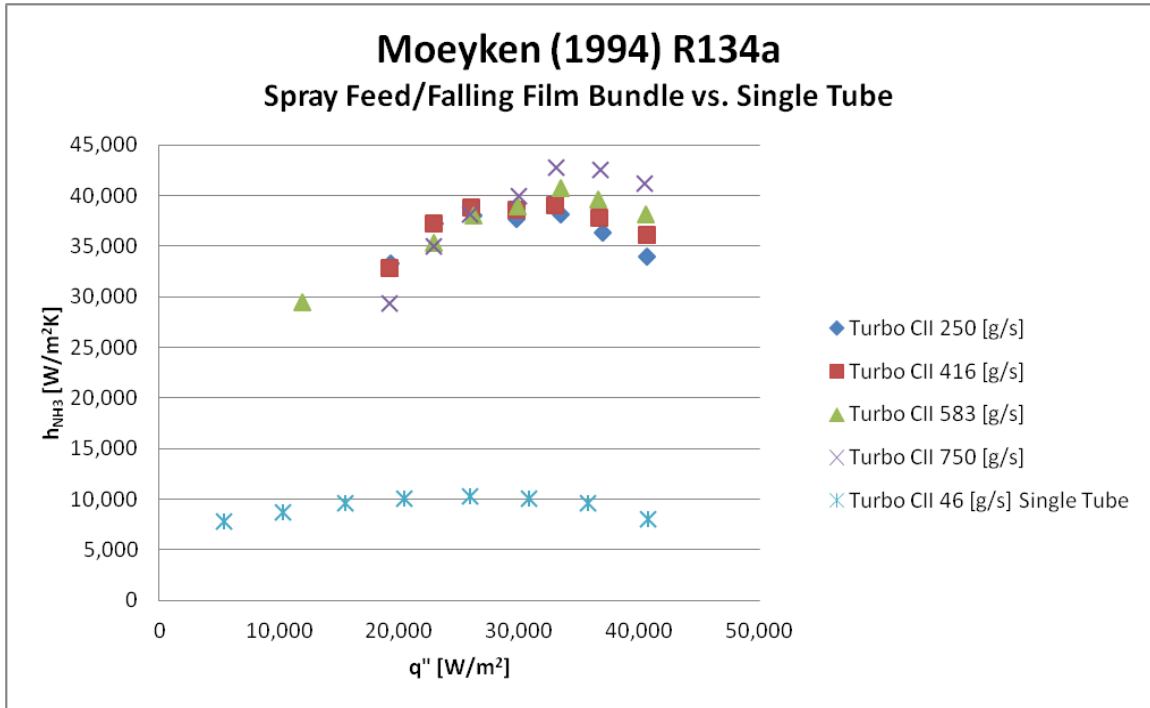


Figure 16: Effect of test rig for bundle vs. single tubes [15].

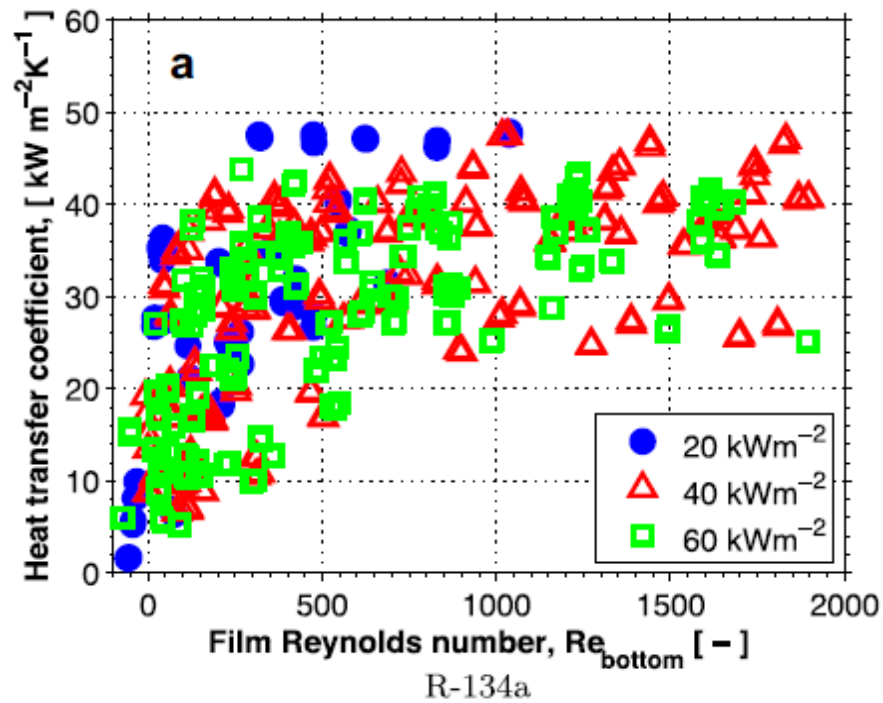


Figure 17: Turbo-B5 falling film single array using R134a, at 5C Tsat, as flow rate varies [25].

In general, these results demonstrate that delivery mode, heat flux, refrigerant, surface geometry, saturation temperature, refrigerant flow rate, nozzle configuration,

and flow rate, among other variables, can significantly alter results. The same exact evaporator tube can provide very high heat transfer in one configuration and very little in another. It is, therefore, very important to ensure that the specific evaporator configuration is assessed carefully for each application before a design is finalized.

Capillary Feed/Rising Film:

A 2011 study conducted by Wang et. al. used a novel horizontal capillary feed concept for a tubular evaporator as part of an absorption chiller design [19]. The concept is identical to the horizontal feed system which was developed in our research, and it seems this author and his team independently developed the same mechanism. In the 2011 study, a single evaporator tube was set above a feed tray which contained the liquid pool of refrigerant. Rectangular microchannels, cut into the exterior of the evaporator, provided the capillary wicking to draw the fluid over the surface of the tube where it was evaporated which was termed “rising film”. The tube dimensions and material are not specified. The evaporator section was tested using water at a saturation temperature of 5 [C]. Results are shown in Figure 18. Figure 19 shows performance as the immersion depth of the tube was varied. The immersion depth, or the level of refrigerant relative to the tube diameter, was normalized so that 1 represented a liquid depth level with the top of the tube.

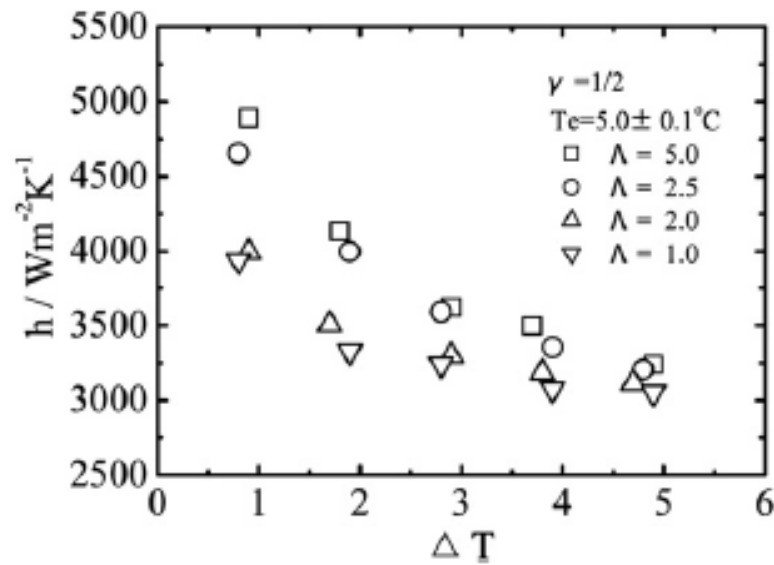


Figure 18: Results from "rising film" capillary feed using water at 5C Tsat [19].

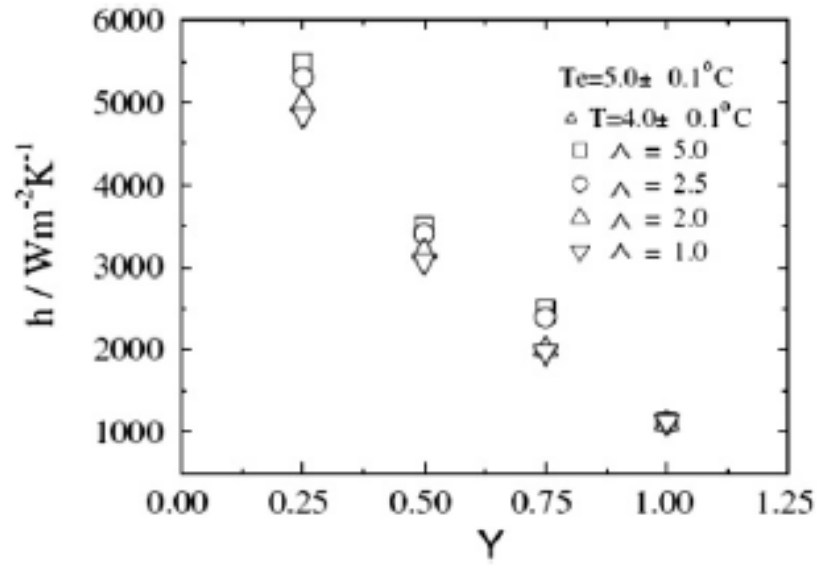


Figure 19: Results from "rising film" capillary feed as immersion depth is varied [19].

Chapter 3: Experimental Methods

Summary of Testing

The following sections discuss methods, results, and analysis for the experimental testing which was conducted during this research. Different evaporator tubes and experimental loops were developed to achieve results which prove the viability of the final capillary feed designs. All tubes were testing in the single tube casing; there were no tube bundles tested in this research. Table 8 provides the reader with a guide of tests conducted which may be helpful in understanding the following sections. Detailed descriptions of each test loop and evaporator surface are found below.

Table 8: Summary of testing.

Experimental Loop	Purpose	Fluid	Single Tube Surfaces Tested
Vertical Capillary Feed Development	Vertical Capillary Feed Mechanism Development	Ethanol	2" One Foot Tube
			¾" Half-Length Plain Fin Tube
Ethanol Test	Preliminary Performance Assessment	Ethanol	2" One Foot Tube
			¾" Half-Length Plain Fin Tube
Ammonia Integrated Test	Initial NH3 Testing	NH3	2" One Foot Tube
Ammonia Independent Test	Final Test Matrix	NH3	2" One Foot Tube
			¾" Half-Length Plain Fin Tube
			¾" Half-Length ISTF Tube

Vertical Capillary Feed Development Loop

Initial testing focused on the vertical tubular evaporator orientation; consequently, a need to provide even capillary feeding in this vertical orientation was one of the earliest issues addressed. The horizontal feed mechanism – a pool feed method also termed “rising film” in literature – was developed later during tests using the independent ammonia test loop and are discussed in a later section. Several preliminary studies were conducted to test the ability to wet an enhanced vertical tubular surface via capillary wicks, liquid guides, and capillary channel tubes. Ethanol was selected as a working fluid for these tests as it shares similar properties with ammonia such as surface tension (Ammonia = .021 [N/m], Ethanol = .018 [N/m]), latent heat of evaporation (Ammonia = 1182 [kJ/kg], Ethanol = 846 [kJ/kg]), and the fact that it can boil at atmospheric pressure below the boiling point of water

(78 [C]). Ethanol enabled us to test the effectiveness of a feed tube in an open tube configuration. The open tube configuration means that there is no shell encasing the evaporator tube; thus, the working fluid evaporates directly to a ventilation system at ambient pressure. This offers the ability to directly observe and manipulate the operation of the feed tube in real time. This open tube configuration proved invaluable as it accelerated test assembly time and provided visual confirmation of the particular success and failures of an individual feed design.

In the vertical capillary feed development loop, hot water is pump through a closed circuit which includes the evaporator surface in question. A separate loop delivers ethanol to a feed tube, secured to the surface of the evaporator tube, and capillary wetting of the microstructure evaporator surface is visually inspected. Rough measurements are recorded for waterside heat transfer and ethanol feed rate. Results of different feed tubes are compared and a favorable feed is selected. This study was conducted to develop vertical feeds for both the 2" one foot tube and the 3/4" half-length tube operating in the vertical orientation. Figure 20 shows the loop schematic, and Figure 21 shows the open tube configuration mounted in the test loop.

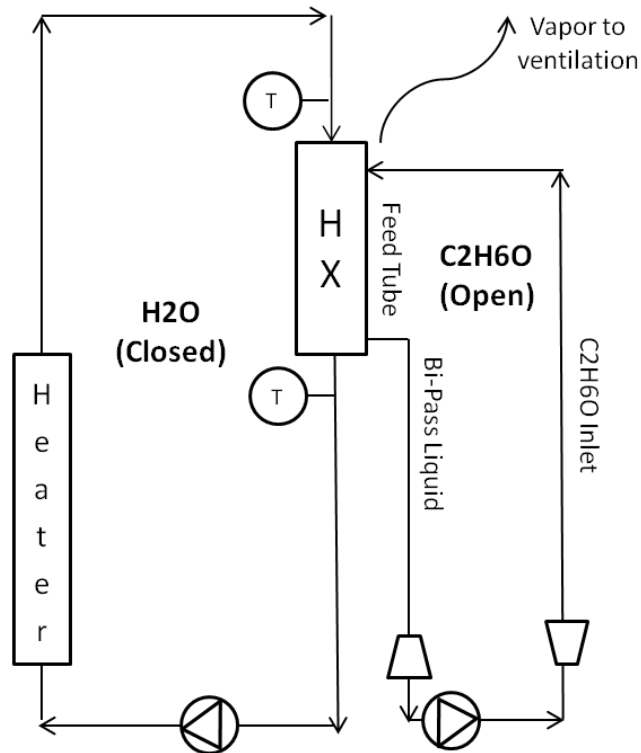


Figure 20: Vertical capillary feed development loop schematic

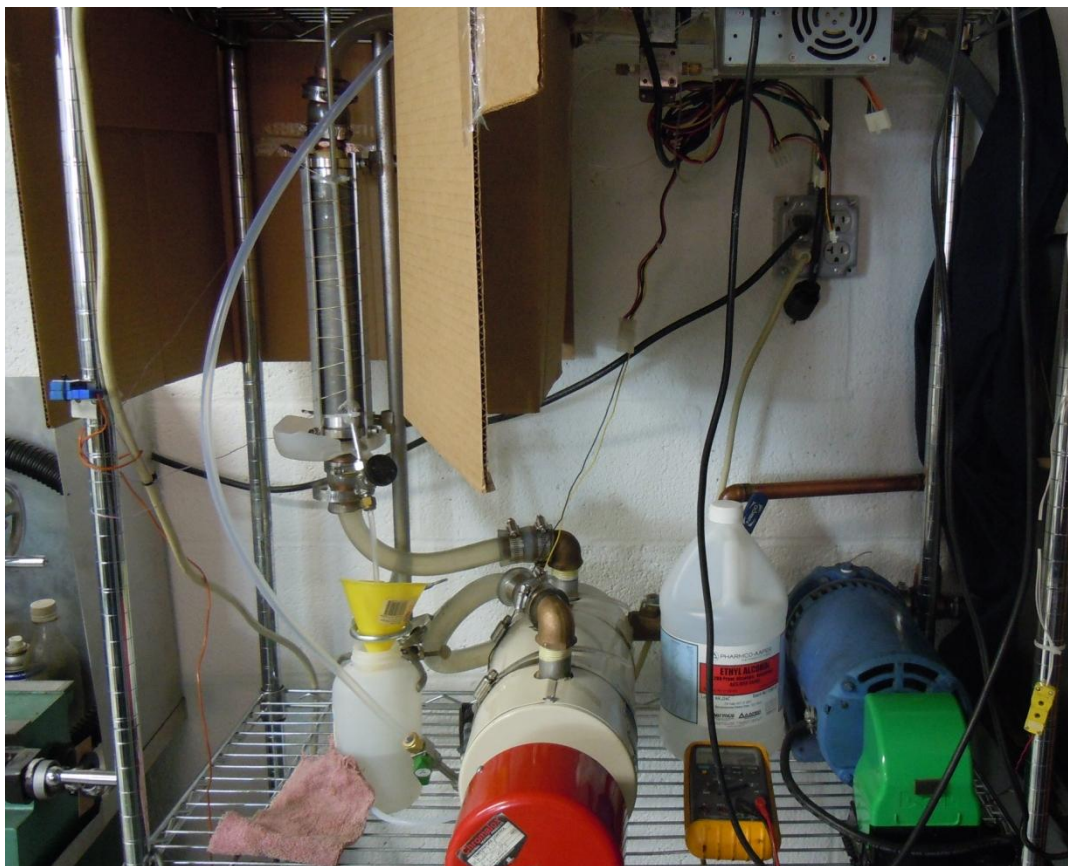


Figure 21: Vertical capillary feed development loop. Note open tube configuration.

During vertical feed tube development several feed concepts were tested. These feed concepts include capillary wicks, liquid guides, and capillary channel tubes. Capillary wicks are thick strings composed of ceramic fibers which become saturated with liquid and are pressed against the micro structure of the evaporator. Several wick concepts were tested, including solid core and hollow core wicks, and liquid travelled through the wick by way of capillary action with gravitational assistance. Liquid guides are simply solid rods which were pressed against the evaporator surface. Liquid was fed near the top of the guide, and fell downward long the evaporator surface. Surface tension ensured that the liquid ran along the region where the evaporator surface contacted the guide, which kept the liquid from spreading out over the surface and creating areas of flooding. Finally, capillary channel tubes were tested. Capillary channel tubes deliver liquid to a channel cut into the edge of a liquid guide. The channel is filled with liquid and held tight to the evaporator surface. Liquid flows downward through the channel assisted by gravity. Optionally, sub-cooled liquid can be introduced multiple times into the channel at various points along the flow length. This helps to ensure that boiling does not occur in the channel which tends to obstruct the liquid flow path. Ultimately, the capillary channel feed was selected as the favorable vertical delivery mechanism both for the 2" one foot tube and the half-length $\frac{3}{4}$ " tube. Figure 22 shows the three families of concepts tested, the liquid guide, wick, and channel feeds. Figure 23 shows examples

of some of the various feed tube designs tested during the development process, and Figure 24 shows the half-length $\frac{3}{4}$ " tube channel feed installed in the open test configuration.

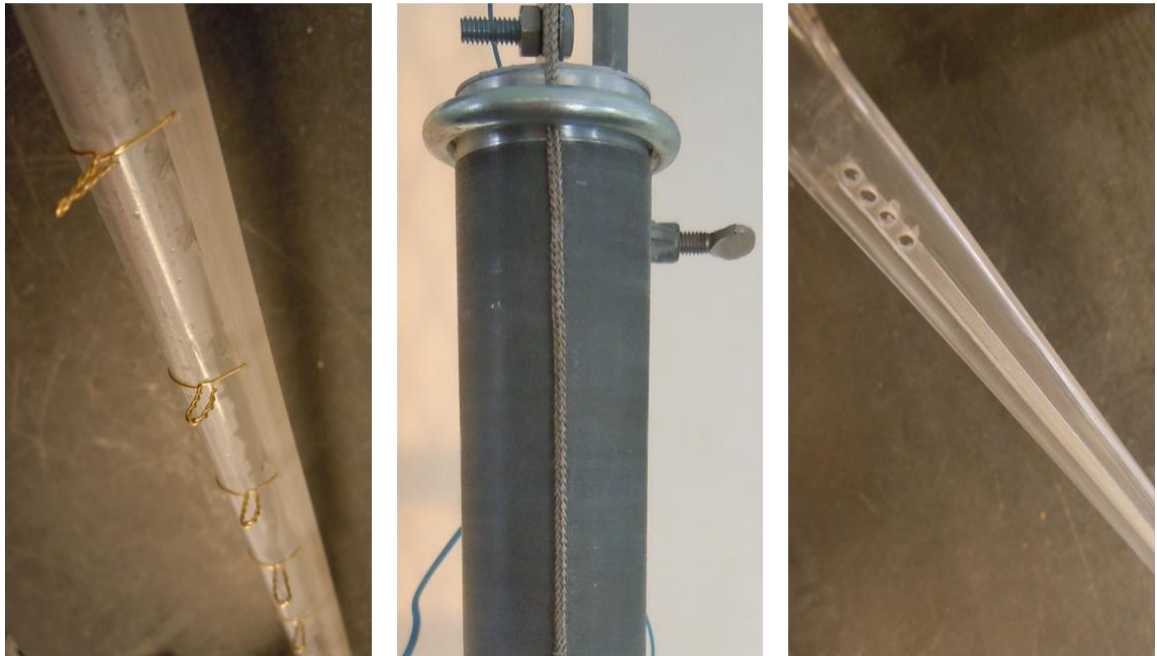


Figure 22: Types of feed mechanisms: Liquid guide (left), wick (center), channel (right).

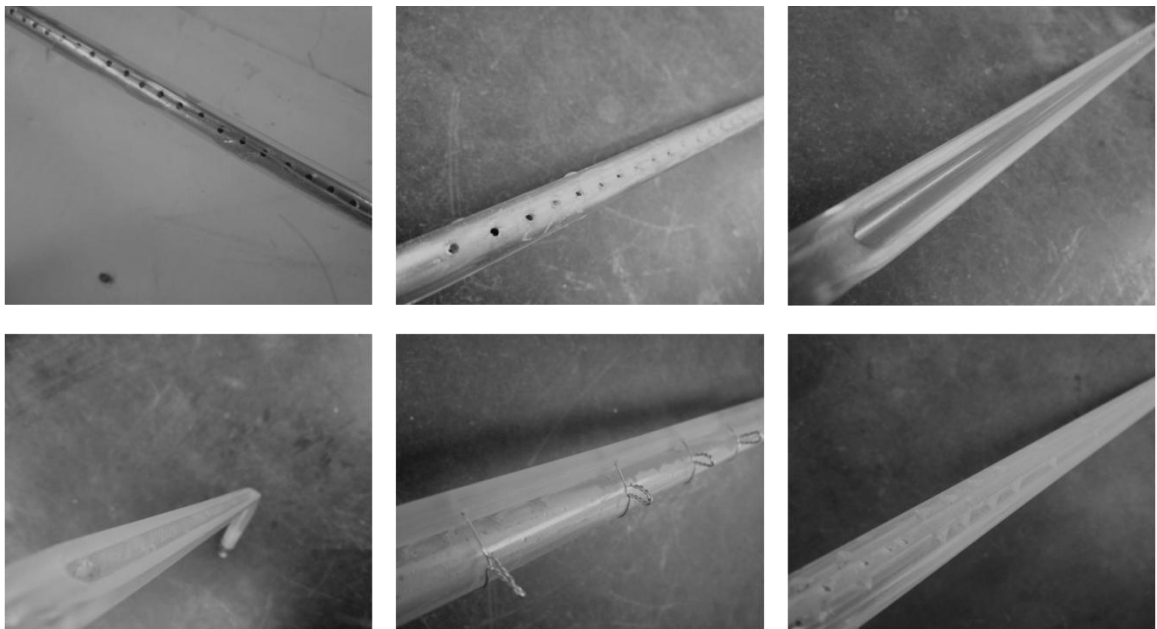


Figure 23: Examples of various feed concepts tested.

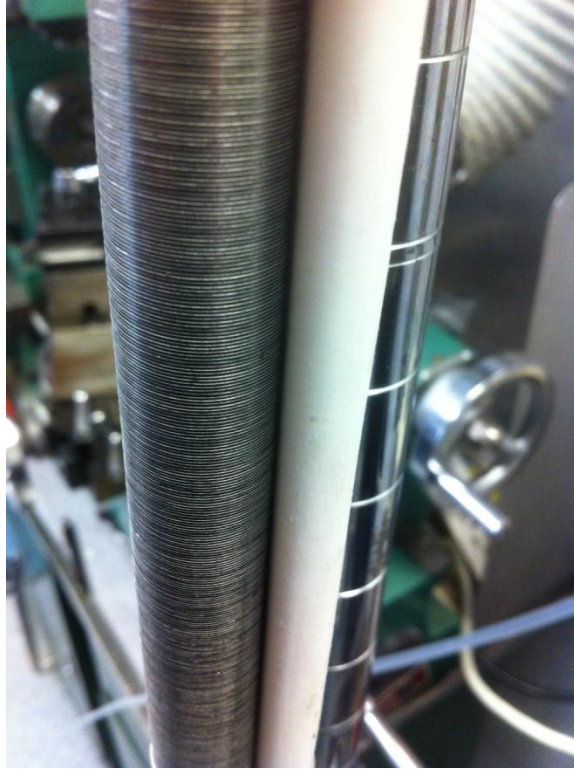


Figure 24: Half-length 3/4" evaporator and channel feed tube in open test configuration.

Feed tube performance was evaluated in the capillary development loop by both visually inspecting for proper wetting and estimating the overall heat transfer coefficient of the evaporator-feed combination. Secondary variables estimated – Q and refrigerant side flow rate - were important guides for operating conditions should the feed design be selected for deployment in further tests. The overall heat transfer coefficient was identified by calculating Q for parametrically increasing heat input to the water loop until the evaporator-feed combination began to experience dry out. In most cases, the evaporator tube was held constant so that the various feed tubes could be compared directly. In the open loop, it was impossible to force LMTD on the evaporator surface so LMTD varied between cases; however, feed-evaporator combinations with higher U tended to favor lower LMTD conditions in which there was no boiling. This is likely due to the presence of thin film conditions. It is important that the tube should not experience catastrophic failure if boiling does occur, so allowing for higher LMTDs in the feed development stage was permitted and desirable. Ultimately, closed NH_3 tests which assessed performance below the onset of nucleate boiling were not possible due to uncertainty limitations. As a result it was fortuitous that during open ethanol tests, the feed tube was developed to continue function during boiling. Future testing which can assess performance of capillary fed evaporators operating in sub-boiling conditions is likely to produce valuable results. After open ethanol testing concluded, performance results were compared, and a feed selection was made both for the 2" one foot tube and the 3/4" half-length tube.

The primary performance variable calculated was overall heat transfer coefficient of the evaporator-feed combination. Heat input to the water loop was varied by measuring power input to a 3000 [W] maximum capacity electric water heater using a variable transformer and multi-meter. Incidental heat input to the loop from the water pump was measured experimentally and factored into the total heat input. The system was allowed to reach steady state. Losses to ambient were ignored. Assuming energy balance, the heat transferred by the evaporator was estimated from the following equation at steady state.

$$Q_{sys} = Q_{H2O} = Q_{Heater} + Q_{Pump}$$

LMTD was estimated by assuming the saturation temperature of ethanol at atmospheric pressure and considering latent heat transfer only using the following equation.

$$LMTD = \frac{(T_w - T_{sat}) - (T_{w,out} - T_{sat})}{\ln\left(\frac{T_w - T_{sat}}{T_{w,out} - T_{sat}}\right)}$$

Finally, overall heat transfer coefficient was calculated as follows.

$$U = \frac{Q_{sys}}{A_s LMTD}$$

The ethanol flow rate was estimated by measuring the difference between inlet ethanol flow rate and ethanol which bi-passed the heat exchanger and was not evaporated. In most cases, there was a significant amount of bi-pass liquid as it was found to be beneficial to over supply the feed tube in order to suppress boiling in the feed tube which obstructs liquid flow to the surface. Table 9 shows instrumentation used in the capillary development loop. It is important to note, due to the open test configuration, performance was estimated for the purposes of tube comparison only, and precise performance measurements with energy balance cross checks would be superfluous or impossible.

Table 9: Capillary development loop instrumentation.

Measurement	Device
Q_{Heater}	Multi-meter
$T_w, T_{w,out}$	T-Type Thermocouples
\dot{m}_{C2H6O}	Beaker/Stop Watch

Ethanol Test Loop

The ethanol test loop adopted the vertical capillary feed development loop, but added a closed ethanol loop and other instrumentation so that vertical closed tube performance could be verified, with reasonable accuracy, prior to ammonia testing.

Ethanol testing could be conducted on our small in house loop with easy modifications and little concern for minor leaks or material compatibility. Ammonia testing could only take place in the large shared ammonia test facility, which required scheduling test time, and considerable resources were required to install and charge leak tight test components. Therefore, it was desirable to ensure that the test section would perform properly prior to ammonia testing; the ethanol loop was used for this purpose. Figure 25 shows the ethanol test loop schematic in the 2" one foot tube configuration, and Figure 26 shows a photograph of the test loop with the $\frac{3}{4}$ " half-length tube configuration. The same test loop was used for both the $\frac{3}{4}$ " half-length tube and the 2" one foot tube; however, the $\frac{3}{4}$ " tube did not require an external ethanol outlet separator whereas the 2" tube did. The $\frac{3}{4}$ " half-length tube evaporator with large casing in the vertical orientation could double as an integrated outlet separator because the test casing had two outlets: a vapor outlet at the top and a liquid outlet at the bottom. Figure 27 shows the vapor and liquid outlets, and liquid inlet, on the $\frac{3}{4}$ " half-length evaporator test casing.

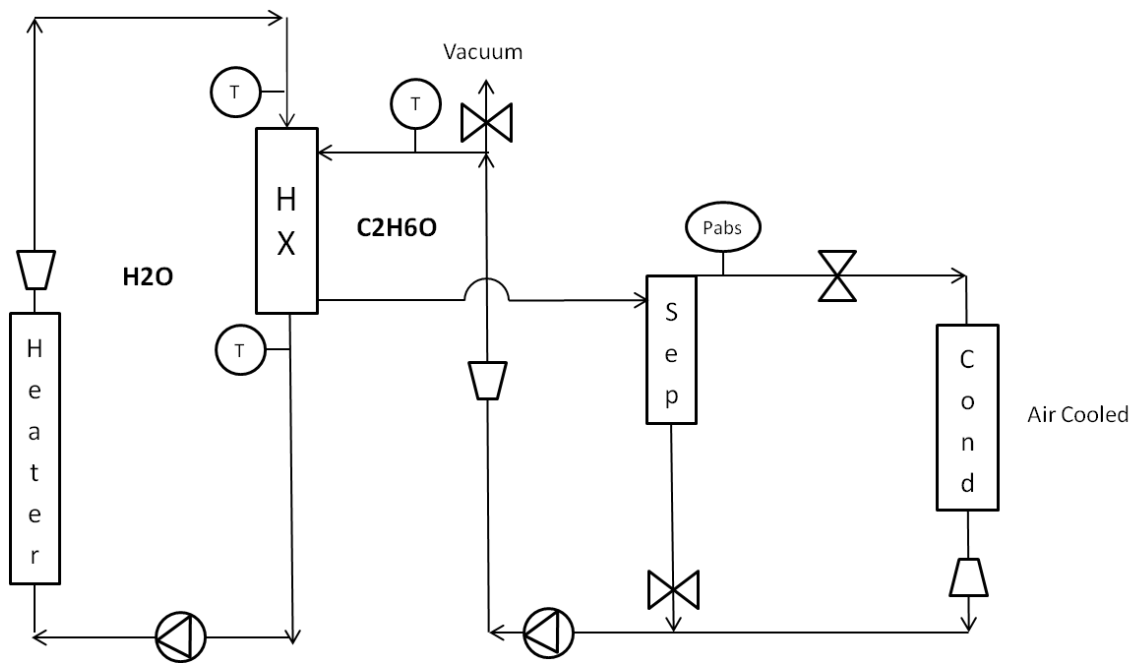


Figure 25: Ethanol test loop schematic (2" one foot test configuration shown).



Figure 26: Ethanol test loop (3/4" half-length test configuration shown).



Figure 27: Ethanol test loop 3/4" half-length liquid inlet/vapor outlet (left) and liquid outlet (right)

Tube performance was evaluated by establishing steady state operation between both the closed water and ethanol loops, and measurements were taken in order to estimate total heat transfer and overall heat transfer coefficient. Heat input to the water loop was varied by measuring power input to the 3000 [W] maximum capacity electric water heater using a variable transformer and multi-meter; however, with the introduction of a water side flow meter it was possible to calculate Q_{H2O} directly from the energy conservation equation. Calculating Q_{H2O} proved a more accurate method of assessing heat transfer, so the heater setting was used merely as a guide for test settings. Losses to ambient were ignored. General heat transfer and energy balance were estimated from the following equations.

$$Q_{H2O} = (\dot{m}C_p\Delta T)_{H2O}$$

$$Q_{C2H6O} = (\dot{m}h_{fg})_{C2H6O}$$

$$EB = abs\left(\frac{Q_{H2O} - Q_{C2H6O}}{Q_{H2O}}\right) * 100$$

Inlet and outlet ethanol enthalpy was estimated from measured P_{sat} and the assumption that $X_{inlet} = 0$ and separator outlet quality is known ($X_{vapor}=1$ and $X_{liquid} = 0$). The inlet mass flow rate of the ethanol for the 2" one foot tube configuration was measured; however, there was no measurement for the bi-pass liquid or condenser portion of the loop. As a result, heat transfer for the 2" one foot tube was estimated using water side calculations only, and energy balance was not calculated. The 3/4" half-length configuration featured a condenser outlet flow measurement; thus, energy balance was calculated using the mass flow rate in the conservation of mass statement below.

$$\dot{m}_{C2H6O \text{ evaporated}} = \dot{m}_{C2H6O \text{ condenser outlet}}$$

Most tubing in the loop is clear PTFE, so it was possible to visually confirm that the separator outlet quality assumptions are reasonable ($X_{\text{vapor}}=1$ and $X_{\text{liquid}} = 0$). Overall heat transfer coefficient was calculated according to the equation defined in the capillary development loop methods section. Secondary variables, such as inlet ethanol flow rate, were directly measured in the ethanol test loop. Table 10 shows instrumentation used in the ethanol loop.

Table 10: Ethanol loop instrumentation

Measurement	Device	Make/Model
Data acquisition	Data logger switch unit and laptop	Agilent/34970A
$\dot{m}_{\text{H}_2\text{O}}$	Float-type Rotameter	Maximum: .52 [l/s]
$\dot{m}_{\text{C}_2\text{H}_6\text{Oinlet}}$ (2" Tube)	Float-type Rotameter	Maximum: 2.57 [ml/s]
$\dot{m}_{\text{C}_2\text{H}_6\text{Oinlet}}$ (3/4" Tube)	Coriolis Mass Flow Meter	Endress-Hauser/Promass 63A
$\dot{m}_{\text{C}_2\text{H}_6\text{Ocondenser}}$ (3/4" Tube)	Coriolis Mass Flow Meter	Endress-Hauser/Promass 83A
$T_w, T_{w,\text{out}}$	1/10 DIN RTD Thermistors	Omega/(P-M-1/10-1/4-6-0-P-3)
T (general)	Thermocouples	T-Type
P_{sat}	25 PSIA Transducer	Setra/205

Ammonia Integrated Test Loop

Initial ammonia tests were conducted with the vertical 2" one foot tube using an integrated ammonia test loop. In this loop the test section replaced a different existing larger scale heat exchanger. Testing was conducted for a short time; however, the results were problematic. Severe oscillations in ammonia flow rate due to an oversized ammonia pump and PID control, and test section flooding were apparent. These phenomena are discussed in detail in the results section. As a result, the ammonia integrated test loop was abandoned after a short time; and, further ethanol tests using the new external outlet separator, as discussed in the previous section, commenced. Figure 28 shows the ammonia integrated test loop schematic, Figure 29 and shows the 2" one foot tube test section ready for deployment in the integrated loop. Note that the test section lacks a separator, and two phase flow at the outlet is forced upward, via a 90° elbow, against the hydrostatic pressure gradient into the much larger ammonia circulation without pump assist. This configuration resulted in test casing flooding. It may be useful to note the short falls of this configuration for future LGTE design discussions; however, as the loop was not a success no further discussion of the methodology is warranted.

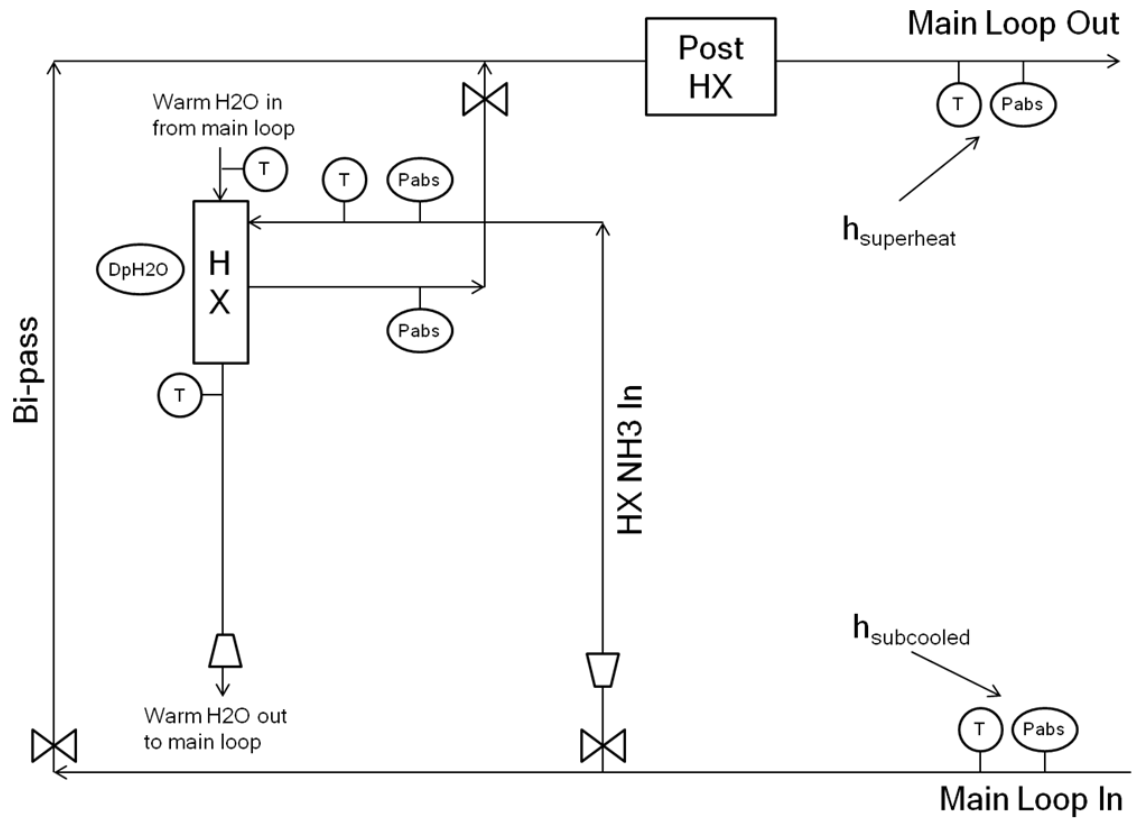


Figure 28: Ammonia integrated test loop schematic



Figure 29: 2" one foot tube in the ammonia integrated test loop configuration, elbow at outlet.

Ammonia Independent Test Loop

The most beneficial and complete set of test results were conducted with the ammonia independent test loop. This test loop was developed on very short notice after issues with scheduling time to share the larger ammonia test loop proved it

necessary to be able to operate independently. The loop was designed and fabricated in approximately three weeks' time, and was used for almost a month to collect data on five different test configurations (three separate surfaces). The independent test loop was adopted from the ethanol loop design, and modified to allow operation in the ammonia environment. Testing was possible for vertical and horizontal orientations with this loop. The horizontal feed mechanism was developed during testing for this loop, and is described in a following section about the small test casing. All materials were made ammonia compatible and pressure vessels and seal surfaces were designed to provide acceptable containment. The replacement of all PTFE tubing in the loop with SS316 was necessary for containment, but the ability to visualize flow conditions was lost. Resultantly, two custom fabricated flow visualization windows were constructed at critical points to ensure that the separator outlet quality assumptions, discussed in the previous section, remained valid ($X_{\text{vapor}}=1$ and $X_{\text{liquid}}=0$). This flow visualization window is shown in Figure 32. A schematic of the independent loop is shown in Figure 30 and an image of the loop can be seen in Figure 31.

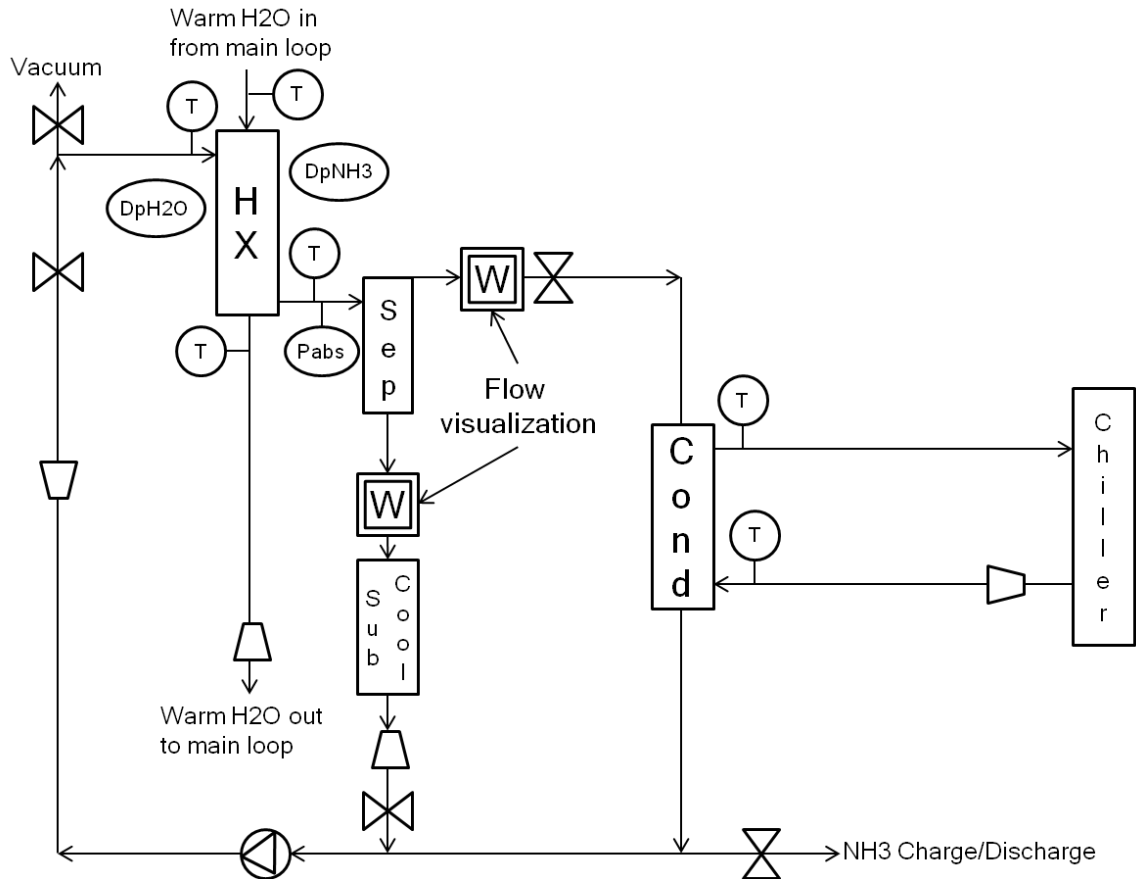


Figure 30: Independent ammonia test loop schematic.

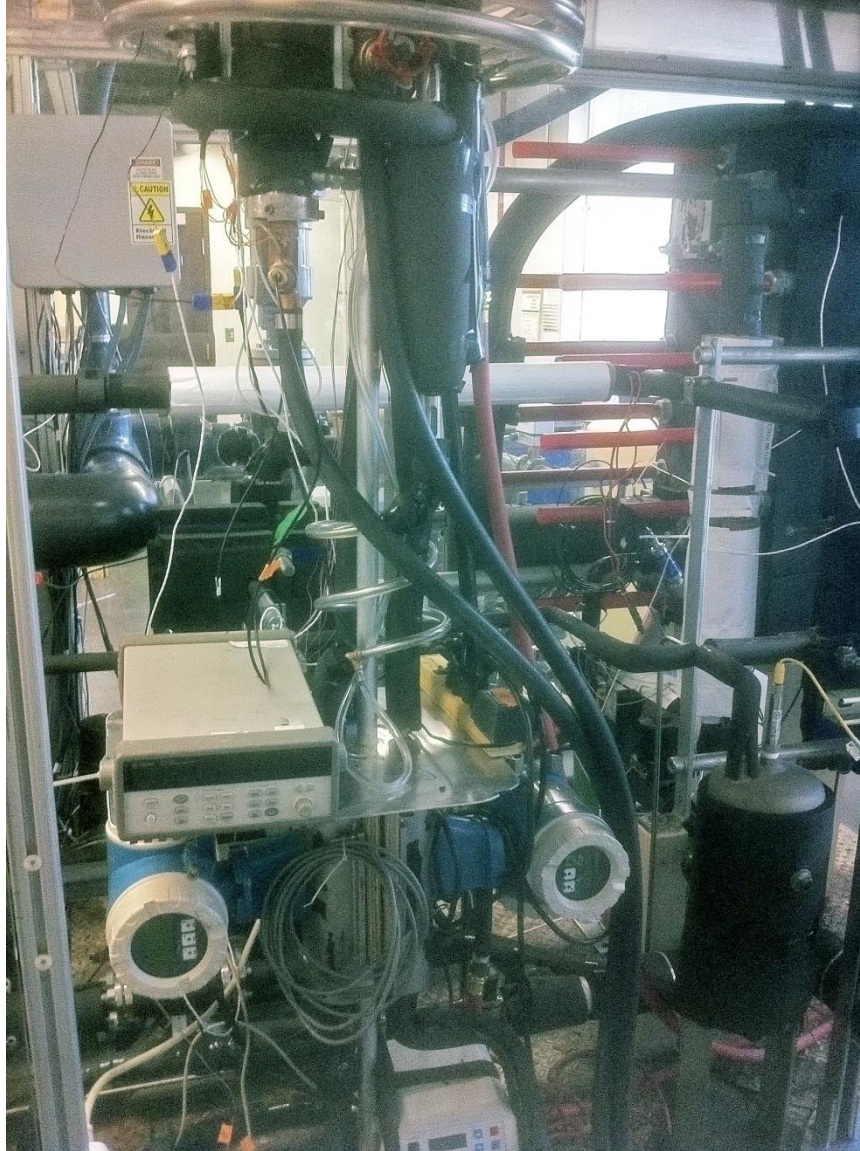


Figure 31: Independent ammonia test loop photograph.



Figure 32: Flow visualization window.

Tube performance was evaluated by establishing steady state operation between the warm water, ammonia, and condenser loops. Measurements were taken in order to estimate total heat transfer and overall heat transfer coefficient. Heat input to the loop was varied by controlling the existing warm water loop which consisted of a sea water tank, heater, mass flow meter, and pumping system. Ammonia loop conditions were adjusted by controlling the independent loop pump system, and initially, by setting the loop ammonia charge level such that it was possible to visually verify the separator outlet quality assumptions are correct using the visualization windows ($X_{\text{vapor}}=1$ and $X_{\text{liquid}}=0$). The condenser water temperature and flow rate was adjusted, in combination with the vapor outlet valve (via P_{sat}), to control LMTD at the evaporator. LMTD was calculated using the absolute pressure transducer. Losses to ambient were ignored and negligible as the loop was well insulated and ambient temperature was usually within 5 [K] of the loop. After steady state conditions were established at the desired test point, data was recorded for several minutes, and averaged values were used to calculate performance variables according to the following equations.

$$Q_{evaporator} = (\dot{m}C_p\Delta T)_{evaporator\ H2O}$$

$$Q_{NH3} = (\dot{m}h_{fg})_{NH3}$$

$$Q_{condenser} = (\dot{m}C_p\Delta T)_{condenser\ H2O}$$

$$EB = abs\left(\frac{Q_{evaporator} - Q_{condenser}}{Q_{evaporator}}\right) * 100$$

Inlet and outlet ammonia enthalpy was referenced from measured P_{sat} and the assumption that $X_{inlet} = 0$ and separator outlet quality is known ($X_{vapor}=1$ and $X_{liquid} = 0$). All test configurations required the use of the external separator, except for the 3/4" half-length vertical test configuration which made use of the separation effect inherent in the casing design, as discussed in the ethanol loop methods section. The evaporated ammonia mass flow rate was estimated from the following relation.

$$\dot{m}_{NH3\ evaporated} = \dot{m}_{NH3\ inlet} - \dot{m}_{NH3\ bypass\ liquid}$$

Overall heat transfer coefficient was calculated according to the following equation, and LMTD as defined in the capillary development loop methods section.

$$U = \frac{Q_{sys}}{A_s LMTD}$$

Secondary variables, such as inlet ammonia flow rate, were directly measured. Table 11 shows instrumentation used in the ethanol loop.

Table 11: Independent loop instrumentation.

Measurement	Device	Make/Model
Data acquisition	Data logger switch unit	Agilent/34970A
$\dot{m}_{warmH2O}$	Coriolis Mass Flow Meter	Micro Motion/CMF100
$\dot{m}_{coldH2O}$	Float-type Rotameter	Maximum: .091 [l/s]
$\dot{m}_{NH3inlet}$	Coriolis Mass Flow Meter	Endress-Hauser/Promass 63A
$\dot{m}_{NH3bypass}$	Coriolis Mass Flow Meter	Endress-Hauser/Promass 83A
$T_{H2Owarm\ in/out}$	1/10 DIN RTD Thermistors	Omega/(P-M-1/10-1/4-6-0-P-3)
T (general)	Thermocouples	T-Type
P_{sat}	250 PSIA Transducer	Wika/S10
Dp_{NH3}	0 – 1.25 PSID Transducer	Validyne/P55D-30
Dp_{H2O}	0 - 3.2 PSID Transducer	Validyne/DP15-34

2" One Foot Proof of Concept Tube Test Section

The 2" one foot tube was tested as a proof of concept model for the vertical capillary fed enhanced tubular heat exchanger concept. It is not desirable to utilize the tested configuration for the OTEC plant because the tube diameter is too large for favorable bundle packing density. Furthermore, the tube is too short to achieve a measurable waterside temperature difference; thus, it was necessary to install an insert to reduce the internal hydraulic diameter of the tube. This waterside insert introduced a high pressure drop to the loop; however, simultaneously exhibited higher water side heat transfer coefficient for a given flow rate. Figure 33 shows the 2" one foot aluminum evaporator tube and its internal and external surface features. Figure 34 shows the 2" tube test casing which is made of SS316. Figure 35 shows a schematic of the 2" tube operation. Liquid ammonia enters the test section at the top, and travels down the capillary feed tube along the evaporator surface. The evaporator generates vapor which drives bypass liquid, collected at the bottom of the casing, out of the exit port as it leaves. The vapor and bypass fluid mixture enter the separator where visualization windows help ensure proper charge and valid separator outlet quality assumptions. Table 12 gives important information about tube geometry.



Figure 33: 2" one foot aluminum tube.



Figure 34: 2" one foot test section casing.

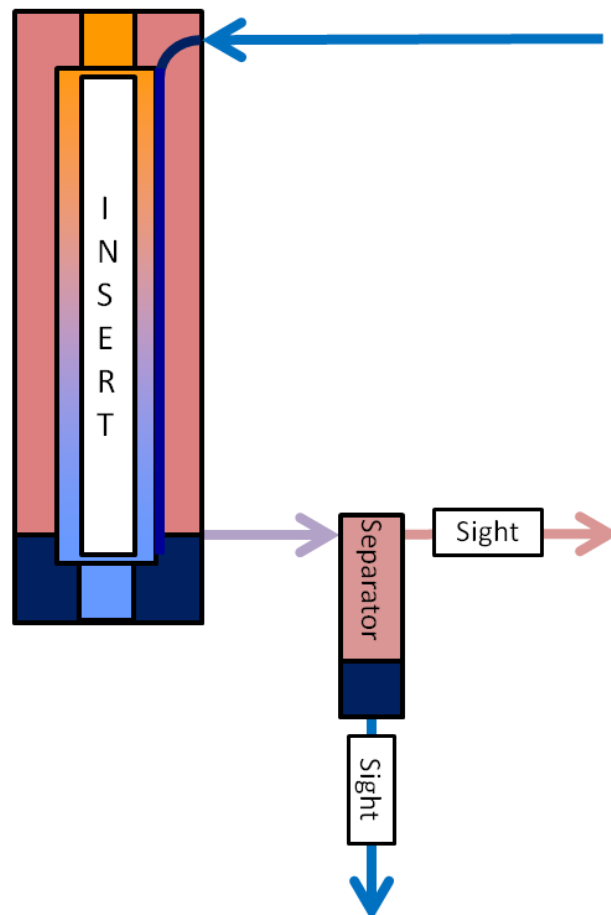


Figure 35: 2" one foot test section schematic showing capillary feed tube and outlet separator.

Table 12: 2" one foot tube and test section critical dimensions.

Tube OD	.0499 [m]
Tube ID	.04786 [m]
Total Heat Transfer A_s	.03225 [m ²]
Heat Transfer Length	.21 [m]
Internal Rifling Cross Section	Triangular
External Microchannel Cross Section	Rectangular
External Microchannel Fin Count	212 [fins/in]
Test Section Casing ID	.0594 [m]
Water Side Insert OD	.0419 [m]

3/4" Half-length Surfaces Tested

The 3/4" half-length tube was the primary focus in ammonia testing for the OTEC application. Two surface geometries were selected for the 3/4" half-length tube: the plain fin and integral saw tooth fin (ISTF). Both surfaces were manufactured from 5052 aluminum. Details for the surfaces tested are shown in Table 13 and an image of the ISTF structure is shown in Figure 36 and Figure 37. The two tubes are shown side by side in Figure 38.

Table 13: 3/4" Half-length Tube Critical Dimensions.

OD	.01818 [m]
ID	.01614 [m]
Total Heat Transfer A_s	.08216 [m ²]
Heat Transfer Length	1.524 [m]
Internal Rifling Cross Section	See Figure 37
External Plain Fin Cross Section	Rectangular
External ISTF Surfacing	See Figure 36

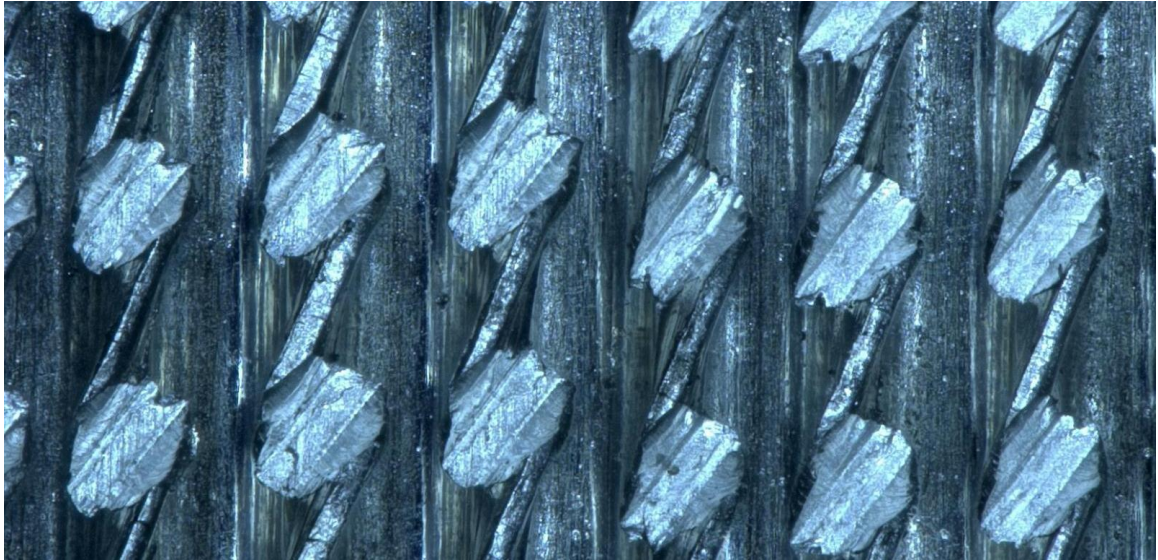


Figure 36: ISTF surface radial view looking inward.



Figure 37: 3/4" ISTF profile with internal rifling visible

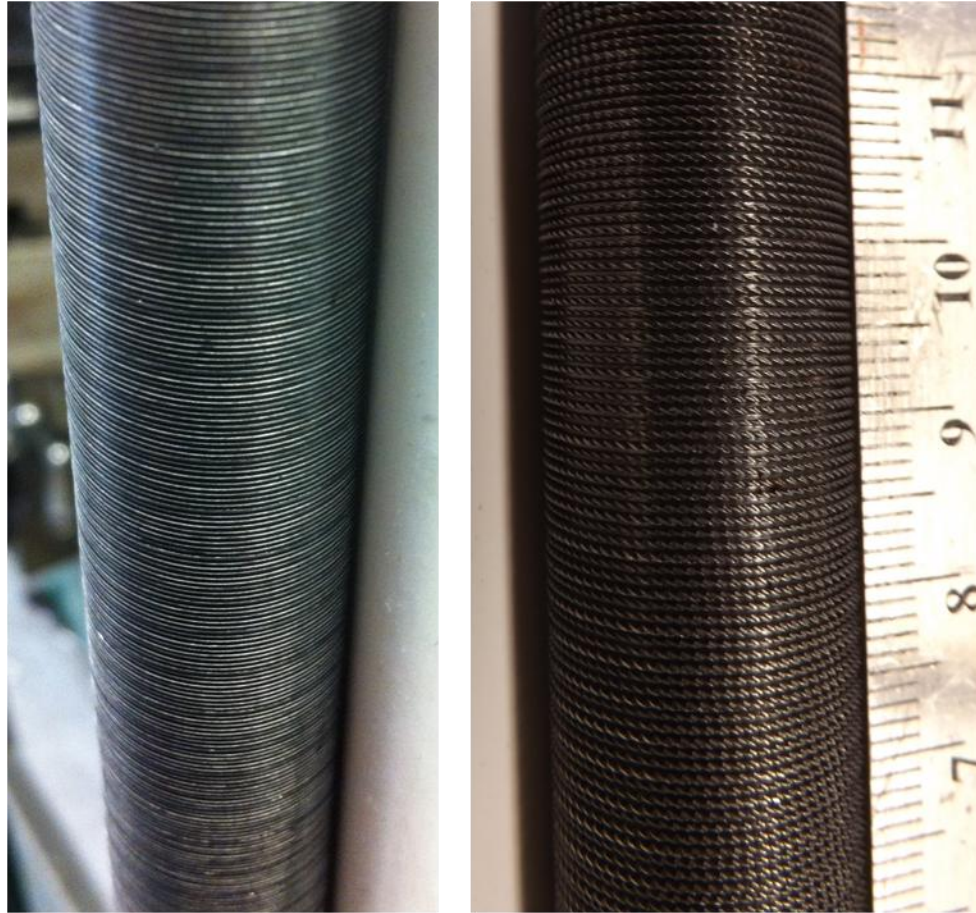


Figure 38: 3/4" half-length tube external surfacing, plain fin (left) and ISTF (right).

Half-length Large Casing Test Section (Vertical Feed)

The $\frac{3}{4}$ " half-length large casing test section was designed to accommodate a capillary channel feed tube so that the half-length evaporator could be tested in the vertical orientation. The large casing was also used in horizontal testing, without the feed, as discussed in the results section, as a way of studying the effect of casing size on horizontal test performance when compared with the small casing test results. In the horizontal orientation, the vapor outlet port was sealed, and the external outlet separator was utilized; however, in the vertical orientation the large casing did not require an external separator as bi-pass liquid exited the bottom outlet port and vapor the top. In horizontal testing, the outlet orientation could be varied (axial rotation) as is described in the following section on the horizontal test casing. Figure 39 shows a solid model of the top manifold of the test casing.

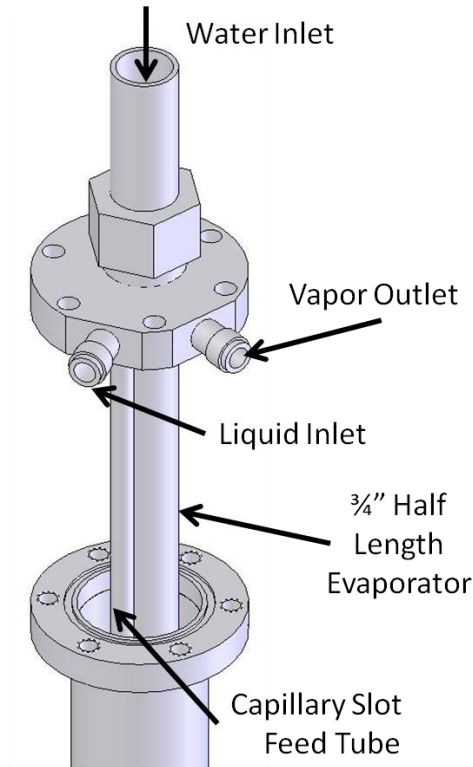


Figure 39: Model of the half-length large casing test section inlet.

Notice the separate liquid inlet and vapor outlet ports. Also, the $\frac{3}{4}$ " evaporator tube is offset from the casing internal diameter center axis. This is to allow space for the capillary channel feed, and is an important consideration for the horizontal test orientation where there is no feed tube installed (asymmetric vapor flow/liquid pool area). Figure 94 shows dimensions for the upper manifold and Figure 95 shows dimensions for the bottom manifold and bi-pass liquid outlet port, both figures can be found in the appendix. Figure 27 shows an image of the inlet and outlet port connections for the large test casing installed on the ethanol test loop. Table 14 summarizes critical dimensions of the large test casing.

Table 14: Half-length large casing critical dimensions.

Casing ID	.0348 [m]
Casing OD	.0381 [m]
Casing Internal Length	1.524 [m]
Material	SS316

Half-length Small Casing Test Section (Horizontal Feed)

The $\frac{3}{4}$ " half-length small casing test section was designed for horizontal test orientation only. It is thought that it is not possible to deploy the capillary feed tube which was developed for the vertical tube orientation in the horizontal. The reason for this thinking is that without the aid of gravity assist, the fluid in the channel would not be sufficiently distributed along the tube length and would be very sensitive to slight changes in orientation other than exactly level with the ground. This hypothesis was never fully tested, due to time constraints; however, so the development of the new feed mechanism was executed as a precautionary measure.

The horizontal feed mechanism is basically a partial immersion of the evaporator tube in a shallow liquid refrigerant pool. Originally termed "pool feed" it was later discovered that another instance of this same feed concept already exists in literature and is termed "rising film" [19]. Figure 40 illustrates how the horizontal feed mechanism works. The evaporator tube is placed inside the small test casing. Unlike the large test casing, the small test casing does not have an offset bore for the evaporator tube – designed to accommodate the feed tube in the vertical tests – and as a result the small test casing provides a smaller but symmetric spacing between the evaporator tube and the casing wall. Liquid ammonia is introduced to the test casing and allowed to run along the gap below the evaporator. As the refrigerant pool comes into contact with the evaporator tube, liquid is drawn up around the circumference of the evaporator due to capillary action within the enhancement surface features. The outlet of the small casing accommodates both vapor and excess (bypass) liquid. By varying the axial orientation of the small test casing, the outlet port position is adjusted and the level of the liquid pool can be varied parametrically. If the outlet port is at the top of the tube, all of the excess liquid, which is driven out of the test casing by high velocity vapor, has to pass over the surface of the evaporator. If the outlet port is at the bottom of the small test casing, excess liquid can easily drain away from the tube, and the evaporator surface is only wetted by capillary action. As the small test casing has a single outlet port, the use of the external outlet separator was required in all tests. The results of pool level tests are communicated in the results section for the horizontal plain tube. Figure 96 shows the cross section view of the inlet end of the small test casing, and can be found in the appendix. Table 15 shows critical dimensions for the test casing.

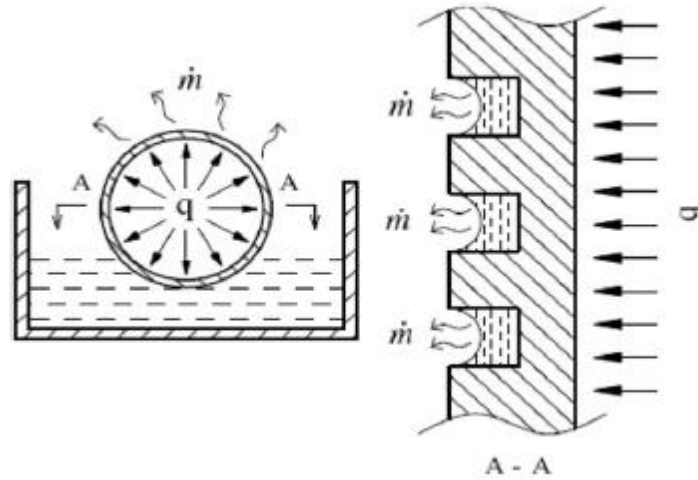


Figure 40: Illustration of the horizontal feed mechanism [19].

Table 15: Half-length small casing critical dimensions.

Casing ID	.02185 [m]
Casing OD	.02533 [m]
Casing Internal Length	1.524 [m]
Material	SS316

General

Test methodology specific to each configuration has been discussed in some detail in the preceding sections; however, there are some additional general methodological considerations which will be discussed here. All tests were conducted with some basic guiding constraints specific to the OTEC application; these constraints are listed in Table 3 and Table 4. The following general discussions apply to all tests and analysis where instrumentation allowed; however, this was most apparent in tests using the independent ammonia test loop.

Uncertainty in Results:

One significant issue which was present throughout all testing was uncertainty in test results. The target LMTD was 1.88 [K] and ΔT water through the evaporator was low (≈ 1.5 [K]). These small but critical values resulted in the need for highly precise temperature measurements. Uncertainty propagation analysis has shown that the dominant source of uncertainty is the evaporator water side temperature measurements. This is true for both LMTD and evaporator water side heat transfer. For this reason, results which demonstrate good energy balance are used to calculate overall heat transfer based on the condenser loop water measurements rather than the evaporator. This is appropriate because condenser water flow rate was much lower,

so ΔT was much larger than in the evaporator. Uncertainty propagation for a typical test case is shown in Figure 97 in the appendix. In order to reduce uncertainty in LMTD calculations due to evaporator water measurements, warm water was evaluated using 1/10 DIN RTD thermistors with a systematic error of around .03 [K].

Total instrument error was calculated as the result of the RMS equation for combining systematic and measured error and is illustrated below. The systematic error for a given piece of instrumentation was constant for a test point and could usually be acquired from manufacturer's documentation. Often systematic error was a function of the measured property, and this was accounted for when necessary.

$$\epsilon_{tot} = \sqrt{\epsilon_{systematic}^2 + \epsilon_{measured}^2}$$

$$\epsilon_{measured} = \sqrt{\frac{1}{n} \sum_{i=1}^n (x_i - x_{av})^2}$$

x_i = measured value at point i

n = total number of measurements in set

T-Type thermocouple measurement error was reduced by using bundles of 3 thermocouples at each measurement point. The uncertainty was assessed for these measurement points according to the following equation.

$$\epsilon_{T-Type\ bundle\ tot} = \frac{(\epsilon_{tot\ T1} + \epsilon_{tot\ T2} + \epsilon_{tot\ T3})}{3\sqrt{3}}$$

A significant effort was spent on temperature sensor calibration in order to further reduce the uncertainty caused – in all temperature dependent metrics – by systematic temperature sensor error.

In order to calibrate temperature sensors, a 1/10 DIN RTD was chosen with a known uncertainty, and used as a reference. All T-Type thermocouple bundles (T type thermocouples were always used to measure temperature points in bundles of 3) were connected to the data acquisition unit in the manner in which they would remain during formal testing. All sensors were placed in a water bath with well mixed stable thermal conditions. After steady state was reached, T-Type thermocouple voltage and the RTD reference temperature measurements were recorded. The water bath temperature was then adjusted for the next data point. A full range of temperature was tested parametrically, and the output measurements were plotted as shown in Figure 41. A linear regression was generated, and was used in future ammonia tests to estimate the systematic error of each thermocouple as a function of test temperature. This procedure reduced the single T-Type thermocouple uncertainty from the factory rated .5 °C estimate to between .1 °C and .4 °C.

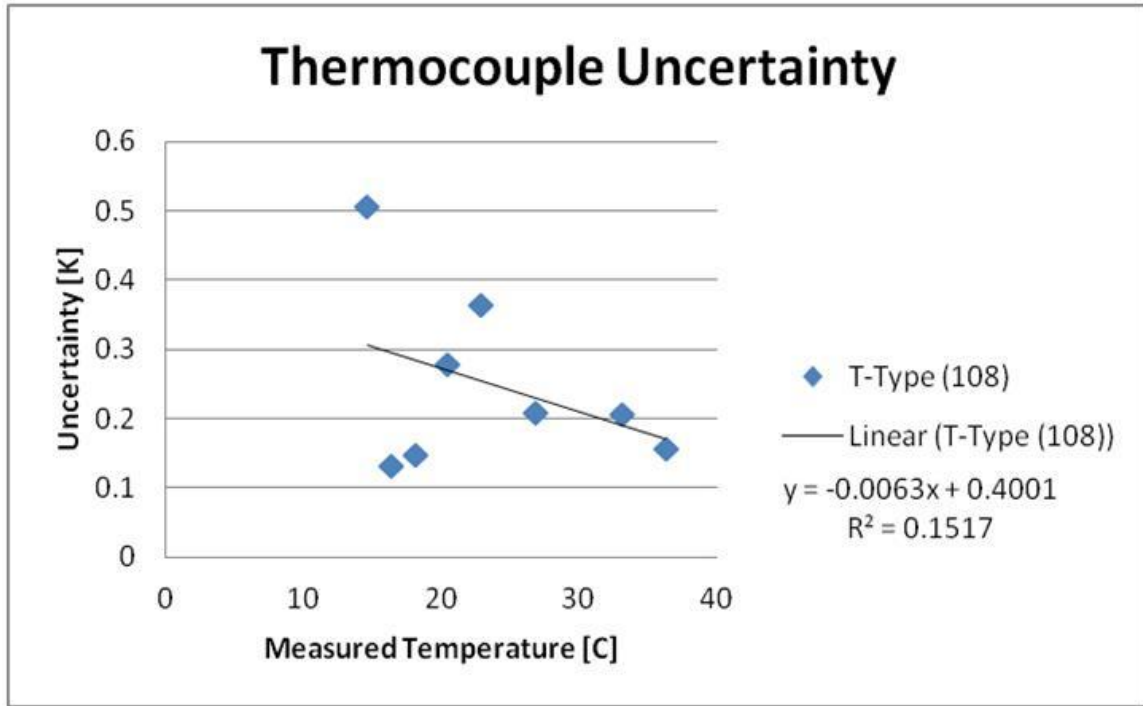


Figure 41: An example of a typical T-type thermocouple uncertainty calibration.

It is important to note that in all T-Type measurements it was necessary to record a known reference temperature to compensate for junction temperature offset within the data acquisition unit. During all ammonia testing, a 1/10 DIN RTD was paired with a designated reference T-Type bundle and set into a well-insulated box containing water at a stable temperature. The difference between the RTD and reference T-Type bundle measurement was used to correct the junction temperature offset for all thermocouple bundles in the test. The results of the efforts to control uncertainty, described above, were successful in keeping error limits of final calculated performance metrics to within 5%-10%; however, there were other efforts made to ensuring accurate reliable data, and are reflected in the comprehensive list below.

1. Calibrate sensors to achieve low systematic error
2. Use of bundled thermocouples to reduce systematic error at measurement point
3. Ensure stable operating conditions during data collection to ensure low measured error
4. Avoid very low flow rates and temperature differences during testing
5. Visually inspect data for logical trends and low random variation
6. Repeat test points to ensure repeatability and no large hysteresis effects
7. Only retain data with an associated total system energy balance below 10%

After filtering results, the energy balance of the retained data was $8.22 \pm 3.15\%$ for the $\frac{3}{4}$ " half-length horizontal ISTF tube in the small test casing, and can be taken as a typical value for all tests using the independent ammonia loop. Refrigerant side heat transfer coefficients were calculated using the Wilson plot derived water side heat transfer values, as described in the next section, and uncertainty for the Wilson plot values was accounted for in both heat transfer coefficients. Figure 42 and Figure 43 show typical uncertainty of the primary calculated results for the independent ammonia test loop.

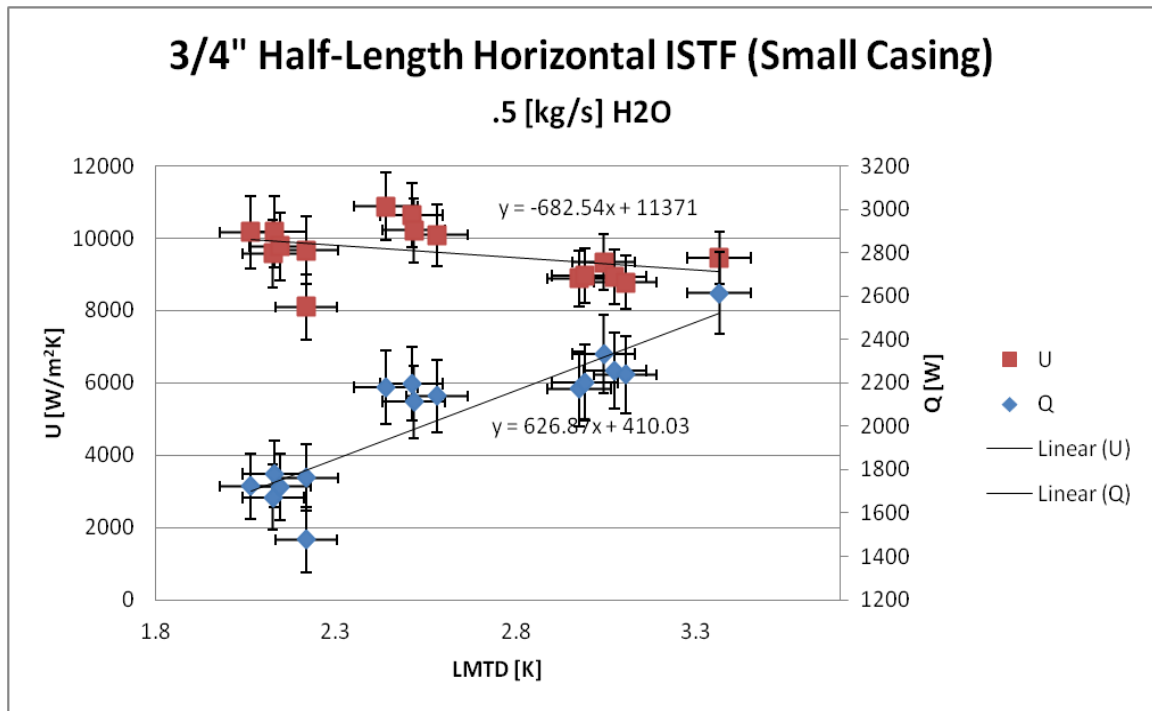


Figure 42: A typical example of uncertainty in U and Q .

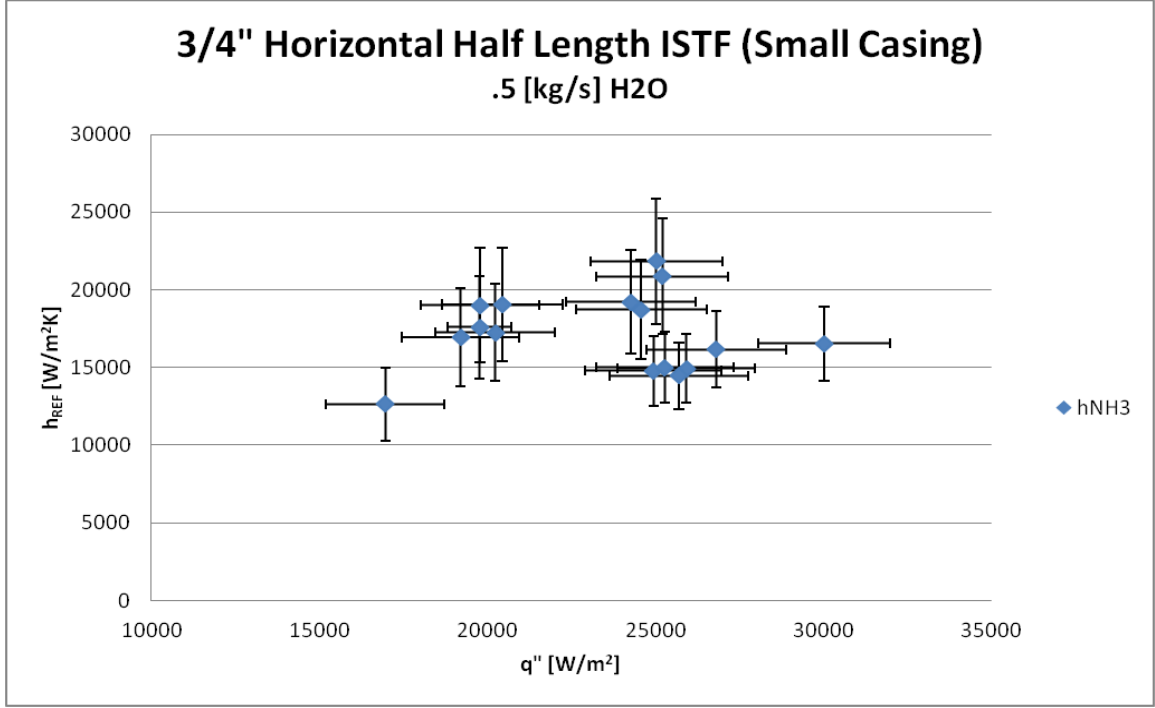


Figure 43: A typical example of uncertainty in href.

Wilson Plot:

The final topic of importance as it pertains to general test methodology is the use of the Wilson plot method. The Wilson plot is used to estimate the contribution of water side versus refrigerant side convective axial thermal resistance in the tubular heat exchanger. This method is useful in that it helps identify where overall performance is being limited, and by using a thermal resistance circuit model the refrigerant side heat transfer performance can be estimated. The Wilson plot method operates on the assumption that if conduction through the tube wall and the refrigerant side convective heat transfer coefficient are held constant, then the water side convective heat transfer coefficient is a linear function of the overall heat transfer coefficient and depends on water flow rate only [21]. This assumption is valid for the OTEC application because temperature and pressure do not vary enough to affect water properties significantly; thus, the following equations demonstrate that water side heat transfer coefficient is only dependent on mass flow rate.

$$\bar{h}_{H2O} = \frac{\bar{Nu}_L k_{H2O}}{L}$$

$$\bar{Nu}_L = f(Re_D, Pr)$$

$$Pr = \frac{C_{pH2O}}{k_{H2O}}$$

$$Re_D = \frac{\dot{m} D_h}{\mu_{H2O} A_c}$$

$$k_{H_2O}, C_{p,H_2O}, \mu_{H_2O} \approx \text{constant}$$

$$L, D_h, A_c = \text{constant}$$

$$\therefore Re_D = f(\dot{m}) \rightarrow \bar{h}_{H_2O} = f(\dot{m})$$

Therefore, regardless of the particular operating conditions on the refrigerant side, h_{H_2O} can always be predicted for a given water flow rate.

To use the Wilson plot method, an empirical test is conducted. By holding refrigerant side conditions constant, varying water flow rate, and calculating the overall heat transfer coefficient at each test point, a linear plot can be generated to find the coefficient (C_1) of the relationship between h_{H_2O} and U [20]. This is demonstrated with the equations below, and the actual linear relation plot used for the 3/4" half-length tube shown in Figure 44.

$$h_{H_2O} = C_1 u_{H_2O}^n$$

$$n = .82 \text{ (assumes fully turbulent flow [21])}$$

$$C_1 = \text{slope of Wilson plot linear curve fit}$$

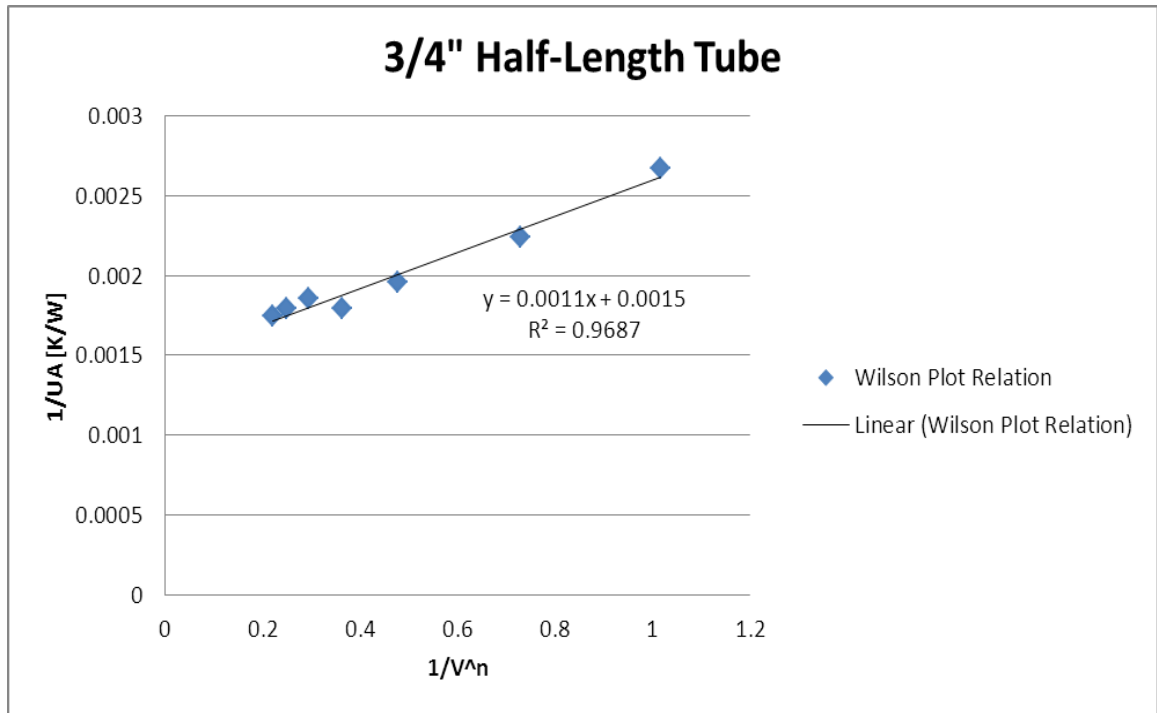


Figure 44: Linear relation for Wilson plot using 3/4" half-length tube.

In the case above, C_1 is equal to .011. Now that h_{H_2O} is known for a given water flow rate, the axial 2D thermal resistance network below can be used to find the refrigerant side heat transfer coefficient.

$$\frac{1}{UA_s} = \frac{1}{h_{H_2O} A_i} + R_{wall} + \frac{1}{h_{NH_3} A_o}$$

$$R_{wall} = \frac{\ln \frac{r_o}{r_i}}{2\pi L k_{wall}} \approx \text{constant}$$

As an interesting note, the linear fit shown in Figure 44 is merely a plot of this thermal resistance network equation; the y-intercept of the plot reflects the average value of $(R_{NH3} + R_{wall})$ for the particular test conditions that were chosen during data collection, and the slope (C_1) is related to h_{H2O} as described above. The Wilson plot method is very useful. Due to the independence of h_{H2O} from temperature, h_{H2O} can be assumed to hold to this relationship in all future tests, regardless of refrigerant side conditions, so long as the same evaporator tube is used. It can also be used to find h_{NH3} and determine whether or not the tube is limited by water or refrigerant side convection.

Chapter 4: Experimental Results and Analysis

Ethanol Testing

Vertical Capillary Feed Design:

Testing was performed in order to develop a feed tube which adequately supplies liquid to the vertically oriented evaporator surface in both the 2" one foot and $\frac{3}{4}$ " half-length applications. Testing was performed in the open tube configuration, and tubes were visually inspected for even and adequate wetting. When it was apparent that tubes would not dry out or flood during operation near the target test heat flux, estimates of overall heat transfer coefficient were used to compare feed tube-evaporator combinations. In general, test conditions were held constant so that the performance of the various feed tubes could be more easily compared. As input Q could be held constant between tests by controlling the 3000 [W] maximum electric water heater, better performing tubes (higher U) had lower LMTDs which indicated optimal wetting of the evaporator surface by the tested feed tube.

Figure 45 shows some of the more successful feed tube concepts tested on the 2" one foot tube. It is interesting to note the first two tests on the left hand side of the figure. These tests were conducted using the same type of feed, only in the second from the left there were two feeds positioned 180° around the circumference of the evaporator from each other. The intention was to determine whether or not the evaporator surface would benefit from additional feeding, at the furthest point from the original feed, where the surface capillary structure was least able to supply fluid in high heat flux conditions. Figure 46 shows a comparison of the two feed tubes developed for testing on the $\frac{3}{4}$ " half-length surface.

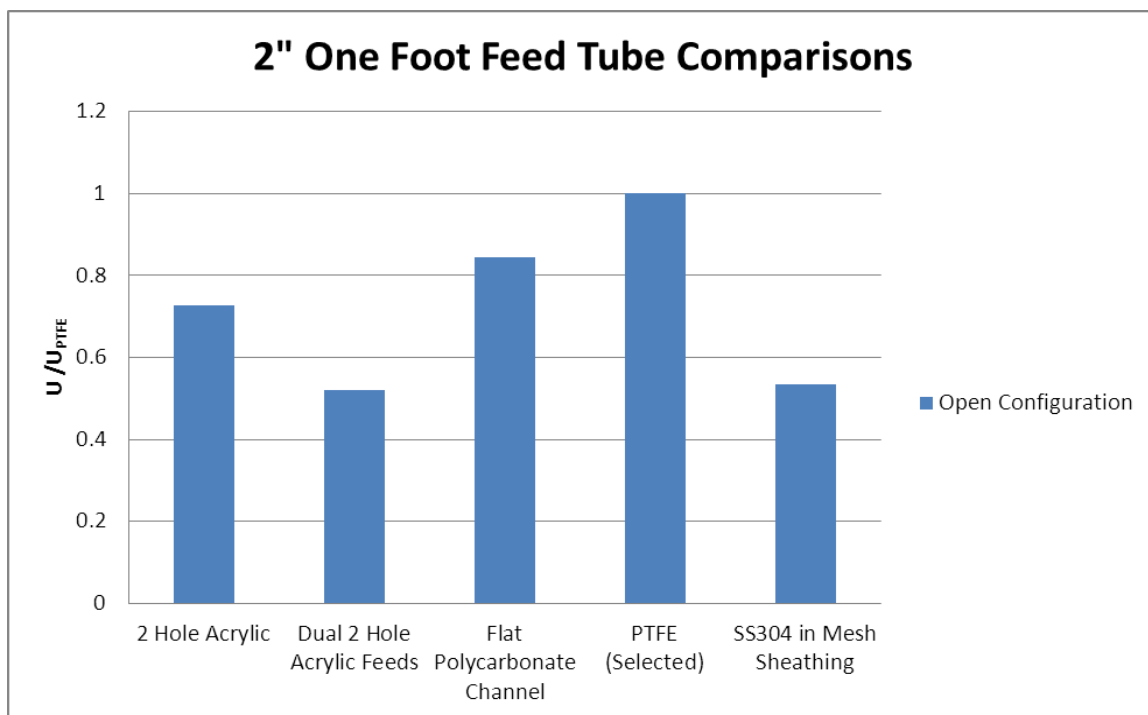


Figure 45: A selection of feed tubes tested on the 2" one foot evaporator.

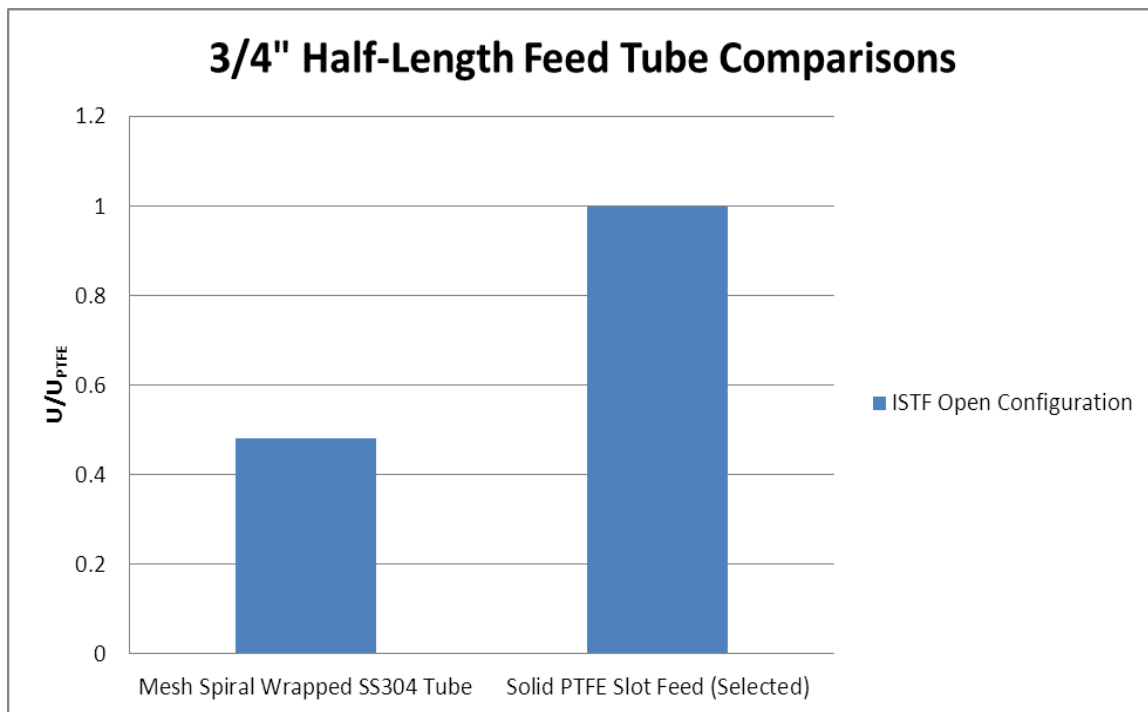


Figure 46: Comparison of half-length feed tubes for the 3/4" ISTF evaporator.

2" One Foot Proof of Concept Tube:

Uncertainty in the 2" tube ethanol data was very high in general, so there is little reliable data to report. Most testing was conducted in order to compare various configurations so as to quickly identify which adaptations caused relative apparent improvements in performance. After successful alterations were identified, focus moved very quickly to the next task. Later ethanol testing with the half-length tube employed the use of better instrumentation, and more time to assess performance was afforded, so there is more to report on the half-length tube using ethanol. After the failure of the integrated ammonia loop, testing was conducted to confirm that the test casing new external separator was able to function. This testing utilized better instrumentation, and resulted in data with slightly lower uncertainty. Average best performance is reported in Table 16.

Table 16: 2" one foot tube with new external outlet separator using ethanol.

Ethanol	LMTD	Q	U
2.34 [g/s]	2.17 [K]	722 (+/- 2.86) [W]	10312 (+/-1017) [W/m ² K]

3/4" Half-length Tube Vertical Testing:

Prior to ammonia lab deployment, pre-testing was conducted on the half-length tube PTFE channel feed combination in the closed configuration. The results of this test, shown in Figure 47 indicate that the tube is functioning in a reasonable range. The appearance of a possible optimum just below 3 [g/s] shows that the tube is likely wetting properly, with a clear tapering off in performance with increased flow rate as flooding commences. Ideally further testing could have produced better resolution and more statistical certainty; however, time constraints dictated that it was necessary to begin installation in the ammonia independent test loop and performance was deemed acceptable. The results of this test, which used the plain fin tube, are in line with the lower performance numbers later gathered from the plain fin tube during ammonia testing. This is discussed in later sections.

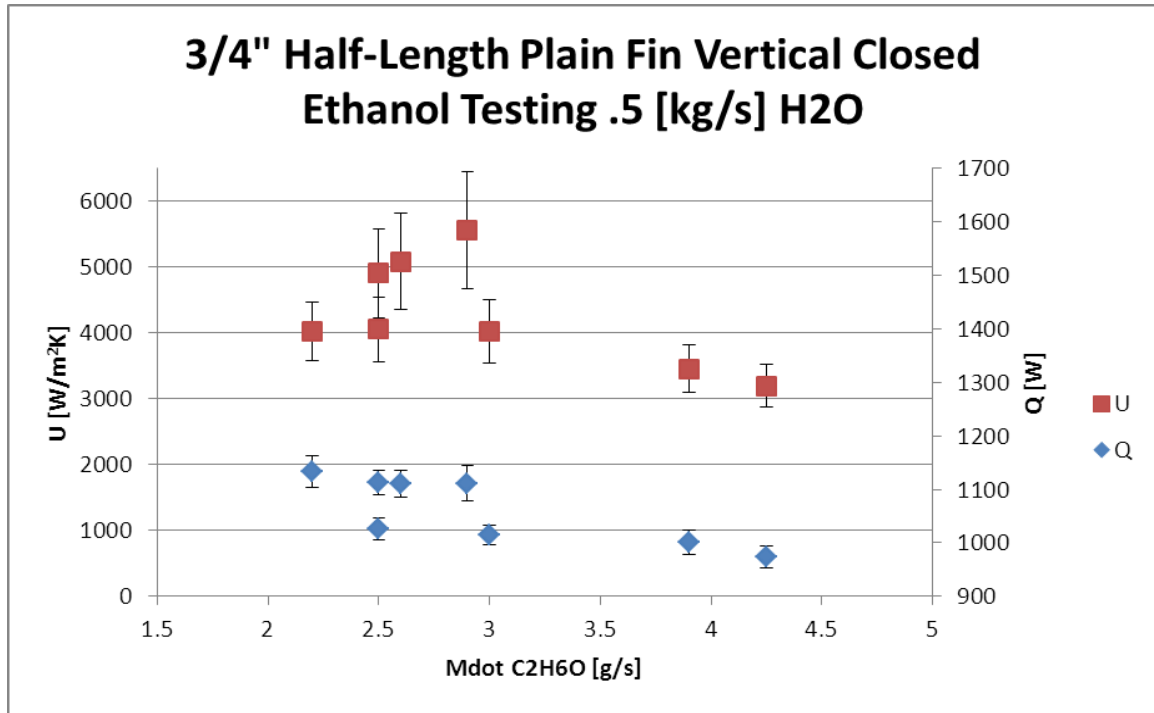


Figure 47: Ethanol pre-testing of the half-length vertical tube in the closed configuration.

Ammonia Testing

2" One Foot Proof of Concept Tube - Integrated NH3 Loop:

As mentioned in the methodology section, the integrated ammonia test loop was abandoned after a short time due to issues with ammonia flow rate oscillations and test section flooding. This failure led to the development of the external outlet separator, a modification that was used with great success in preventing test section flooding during later tests. The other issue, ammonia delivery flow oscillations, made it very difficult to establish steady state test conditions and produced artificially large measured error. It was discovered that these oscillations were due to the existing ammonia pump and PID control. The existing diaphragm pump was oversized for our application and designed to deliver 30 [g/s] of ammonia. Running this diaphragm pump at the low flow rates required for our heat flux capacity assuming 100% evaporating mass flow (≈ 1 [g/s]) caused the oscillations visible in Figure 48. It is noteworthy that even at a flow rate of 6 [g/s] this severe oscillation was observed; severity increase for lower flow rates. As a result of the high measured error and large energy balance difference, no meaningful performance data was reported using ammonia until the independent test loop was installed.

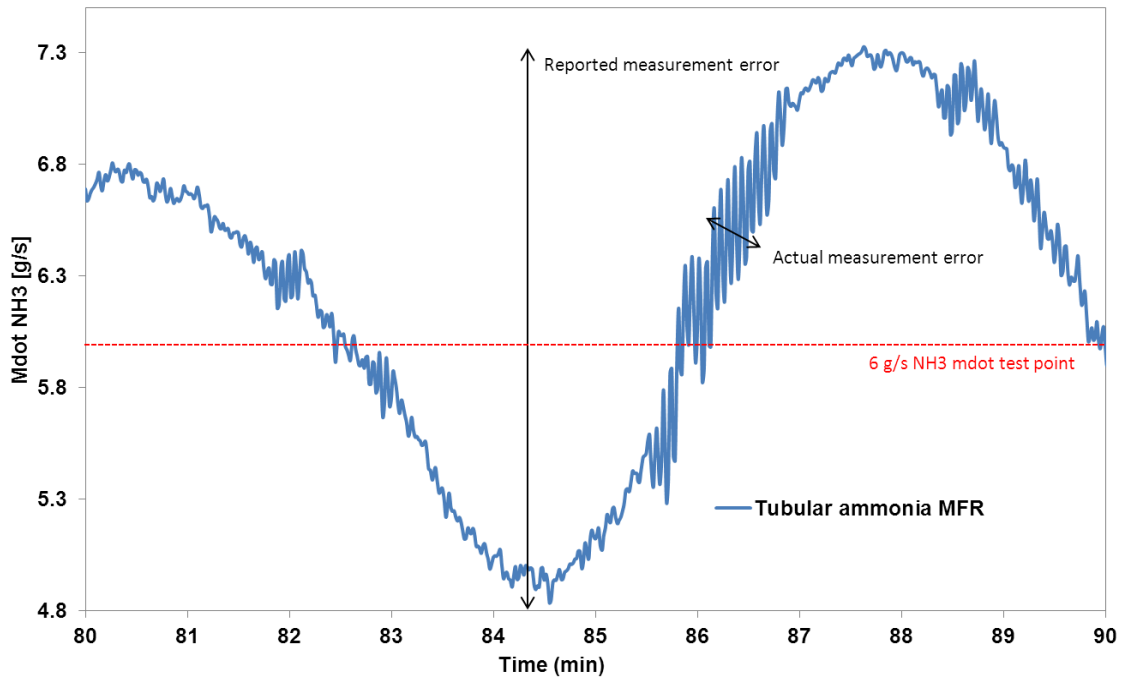


Figure 48: Oscillations in ammonia delivery flow rate due to oversized diaphragm pump and PID control.

Upon installation of the new independent ammonia test loop, the most valuable data was gathered. Five different test configurations were conducted using 3 different surfaces. The test configurations analyzed are listed in Table 17.

Table 17: Configurations tested using the independent ammonia test loop.

1. 2" one foot vertical tube
2. 3/4" half-length plain fin tube in horizontal orientation using the small test casing
3. 3/4" half-length ISTF tube in horizontal orientation using the small test casing
4. 3/4" half-length ISTF tube in horizontal orientation using the large test casing
5. 3/4" half-length ISTF tube in vertical orientation

The results of these five test configurations, which targeted specific OTEC operating conditions, are now promulgated. Some discussions, and additional results using a wider range of LGTE relevant operating conditions, are in following section.

2" One Foot Proof of Concept Tube – Independent NH3 Loop:

The first tube tested using the independent test loop was the 2" tube. Initial results for this tube were lower than expected. Upon disassembly of the test section, it was discovered that a significant amount of vacuum pump oil had contaminated the loop. After cleaning the 2" one foot test section and the independent loop thoroughly with pentane, the loop was re-tested and results proved far superior to the previous

data. The exact concentration of pump oil is not known; however, it certainly constituted a very small mass fraction of the working fluid. The contaminated tube results are shown in Figure 49 and after cleaning in Figure 50. Figure 51 shows oil contamination on the surface of the evaporator, and Figure 52 shows pentane used in loop cleaning with the cloudy oil filled pentane visible on the right.

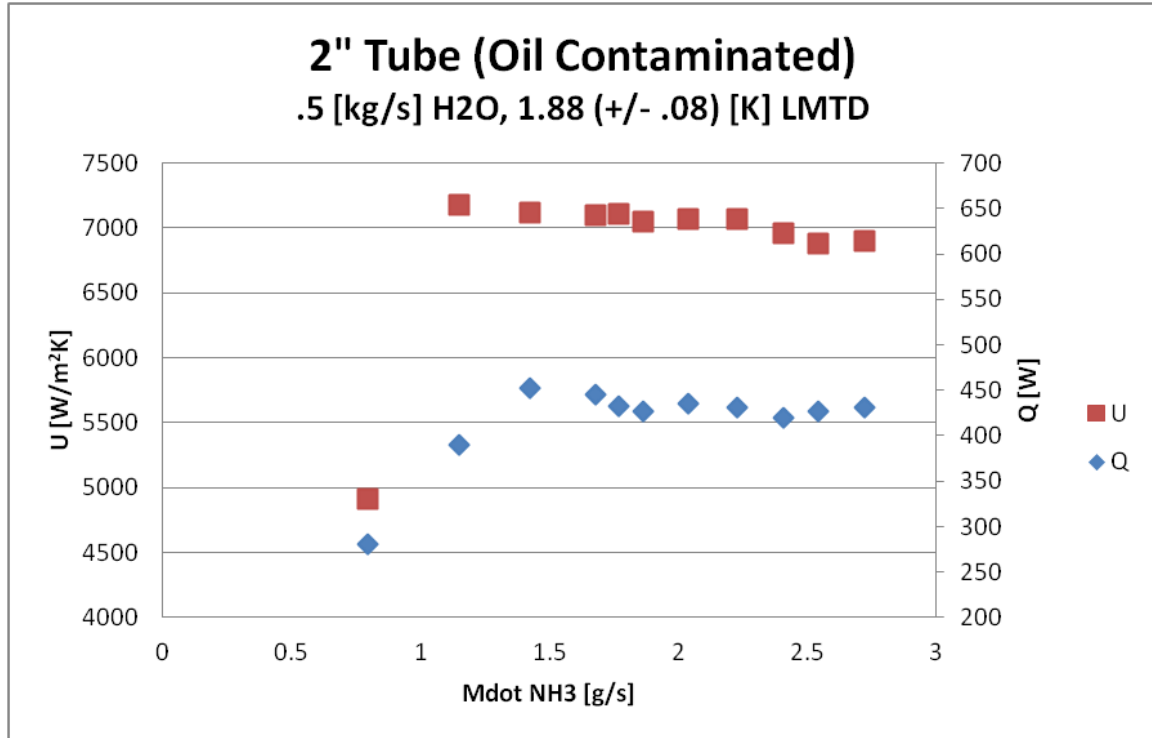


Figure 49: 2" 1 foot tube independent loop results (oil contaminated).

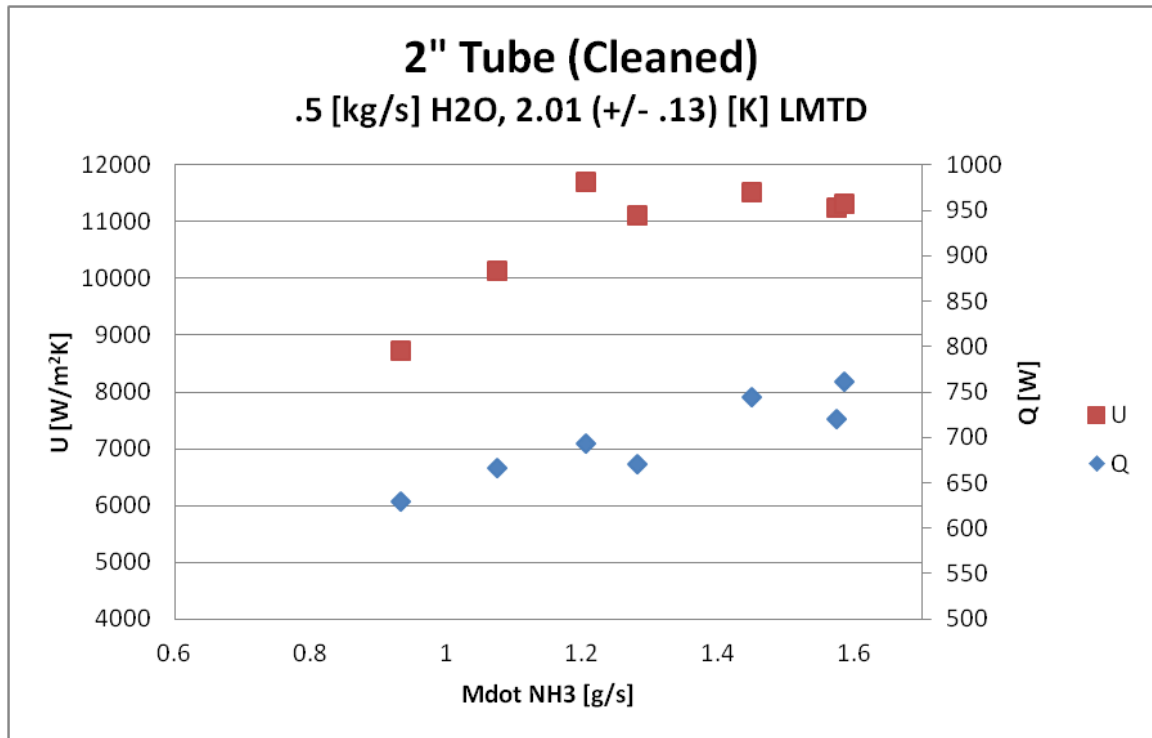


Figure 50: 2" 1 foot tube independent loop results (cleaned).

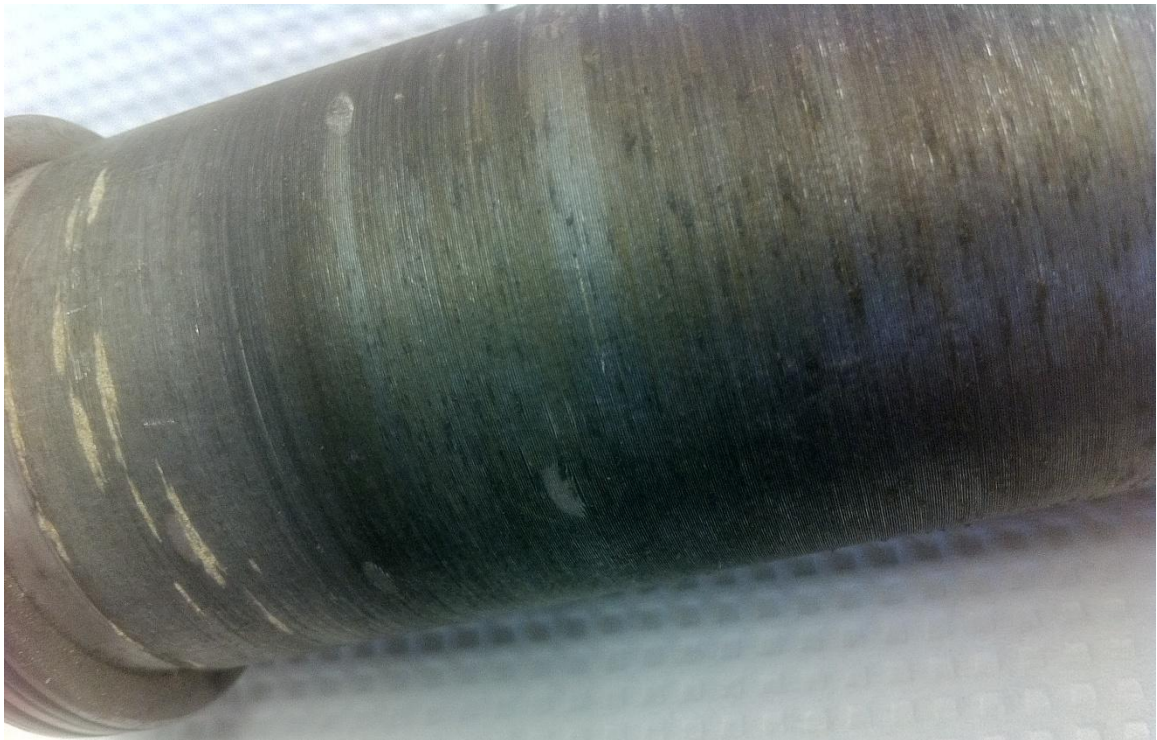


Figure 51: Oil contamination visible on 2" tube surface.



Figure 52: Pentane before cleaning independent test loop (left) and after removing oil (right).

$\frac{3}{4}$ " Half-length Horizontal Plain Fin – Independent NH₃ Loop:

Results for the half-length plain fin tube in horizontal orientation using the small casing are given in Figure 53. In this study, outlet orientation was varied, meaning the tube was rotated axially so that the outlet port was 45° (down), 90° (side), and 180° (top) from bottom dead center. It was surmised that varying the outlet orientation controlled the level of the liquid pool inside the casing. With the outlet port toward the bottom, liquid would be more likely to exit the test casing before flooding occurred. With a top outlet orientation, the entire casing could flood with liquid and only exit the tube at the rate of delivery; however, it is possible that complete flooding did not occur due to liquid being driven out of the casing by high velocity vapor. Results show that outlet tube orientation has a negligible effect on evaporator performance; however, ammonia delivery rate shows a pronounced effect. Optimum performance was observed at around 1 [g/s] of ammonia delivery, which is in good agreement with the expected mass demand for ammonia evaporating the measured ≈ 850 [W] of heat. The indication is that lower mass flow rates lead to portions of the surface drying out, and higher flow rates began to flood the surface. This is some indication that outlet orientation did not have the control of liquid pool level as it was thought. Heat transfer and overall heat transfer coefficient for the 90° side outlet orientation is shown in Figure 54.

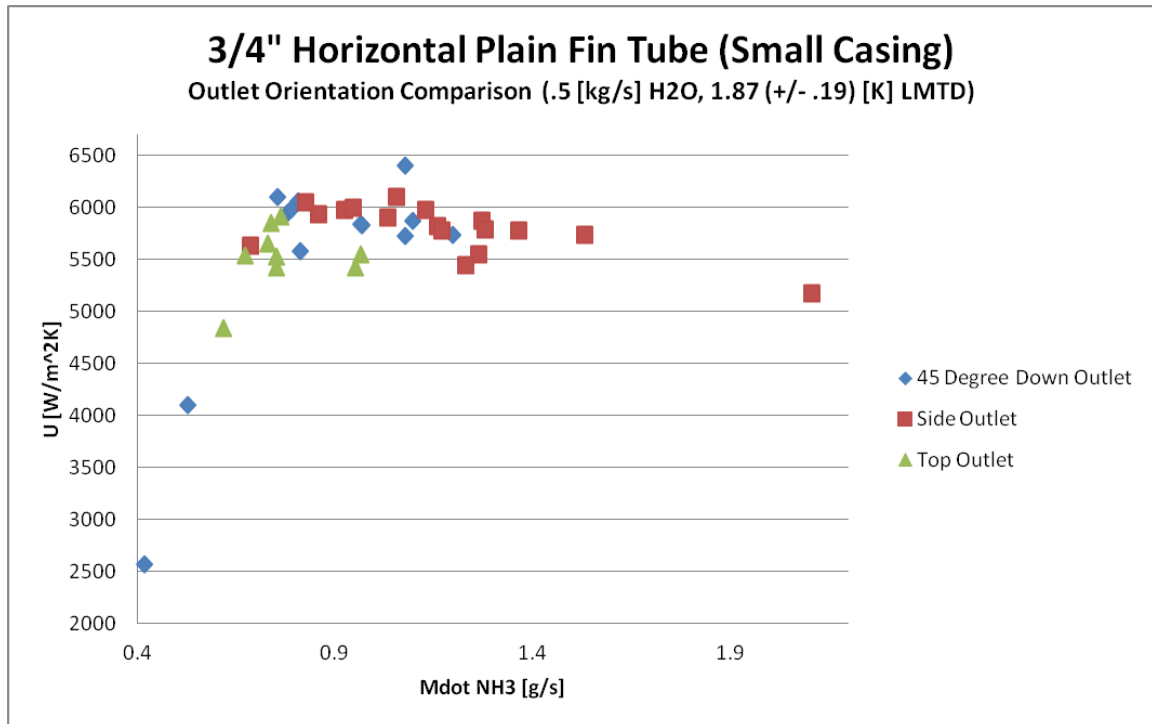


Figure 53: 3/4" horizontal plain fin (small casing) outlet orientation variation.

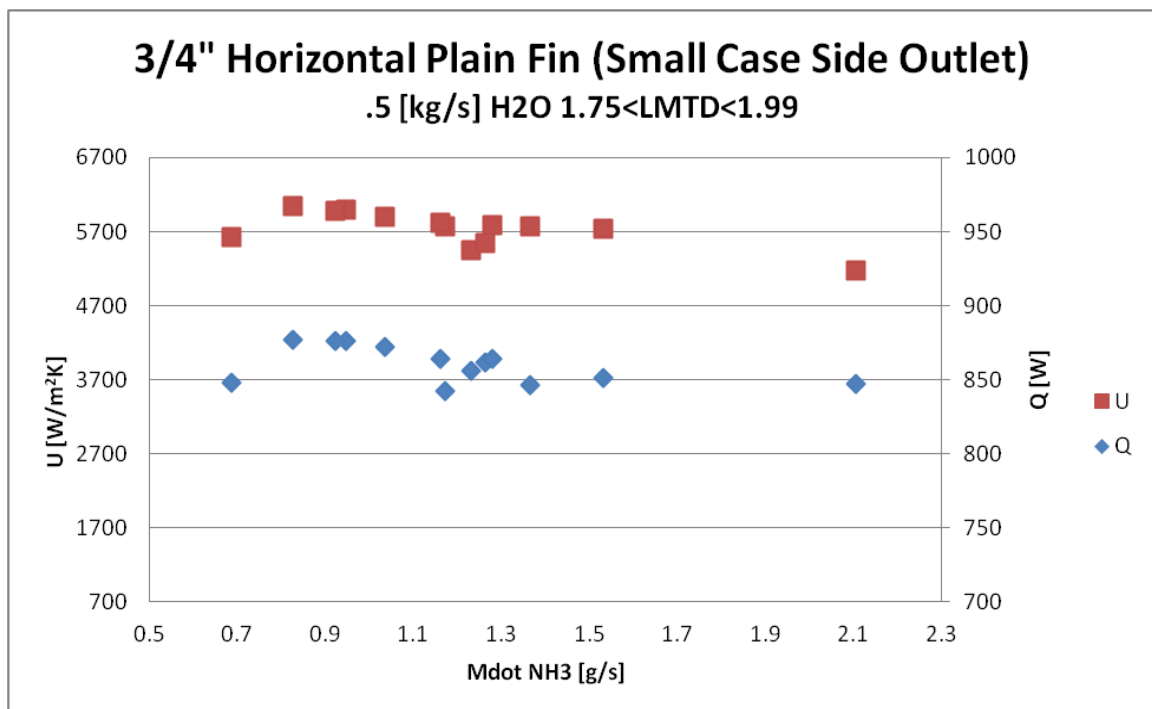


Figure 54: 3/4" Half-length horizontal plain fin results for side outlet.

3/4" Half-length Horizontal ISTF (Small) – Independent NH₃ Loop:

The $\frac{3}{4}$ " half-length ISTF tube tested in the horizontal orientation in the small test casing performed the best of all the tested surfaces. Results from this evaporator are shown in Figure 55.

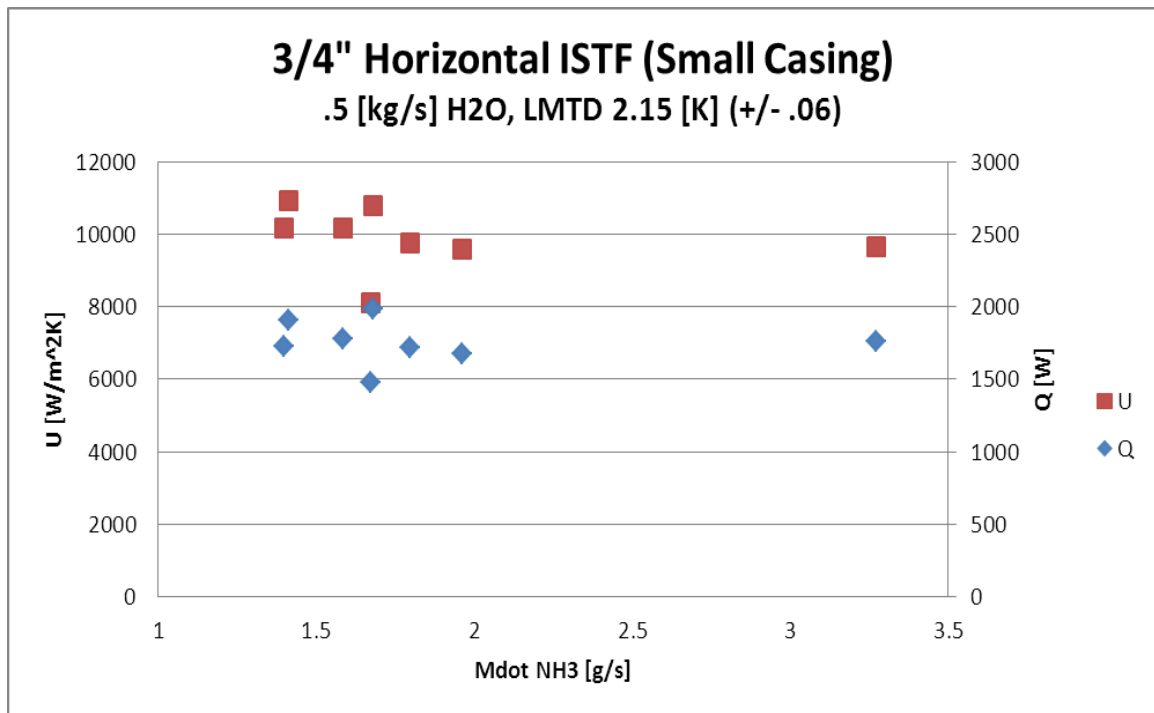


Figure 55: $\frac{3}{4}$ " half-length ISTF horizontal small casing results.

$\frac{3}{4}$ " Half-length Horizontal ISTF (Large) – Independent NH₃ Loop:

The performance of the $\frac{3}{4}$ " half-length ISTF tube in horizontal orientation was greatly reduced when the tube was changed from the small to the large test casing. Results from the large casing tests are shown in Figure 56.

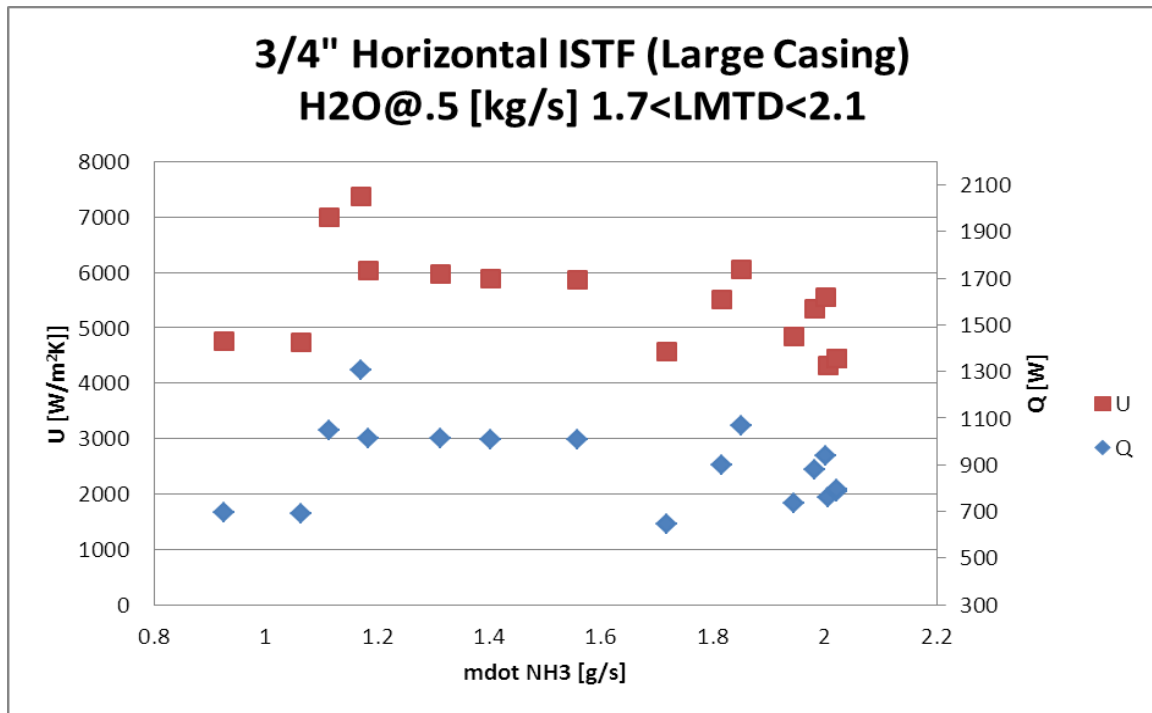


Figure 56: 3/4" half-length horizontal ISTF large casing results.

3/4" Half-length Vertical ISTF – Independent NH3 Loop:

The 3/4" half-length vertical test results performed slightly better than the horizontal tests using the same evaporator and test casing shown above, albeit less than with the horizontal small casing. Results for this tube are shown in Figure 57. One important note is that the feed tube for this half-length configuration was developed against a tight schedule, and further investigation into an optimum design for the half-length feed could potentially deliver superior results.

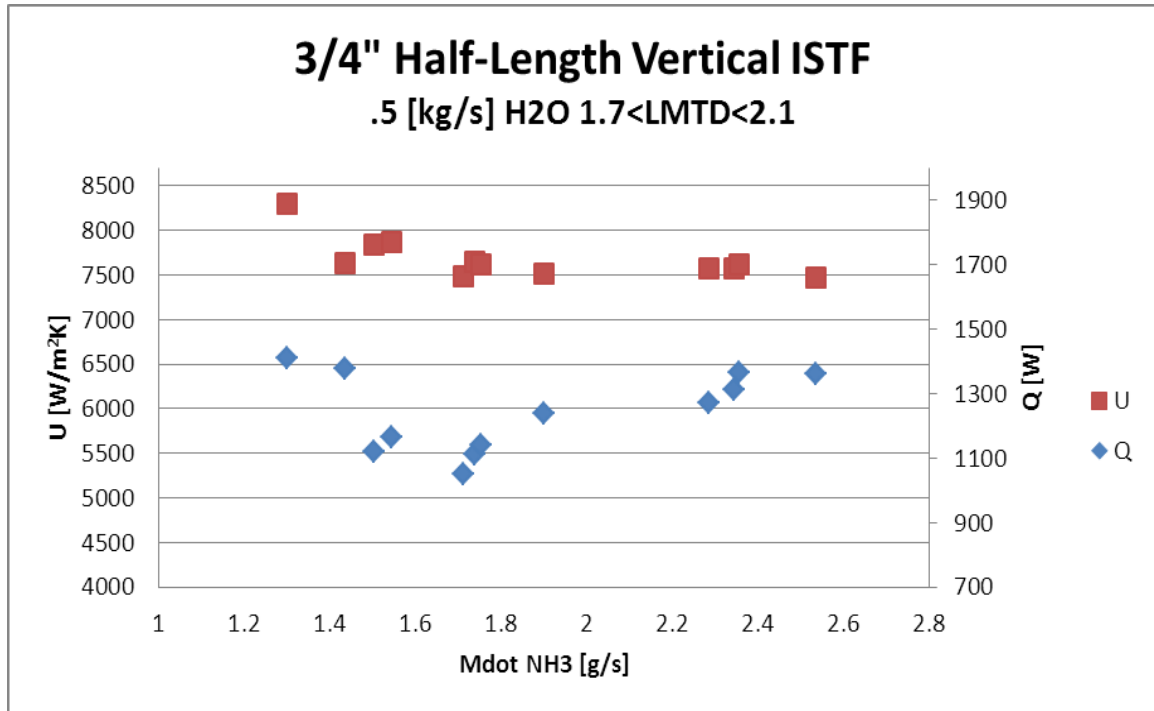


Figure 57: 3/4" half-length vertical test results.

Wilson Plot Results:

Results of the Wilson plot for the 2" and 3/4" tubes are shown in Figure 58. It is important to remember that the 2" tube contained a water side insert, so although the water side heat transfer coefficient is superior for a given flow rate, the hydraulic diameter is too small for OTEC applications due to the threat of bio-fouling and this tube was tested solely as a proof of concept for the vertical capillary feed. Figure 59 shows good agreement between the correlational prediction of the 3/4" tube water side performance and the Wilson plot results.

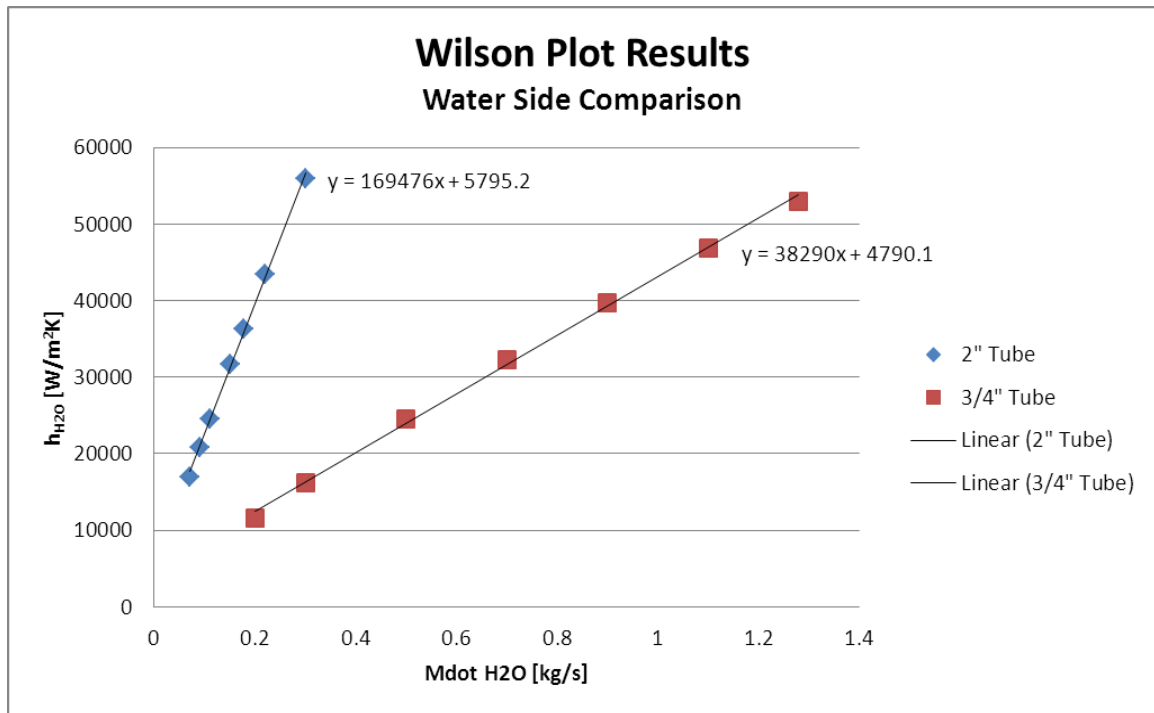


Figure 58: Wilson plot results for water side comparing 2" and 3/4" tubes.

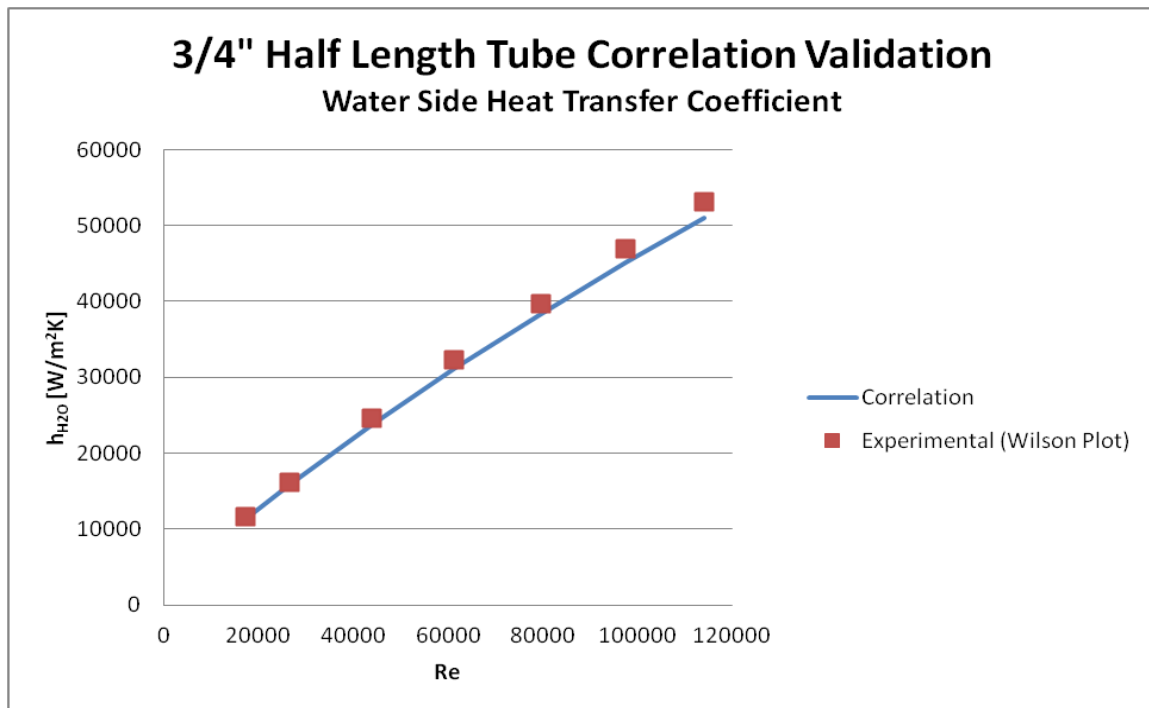


Figure 59: 3/4" Wilson plot results vs. manufacturer's correlation.

In all cases, evaporators were refrigerant side limited. Increasing the water flow rate had varying impacts on overall heat transfer performance. This is discussed in more detail in the discussion section regarding water flow rate. Figure 60 shows

the degree of refrigerant side limitation for the horizontal plain fin tube, and Figure 61 shows the same for the horizontal ISTF tube using the small test casing. Both figures demonstrate results at the .5 [kg/s] flow rate.

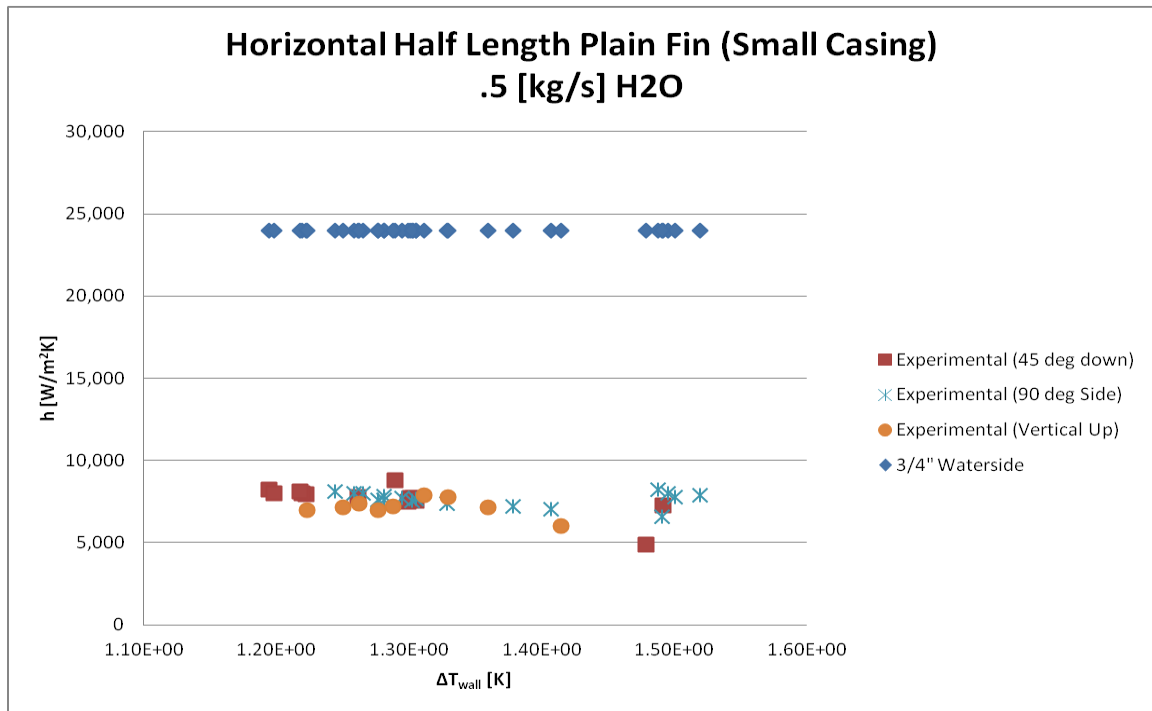


Figure 60: 3/4" horizontal half-length plain fin refrigerant side limitation.

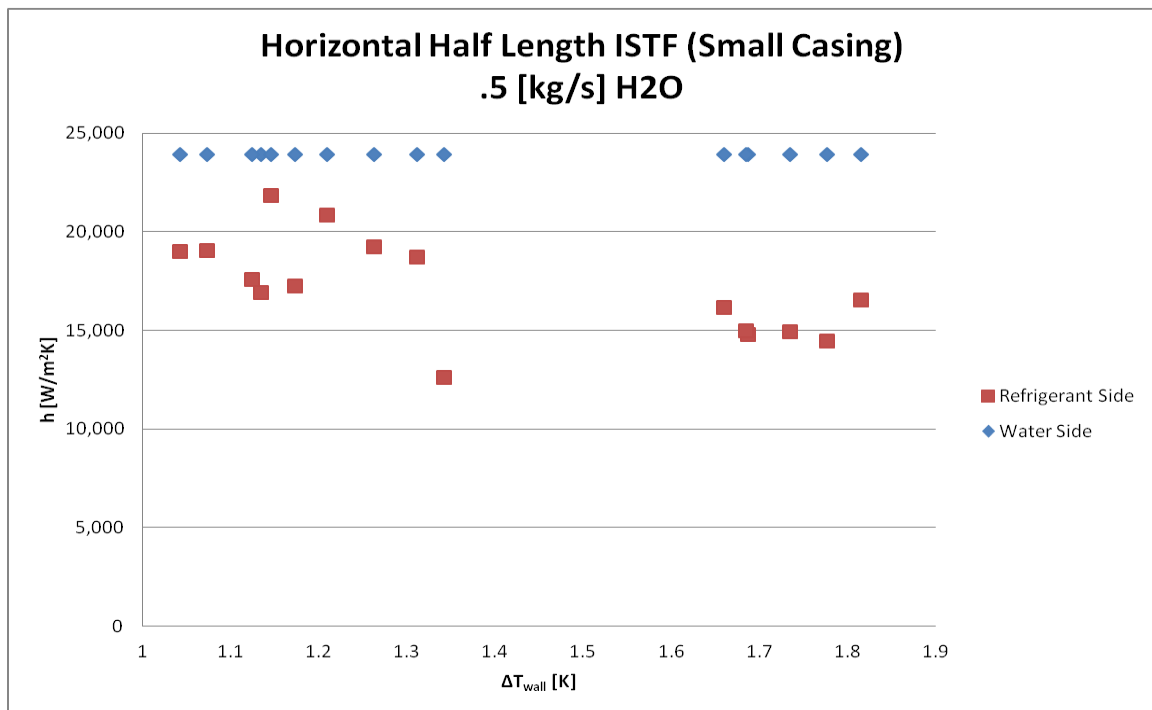


Figure 61: 3/4" horizontal half-length ISTF refrigerant side limitation.

Pressure Drop:

Pressure drop is a major concern for LGTE applications as the low energy potential mandates minimal pumping power losses in order to produce net positive power. Results in this study show that pumping power losses are nearly negligible for the refrigerant side, but some improvements could be realized by further optimizing water side potential. Figure 62 shows measured pressure drop curves for the water side on both the 2" and $\frac{3}{4}$ " tubes. Noting that the 2" tube has a water side insert, it is obvious why the short and wider tube meets the pressure drop constraint at a much lower flow rate than the $\frac{3}{4}$ " half-length tube without insert.

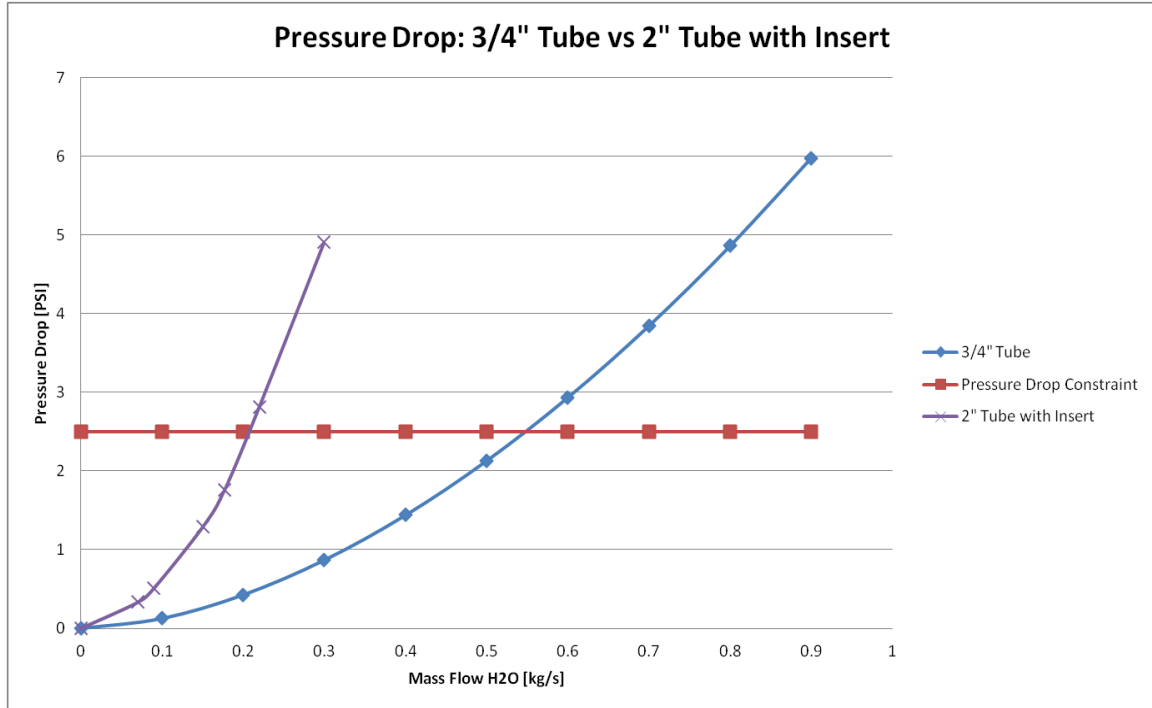


Figure 62: Water side pressure drop for both 2" and $\frac{3}{4}$ " tubes.

Figure 63 shows good agreement between the $\frac{3}{4}$ " tube and the manufacturer's correlation for this tube, which accounts for water side surface enhancement. There is no correlation available for the 2" tube as the water side insert was custom made. Figure 64 shows refrigerant side pressure drop for half-length tube. Both vertical and horizontal configurations are shown as to compare the pressure drop for both feed tube concepts. As is apparent, there is only a negligible loss for both cases at the flow rates tested, with no significant difference between feeds.

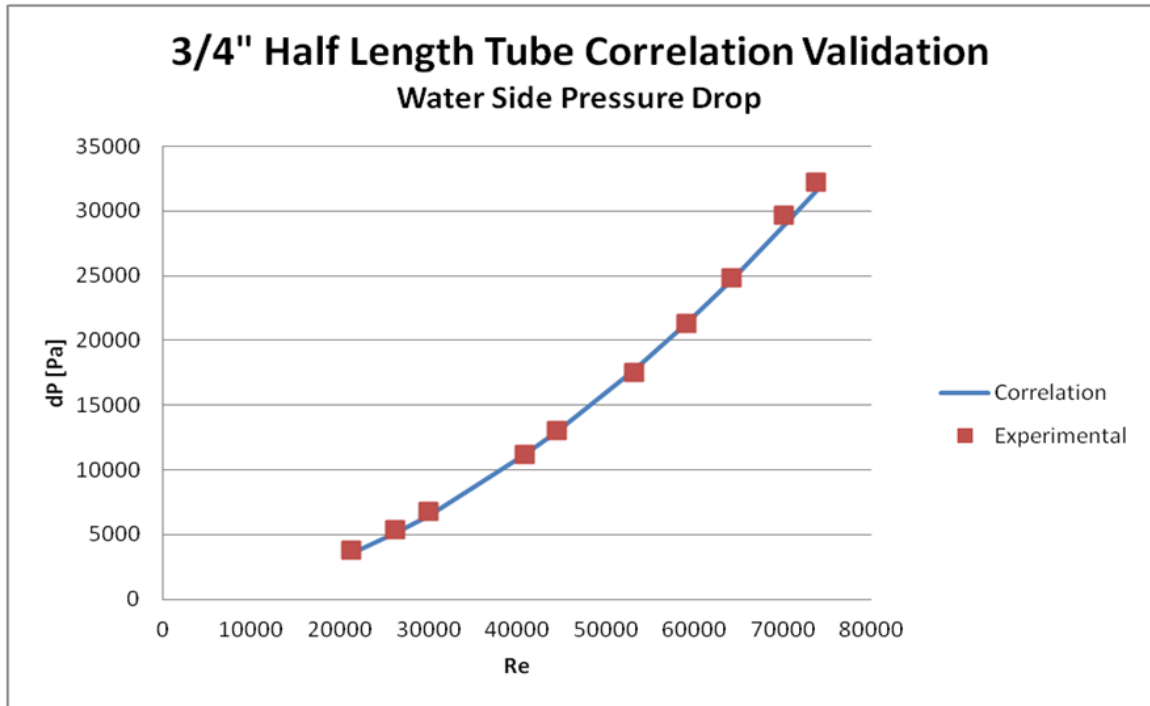


Figure 63: Water side pressure drop measurement validation with manufacturer's correlation.

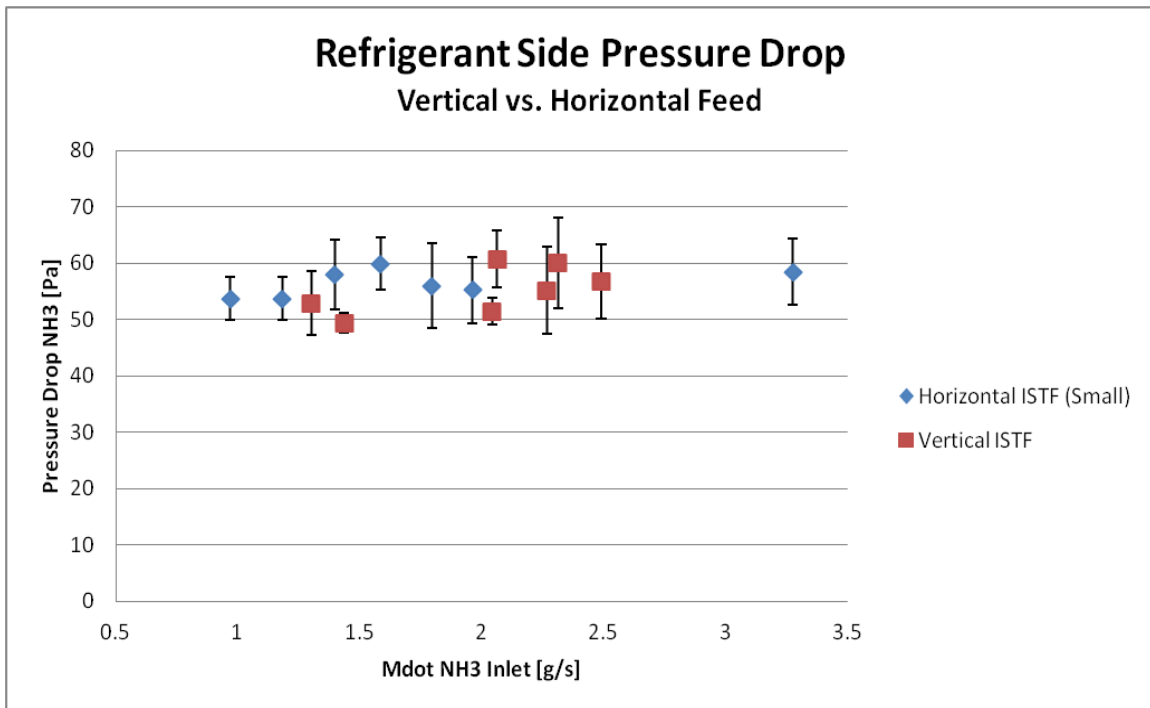


Figure 64: Refrigerant side pressure drop for both half-length feed concepts.

Chapter 5: Discussion and Analysis

Performance Comparisons

A summary of average performance characteristics for the test configurations conducted using the independent ammonia test loop is shown in this section. All results reported are near the 1.88 [K] LMTD OTEC target. The charts below show the average values, as well as the full range of results distributed in the data sample...not the data uncertainty. Figure 65 shows the total heat transfer of the 4 half-length tube configurations that were tested with the independent ammonia loop.

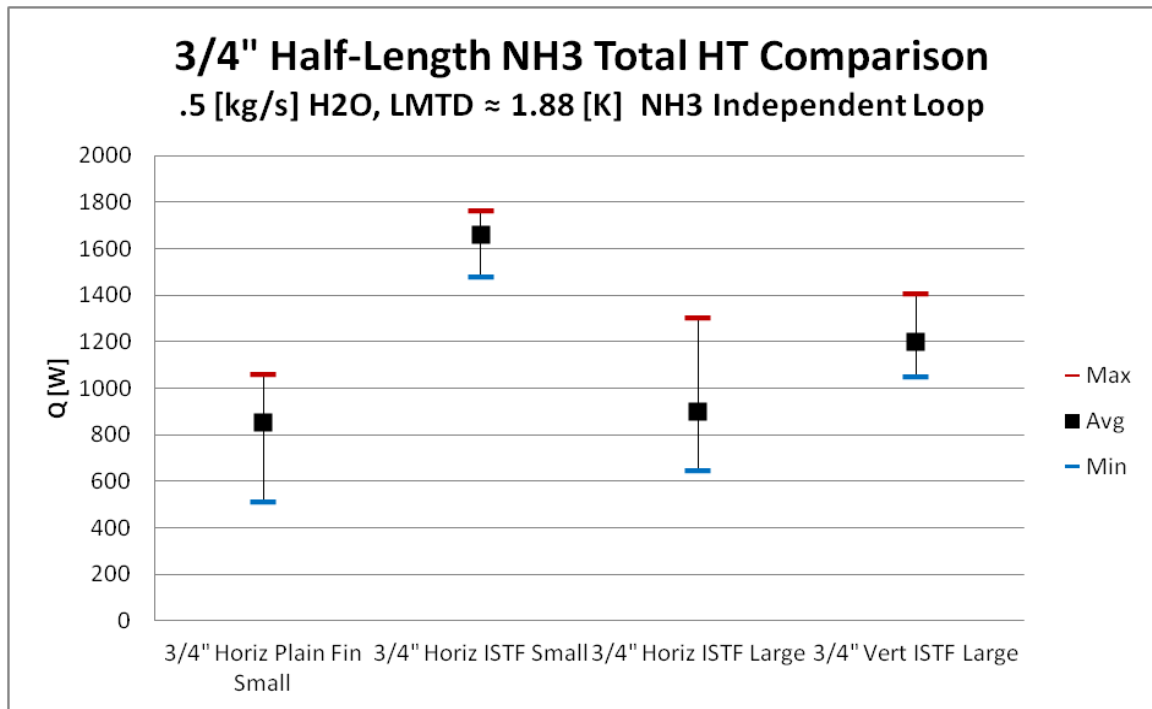


Figure 65: Heat transfer results comparing 3/4" tubes using NH3.

Figure 66 compares overall heat transfer coefficient for all independent loop test configurations. Keep in mind the significant advantage of the water side heat transfer coefficient in the 2" one foot tube due to the insert.

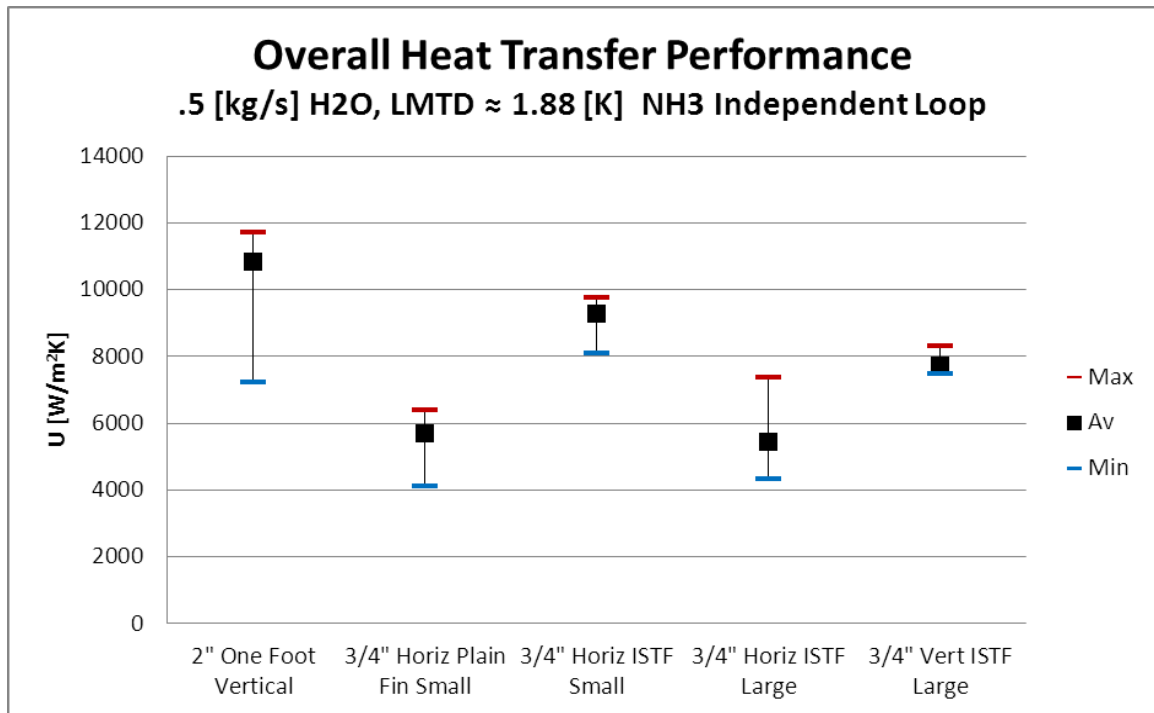


Figure 66: Overall heat transfer coefficient comparing all tubes using NH₃.

Figure 67 shows how the refrigerant side of the tubes performed in the various configurations. Here the clear advantage of the 3/4" horizontal ISTF tube with small test casing is visible relative to the other 3/4" tubes. It is also clear that the 2" tube depends on its superior water side performance in order to compete for best overall thermal performance. This is evident when observing the refrigerant and water side heat transfer coefficients in the neighboring charts. The 2" tube shows lower refrigerant side heat transfer than the 3/4" horizontal ISTF tube in the small test casing; however, overall the 2" tube performs better due to its higher water side heat transfer capability. This is caused by the advantage of the water side insert, for the 2" tube, which is not a practical technology for applications like OTEC where fouling in small flow areas is of concern.

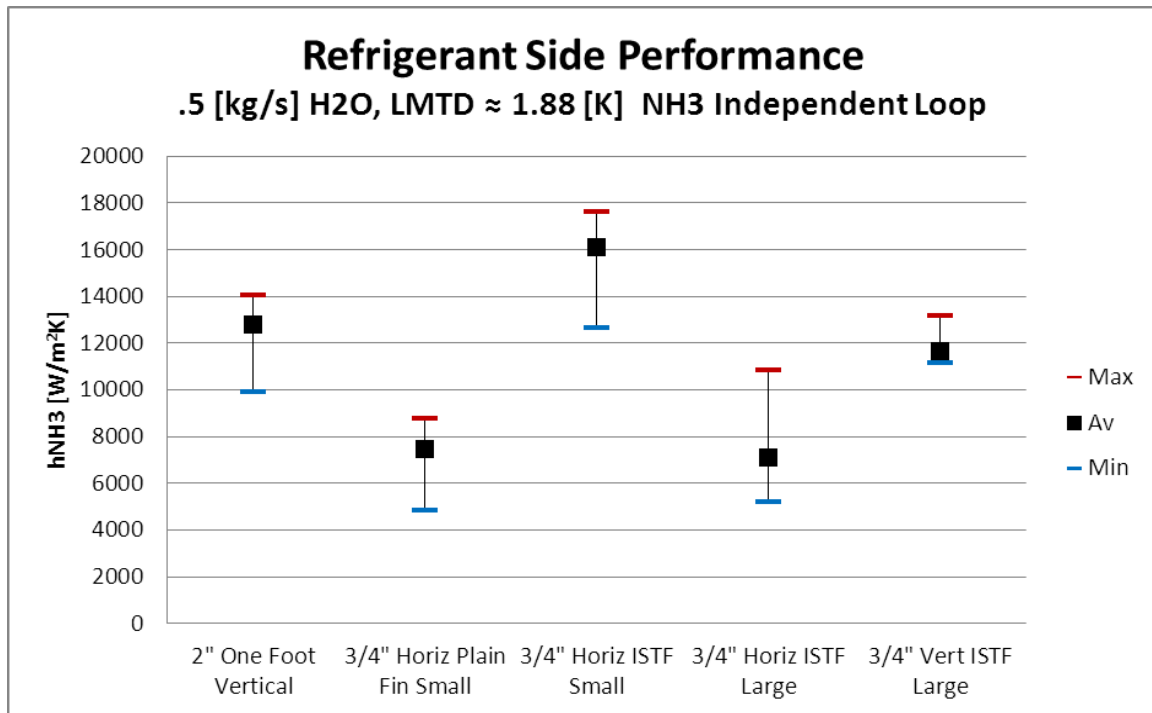


Figure 67: Refrigerant side heat transfer coefficient comparing all tubes using NH3.

Factors in Performance

Feed Tubes:

Ultimately channel (slot) feed tubes were selected for both the half-length and one foot tube applications. Wick feeds exhibited catastrophic failure immediately when boiling was initiated. Boiling readily took place within the wick itself; and, the wick dried out, no longer acted as a capillary supply path. Liquid guides underwent a similar type of failure as wicks when boiling occurred. However, a liquid guide – being a solid surface – does not dry out in the same way that a wick does. The liquid seemed to either detach from the evaporator and travel over the surface of the guide, or avoid the guide completely. In both cases, liquid could be observed boiling and spreading randomly across the evaporator surface flooding some portions and drying out others completely.

Channel (slot) feed tubes handle boiling better. Like the other options, they work very well without boiling and experience a decrease in performance during onset of bubble formation; however, this decrease is not the same as the catastrophic failure experienced by other designs. In most cases the feed tube is still able to supply fluid to the surface evenly; however, the capillary structures on the surface itself can begin to fail to conduct liquid all the way around the circumference of the tube. This surface wetting failure seems to vary with geometry, fluid, superheat, and heat flux; however, the basis for this statement is visual observations during ethanol tests and should be further investigated before it is confirmed.

In general, the channel feed tube design seems to succeed for two reasons: the delivery fluid is thermally insulated from the surface until it is introduced to the channel (slot), and the channel is a confined space which can contain pressure to some extent. Fluid can be thermally insulated from the surface if it travels down the length of the evaporator in a “supply tube” or corridor, which is closed on all sides within the feed, until it reaches ports where it is introduced to the channel. This allows for cool liquid to be reintroduced periodically to the channel flow which is always gaining heat as it progresses, and visual observations have shown that this helps to combat boiling in the channel itself. When it occurs, boiling within the channel generates vapor pressure which can force fluid out onto the surface, significantly interrupting the flow of fluid along the remainder of the channel length. It may be valuable that the channel itself is a semi-confined space, as it seems to act to retard boiling somewhat compared with fluid on the adjacent open surface. It may be that the channel acts as a pressure vessel, requiring P_{sat} to increase as boiling commences; however, this has not been confirmed. It is important to note that in both final designs, feed tubes performed sufficiently well in order to be deployed for ammonia testing; however, there is much to be gained from a more careful analysis and optimization of the feed tubes. A future study may consider investigating the variables outlined in Table 18.

Table 18: Variables to analyze in a later channel feed optimization study.

1. Channel width
2. Channel depth
3. Port count
4. Port spacing
5. Port diameter
6. Effects of varying port spacing/diameter with respect to length
7. Supply tube wall thickness
8. Supply tube diameter
9. Advantages of open ended vs. closed ended supply tube
10. Varying channel depth/width as a function of length
11. Length of the feed tube in which the supply tube diameter is bored (if otherwise solid)

As a note, channel feed tubes were tested which had small notches cut into the sides of the channel in order to let excess fluid run out of the channel and down along the length of the tube (as in the liquid guide model). This is generally advised against as the advantages of the channel feed were somewhat trumped, and a successful tube was not developed.

LMTD:

LMTD is an important variable in the design of an LGTE suitable evaporator. Very low LMTD applications may require evaporators which function will under single phase conditions and will require higher overall U values to produce. Higher LMTD applications may require evaporators which can make use of boiling heat transfer and withstand higher heat flux before dry out. Performance as a function of LMTD can vary with several conditions. In this study, the capillary feed mechanism performance is of most interest; so, here we will look at how the same evaporator tube performs under identical conditions except with changing fluid distribution and feed delivery mechanism. The following discussion focuses on the 3/4" half-length ISTF tube.

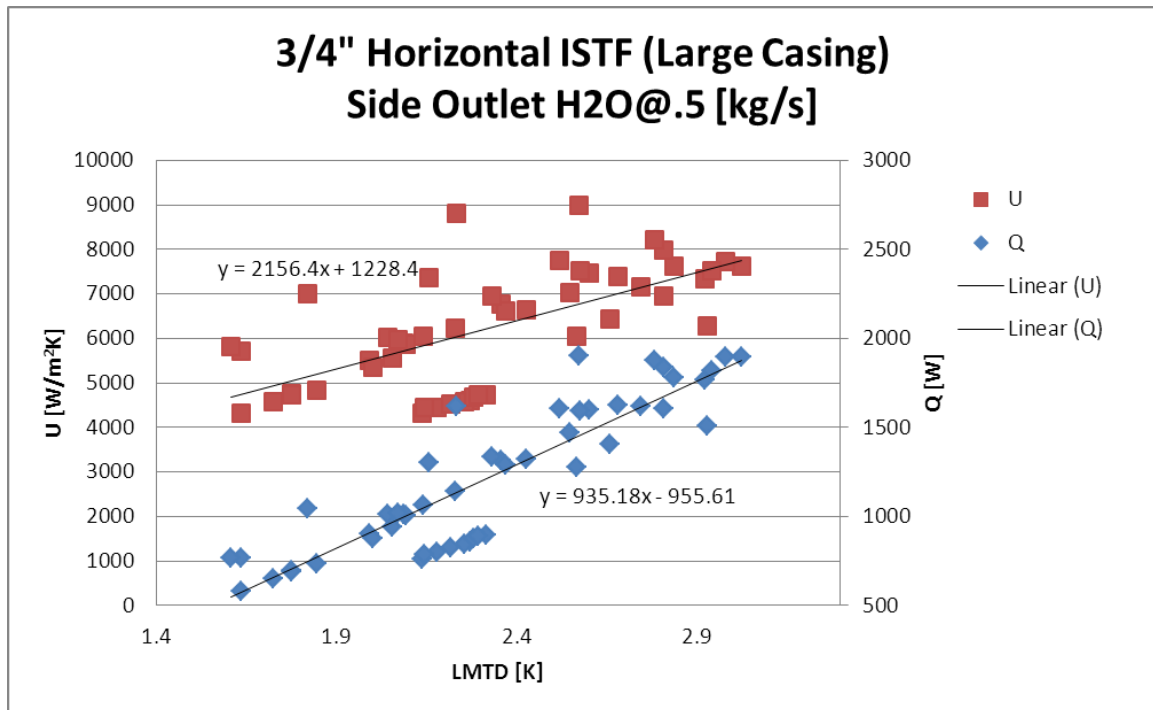


Figure 68: 3/4" half-length horizontal ISTF large casing performance with change in LMTD.

Figure 68 shows the half-length tube tested in the horizontal orientation with the large test casing. This configuration shows an increase in overall heat transfer performance as LMTD increases. On the contrary, Figure 69 shows how this same tube performs better at lower LMTD, in the smaller test casing, and may even exhibit a slight decrease in performance as LMTD increases. The exact cause of this difference is not confirmed; however, it seems likely that it is due to flow distribution within the casing and the consequent ability of the surfaces to stay wetted at higher heat fluxes. Remember, in the small test casing the vapor flow gap is small and symmetric; in the large casing, the vapor flow area is asymmetric and much larger in some areas. In both of these horizontal pool fed examples, the water side is held constant; so, changes in U value are largely a consequence of refrigerant side performance. As expected, in both cases, heat flux is increasing with LMTD;

although, heat flux increases faster in the large casing due to the improving refrigerant side capability.

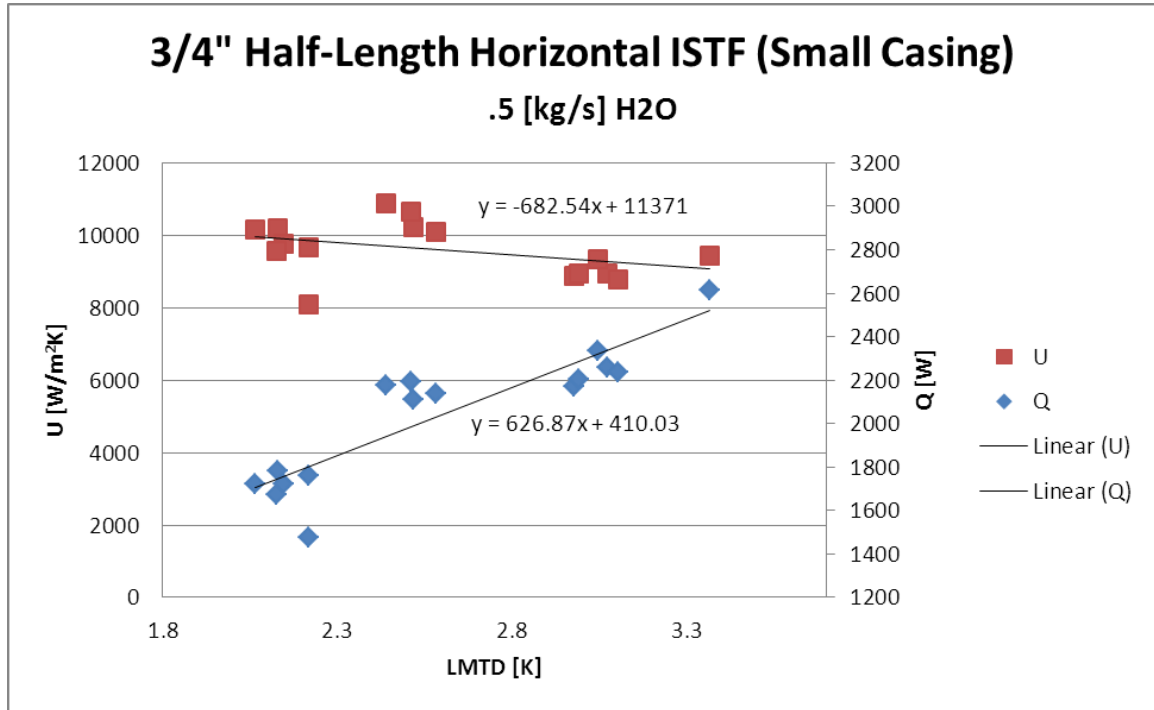


Figure 69: 3/4" half-length horizontal ISTF small casing performance with change in LMTD.

Figure 70 shows performance for the vertical half-length orientation, which uses the large test case and slot feed. Performance in this test is slightly lower than the horizontal small test casing, but much better than the horizontal large case. This is likely due to differences in the way that the vertical tube removes excess liquid when compared with the horizontal tubes. Later discussions demonstrate that increasing refrigerant delivery to the vertical tube does not correspond to proportional increases in the flooding of the vertical evaporator surface as the channel feed is designed to drain away excess delivery fluid. Notice that the slope of the linear curve fit for the overall heat transfer coefficient in Figure 70 is rather moderate compared to the large casing test (nearly half). This comparison between the horizontal and vertical large case ISTF tests give a direct comparison of the performance of the pool feed and capillary slot feed mechanisms as heat flux changes.

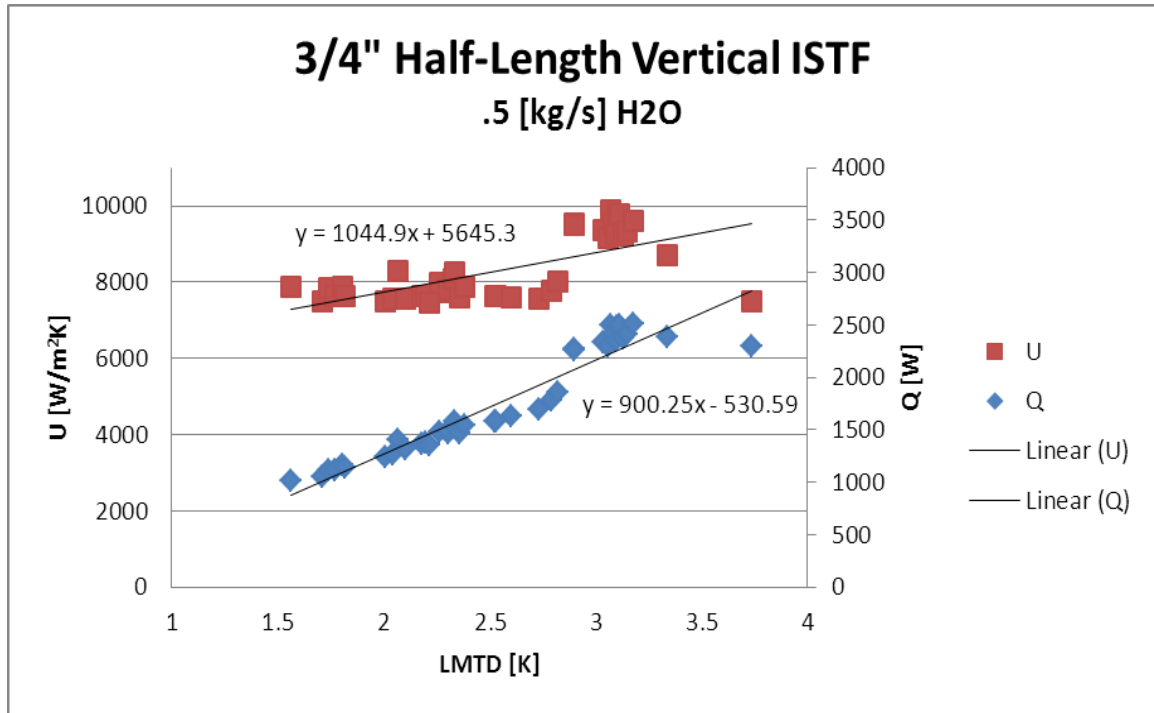


Figure 70: 3/4" half-length vertical tube performance with change in LMTD.

Refrigerant Flow Rate:

Refrigerant flow rate is an important factor in tube performance. A tube that is under-fed fluid is prone to dry out, and a tube that is over fed experiences flooding in the capillary fed configuration. Most of the tested surfaces show data at or near optimum refrigerant flow rate. The optimum refrigerant flow rate in the capillary fed regime is the flow rate which most closely satisfies the evaporating mass flux at a given test condition. The expected evaporating mass flux can be approximated by using the following energy balance equation under saturated fluid conditions.

$$\dot{m}_{evaporating} = \frac{Q}{h_{fg_{NH3}}}$$

The latent heat of evaporation for ammonia was approximately 1.2 [kJ/g] for most test conditions. According to the energy balance equation above, we would expect the surface to be optimally fed at about .73 [g/s] when 875 [W] of heat is evaporating. This projection is in very close agreement with the plain fin result shown in Figure 71. Another method of predicting optimal surface feed rate is by measuring bi-pass fluid, or liquid which leaves the separator during testing and was not evaporated. When the delivery flow rate exceeds the evaporating flow rate, the bypass fluid can be measured and is plotted against performance in Figure 72.

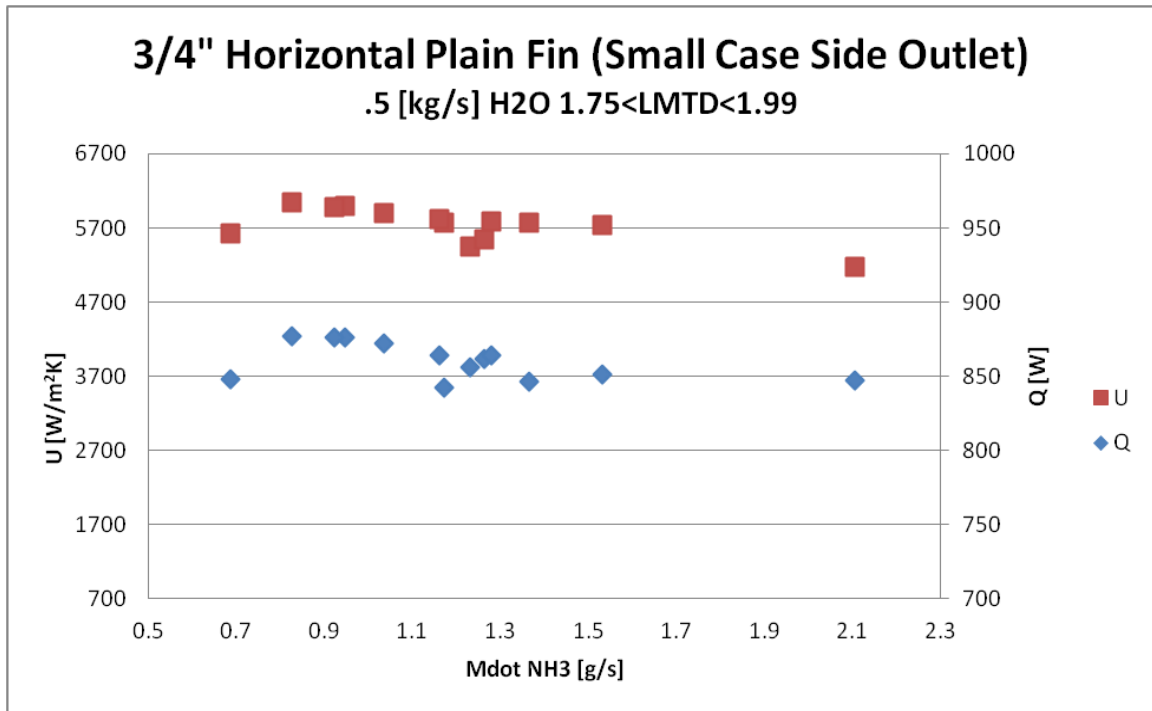


Figure 71: Variation of U as surface-overfeed changes (energy balance method).

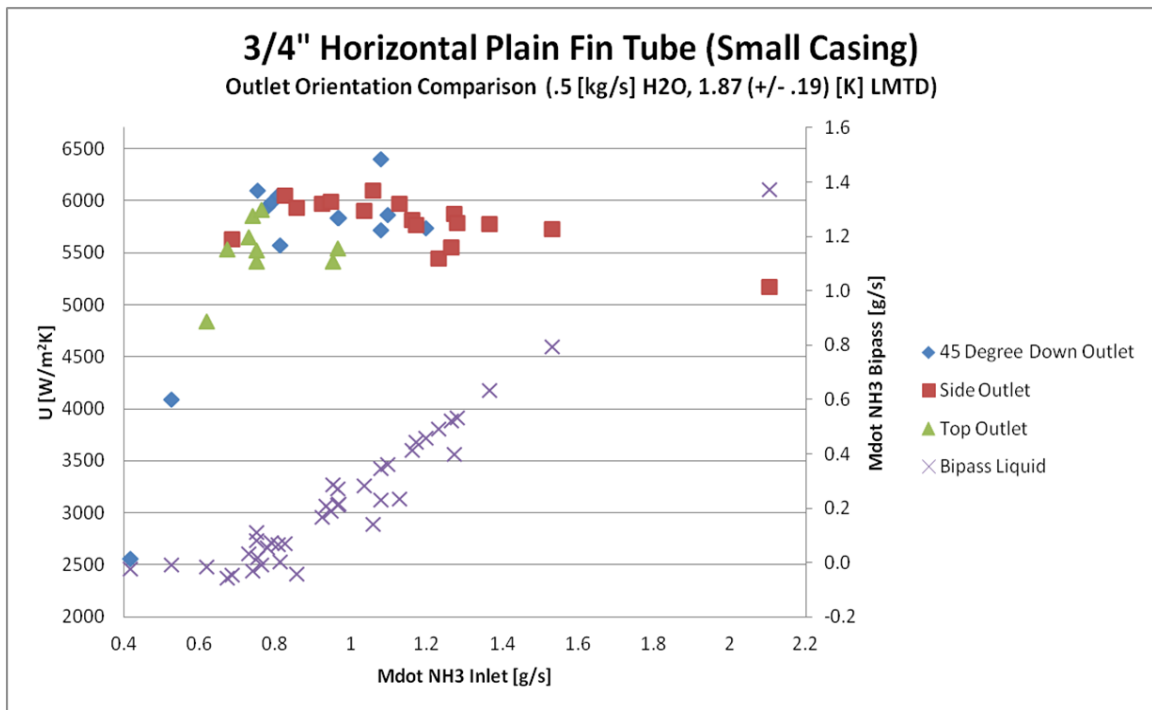


Figure 72: Variation of U as surface-overfeed changes (bypass fluid method).

Here it is clear that some initial flow rate is required to wet the surface. This flow rate is lower for the 45 degree downward orientation, possibly because when the outlet is facing down some fluid is able to drain before the liquid reaches the surface

of the evaporator. As delivery flow rate increases, the surface begins to wet and performance increases. At the optimum point, additional delivery results in increasing surface overfeeding and performance begins to taper off.

There is an inherent difference in how the horizontal and vertical feed mechanisms handle excess fluid; resultantly, there is a difference in how easily a surface can be flooded by excessive refrigerant delivery. In the horizontal feed configuration, increasing the flow rate beyond the required evaporating mass demand tends to have an immediate impact on surface flooding. This impact is less pronounced for the outlet orientation which is better able to quickly remove excess fluid, but careful observation of Figure 72 above confirms a decrease in performance as excess fluid enters the casing. This effect is not nearly as pronounced in the vertical feed.

In the vertical feed, when excess fluid is delivered to feed tube, it tends to continue down the length of the channel slot and exits the feed tube without much impact on evaporator surface wetting. In this design, the surface “takes what it needs” and excess fluid is free to continue out of the test section unused. Visual assessments during ethanol testing has shown that there is a limit to this capacity – likely when the flow rate is so high that pressure drop within the channel slot exceeds pressure drop through the microchannels on the surface – and flooding of the surface has been observed at especially high flow rates. However, it is not always true, as it usually is in the horizontal feed, that increasing the flow rate beyond the optimum floods the evaporator surface. The difference between the horizontal and vertical feeds is apparent in Figure 73 where overall heat transfer coefficient is shown relative to the percent of overfeed that the surface experiences (0% equates to equal mass balance between delivery liquid and evaporating ammonia). In this figure, a pronounced downward trend is apparent in the horizontal feed, as over-feed increases. The scatter of the data may also be some indication of sporadic or uneven flow distribution in the over-fed horizontal context.

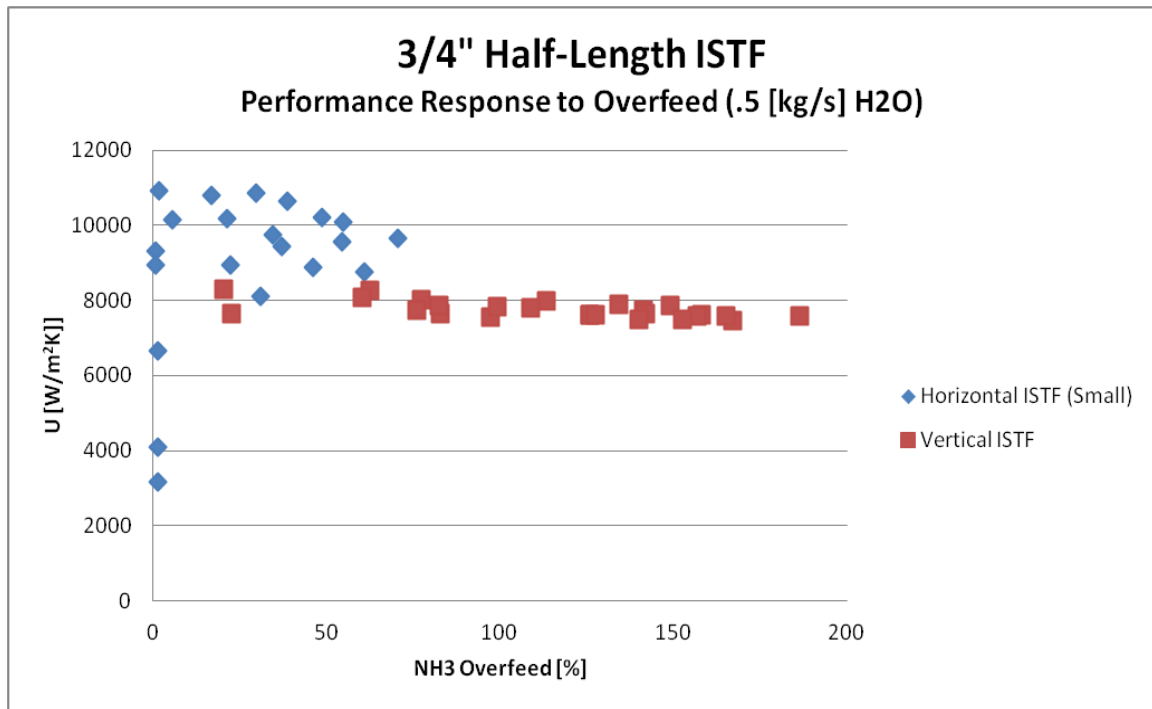


Figure 73: Overall heat transfer coefficient vs. overfeed for both horizontal and vertical configurations.

Here, it is warranted to provide a bit of explanation about why flooding the surface can be detrimental to the performance of the capillary fed surface. In falling film configurations, dry out is also experienced when the surface is under fed and refrigerant supply cannot meet the evaporating energy demand, a function of heat flux and delivery flow rate, as is shown in Figure 74. However, in falling film configurations, increases in refrigerant supply beyond the energy balance point results in either stable or improving performance. This is shown in Figure 75. This is in contrast to the capillary fed concept. The explanation lies in the difference in how the two feed mechanisms work.

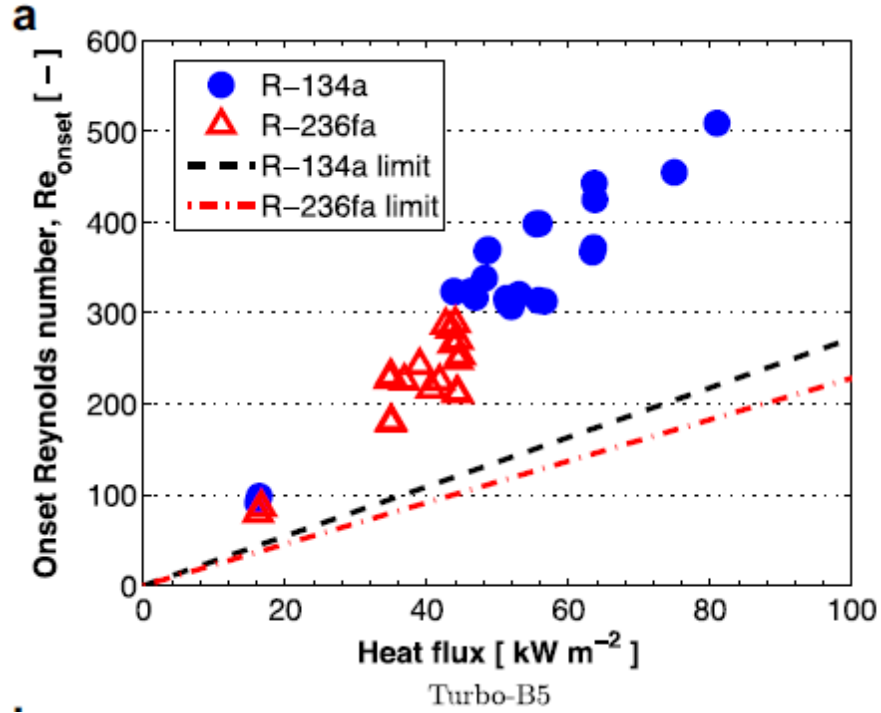


Figure 74: Onset of dry out in a falling film tubular bundle [24].

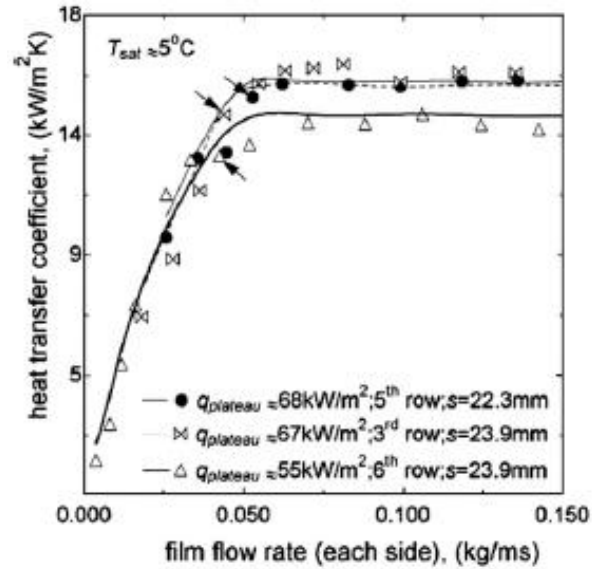


Figure 75: Falling film performance as surface overfeed increases [29].

In the forced fed example, flow boiling best describes the two phase regime. Bubbles form as the refrigerant begins to boil, and they are carried away from the surface to be replaced by cooler fluid. This is illustrated in Figure 76.

Falling film flow direction
(into page)

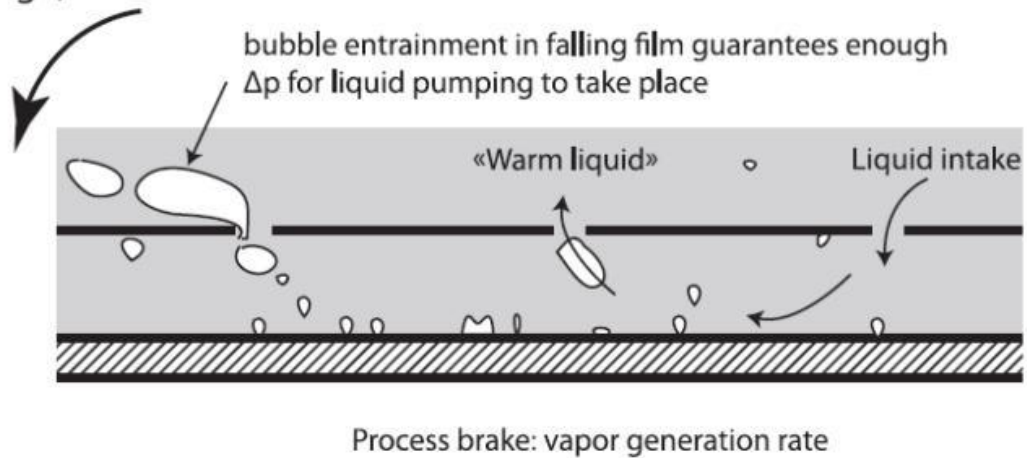


Figure 76: Two phase flow in an enhanced surface using falling film [30].

Increasing the refrigerant flow rate in falling film configurations increases convective heat transfer, improves thermal mixing, more efficiently removes bubbles from confined surface features, and increases the heat flux capacity of the evaporator before experiencing dry out. With the capillary feed in the horizontal orientation, there is no gravity assist, so increasing flow rate only eliminates the microstructure surface's ability to induce meniscus enhanced thin film evaporation. In the vertical orientation, there is likely some flow boiling effect; however, the direction of film is perpendicular to the microchannel and visual studies using ethanol have confirmed that this film remains confined to small regions of the surface only. Finally, although surface flooding may help to combat dry out, it is unlikely that the surface is flooded enough to imitate the mechanisms apparent in pool boiling.

Pool boiling differs from the capillary feed in that thin film evaporation is only available for short periods at points where bubbles contact microstructure walls, and increasing heat flux improves the performance of an immersed tube [26]. Increasing heat flux improves the function of a pool boiling tube in that increased boiling develops a more pronounced local surface velocity due to bubble buoyancy. This effect, coupled with the large availability of sub-cooled fluid surrounding the tube, makes pool boiling a more attractive option for higher heat flux applications so long as the critical heat flux of the working fluid is not approached. In contrast to pool boiling, an over-supplied capillary fed surface does not have access to large quantities of sub-cooled liquid and cannot easily induce high Reynolds number surface flows due to bubble buoyancy.

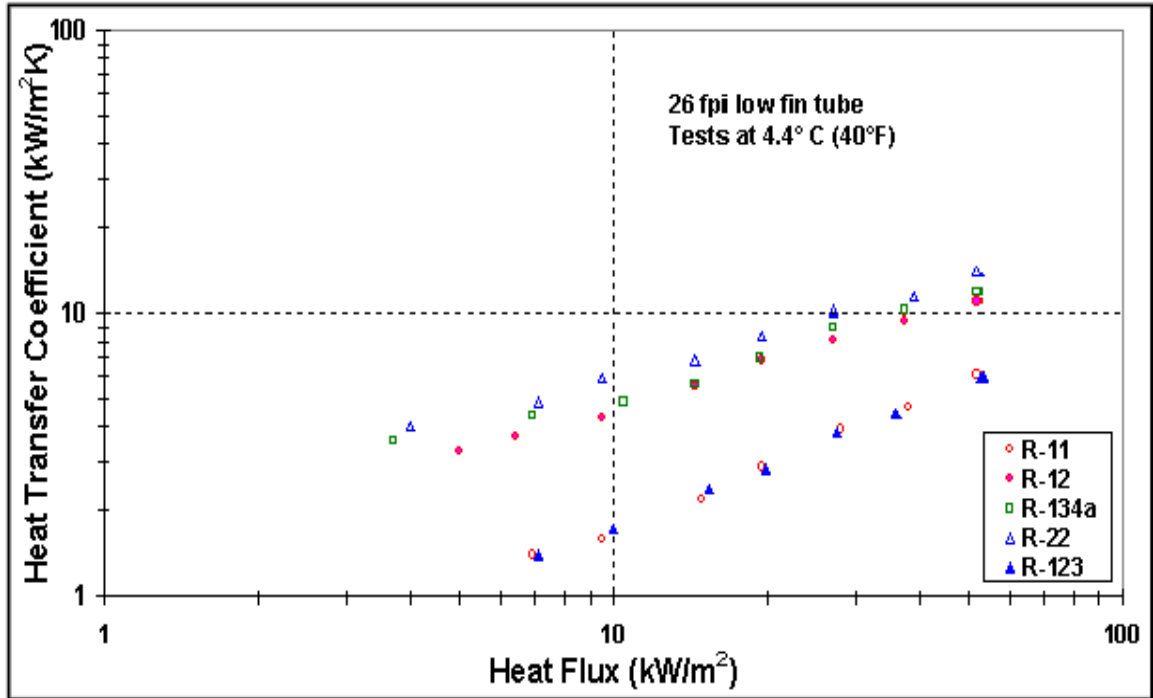


Figure 77: Pool boiling heat transfer as heat flux increases (Webb & Pais 1992) [24].

These comparisons help to provide the framework for understanding the fluid regime of the capillary fed surface. Performance for all of the configurations tested using the ammonia independent loop are shown as a function of delivery flow rate, as LMTD is held constant, in Figure 78. From this chart it is easy to see where the various surfaces are optimally fed and how flooding affects the performance of an individual configuration.

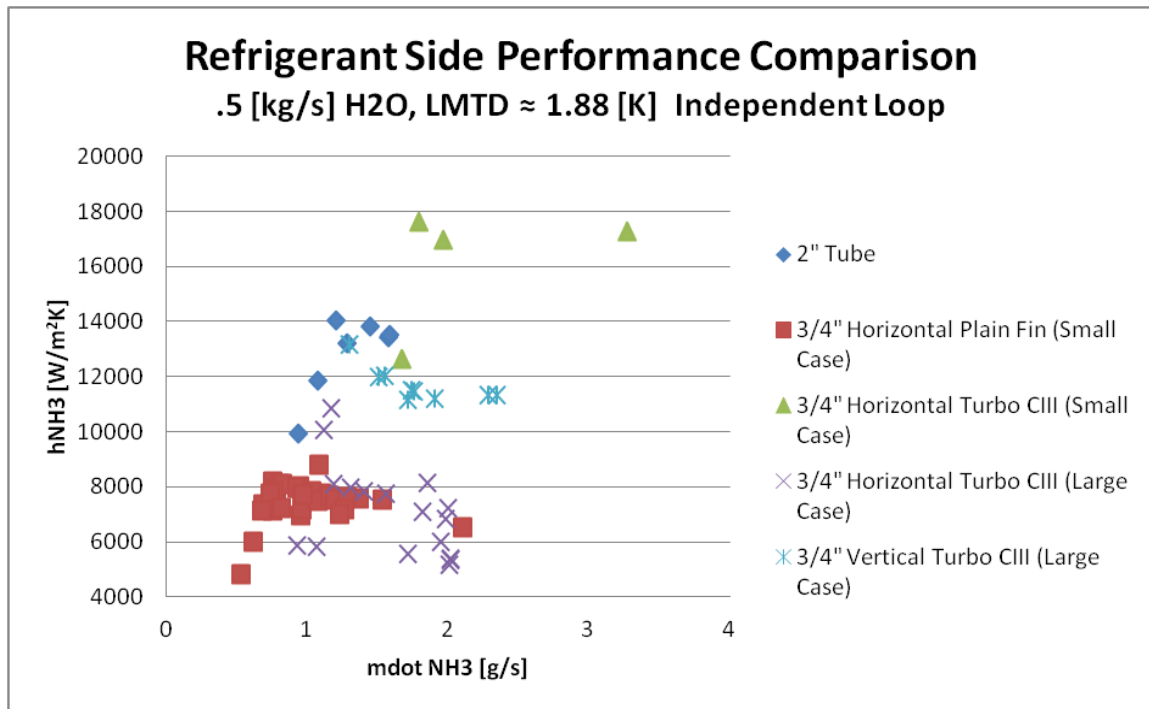


Figure 78: NH₃ side performance comparison as delivery rate changes for all tubes.

Refrigerant Flow Distribution:

All tests conducted in this study have shown a strong relationship between tube performance and refrigerant flow distribution. Whether it is due to flooding or dry out caused by an inadequate feed tube design or delivery flow rate, or test casing considerations (small versus large casing vapor flow path), it is evident that optimum and adequate feeding of the evaporator surface is important to performance. In test casing designs where there is a very small gap between the evaporator and test casing, it takes a very small volume of excess fluid to completely flood the test section. This sensitivity can cause a surface to flood rapidly with only minor fluctuations in delivery flow rate, heat flux, or poor control of test instrumentation and equipment. It is suggested that future research heeds this consideration valuable, and the employment of larger test casings and careful feed tube design should be investigated.

Water Flow Rate:

Water flow rate had a large effect on tube performance. In all tests, surfaces were refrigerant side limited, as is apparent in Figure 79 which shows results for the .5 [kg/s] flow rate. Notice that only in the small horizontal ISTF configuration (best performer) does the refrigerant side begin to approach water side performance levels. Increasing the water side flow rate resulted in a marked improvement in overall heat transfer and heat transfer coefficient for all cases. Figure 80 and Figure 81 demonstrate the effect of increasing water flow rate for the 2" and 3/4" plain fin tubes. In all cases, LMTD was held near constant around 2 [K].

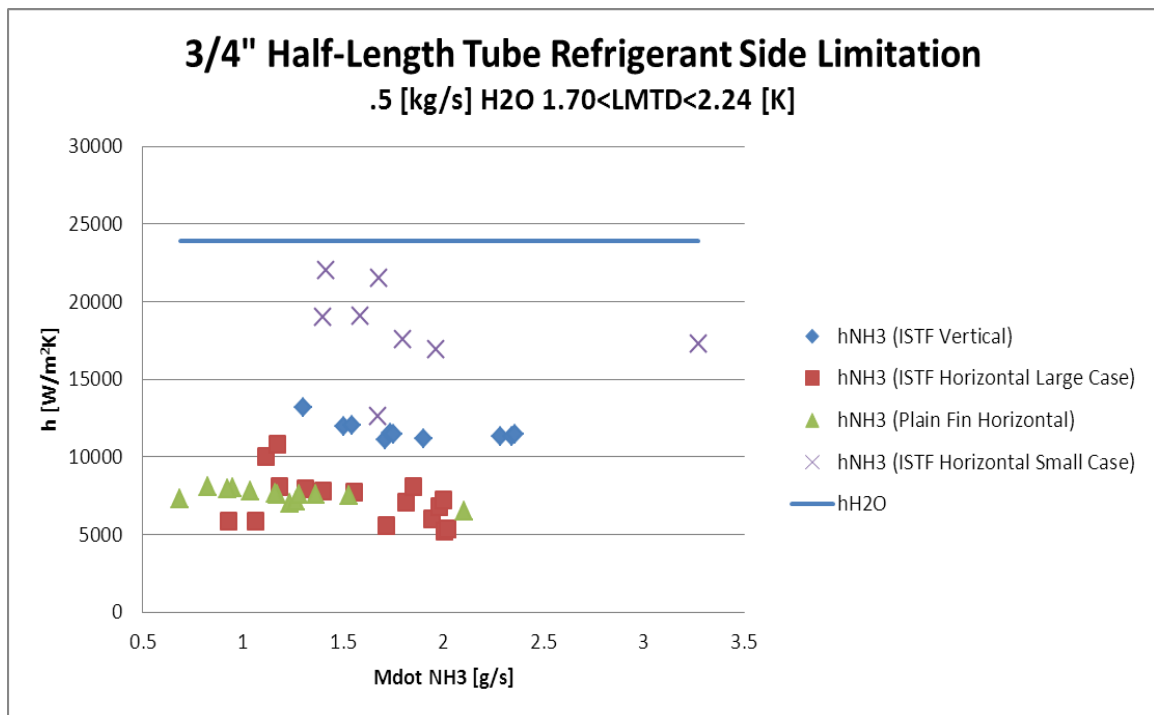


Figure 79: 3/4" half-length tube refrigerant side vs. water side performance (.5 [kg/s] H₂O).

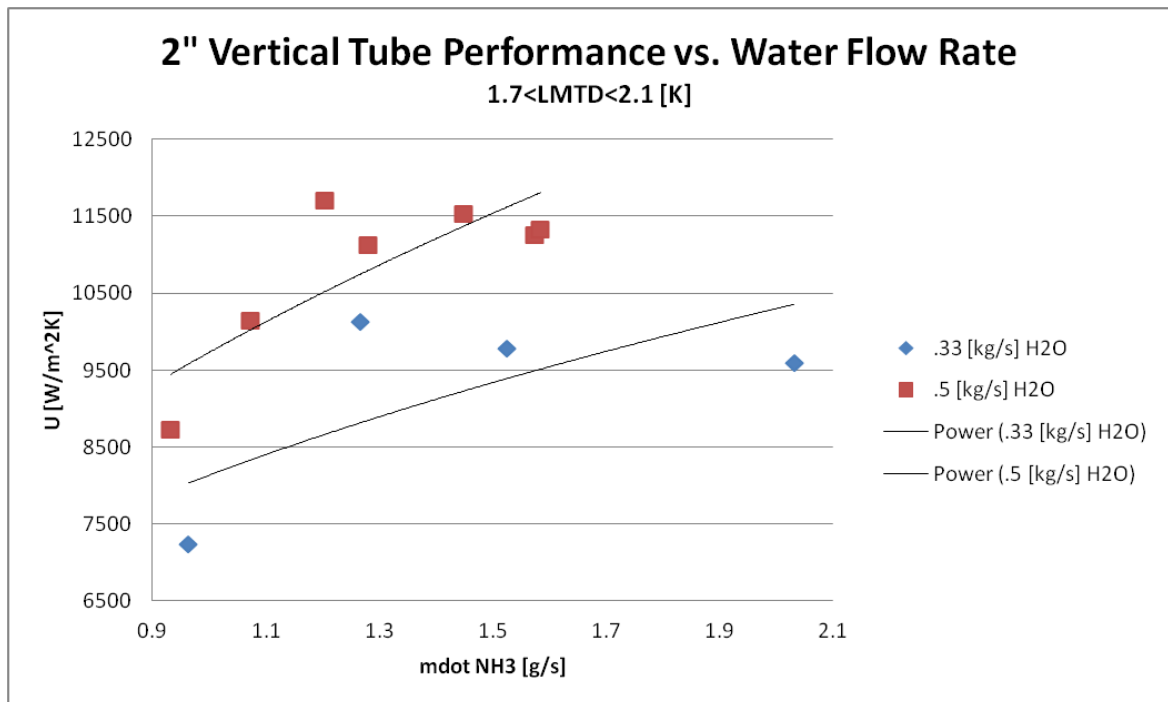


Figure 80: 2" Vertical tube U vs. water flow rate.

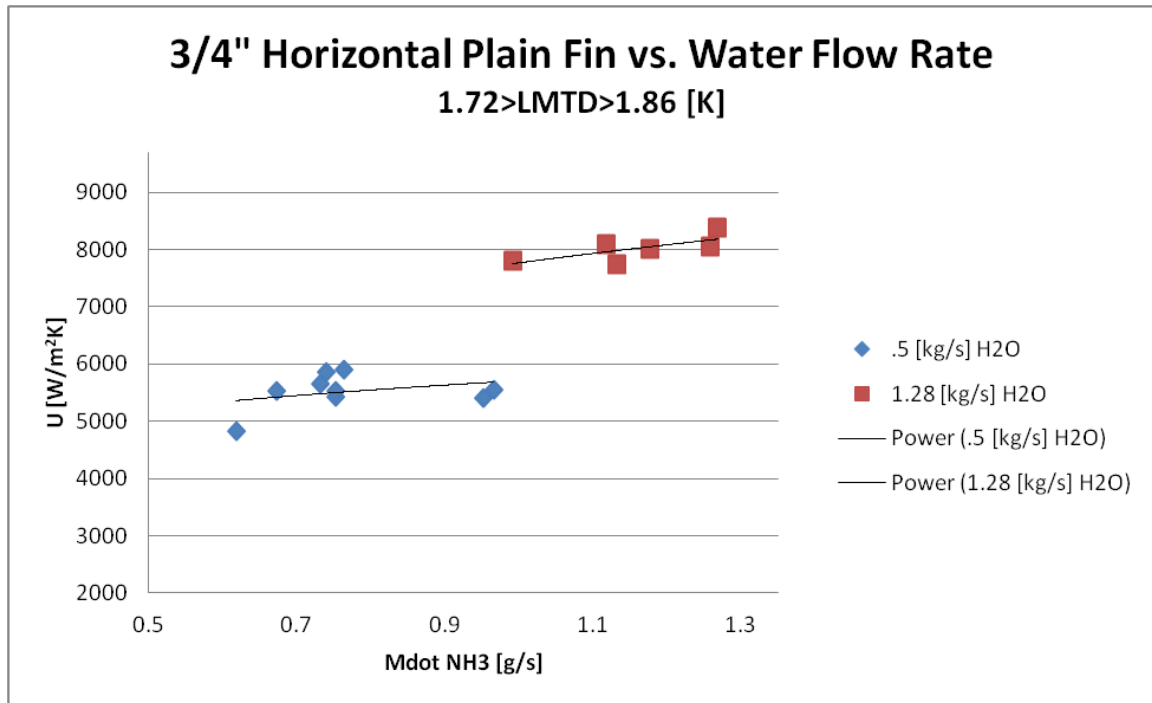


Figure 81: 3/4" horizontal plain fin tube U vs. water flow rate.

Increases in LMTD or heat flux did not seem to result in a marked impact on refrigerant side performance for the horizontal ISTF tube in the small test casing. This is apparent in Figure 69 as well as Figure 83. Increasing the water side flow rate, improves the water side heat transfer coefficient and results in an increase in the overall heat transfer and heat transfer coefficient of the tube, as is apparent in Figure 82. Reviewing the three figures mentioned here for the horizontal ISTF small case tests, shows that the improvement in performance is solely due to the water side.

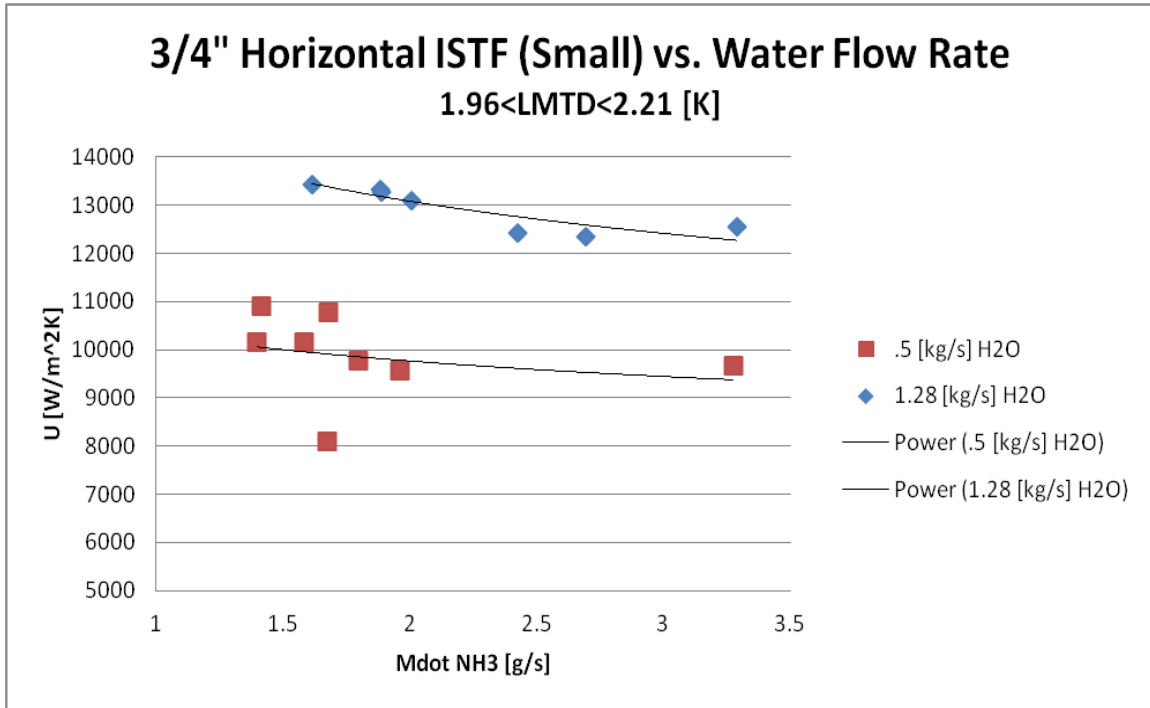


Figure 82: 3/4" horizontal ISTF (small) tube U vs. water flow rate.

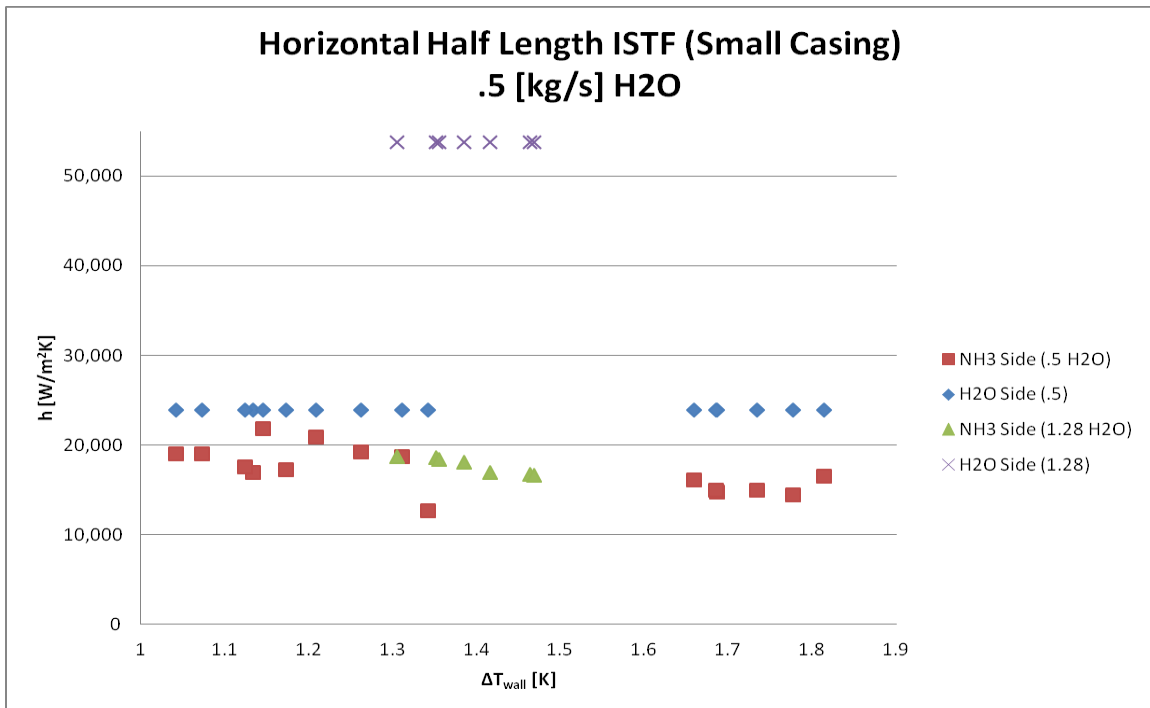


Figure 83: 3/4" horizontal ISTF (small) contribution to U vs. water flow rate.

Correlational Heat Transfer Mode Characterization

As the capillary feed mechanism was the novel concept proposed in this research, it is of primary importance in our discussions. To complement the above analysis, a few correlations are applied to results from the current work in order to better understand the nature of the capillary feed performance. The focus here is solely on the refrigerant side, with an emphasis on perspectives which may shed light on how well the surface was performing during operation in the independent ammonia test loop.

As mentioned in several instances in the preceding sections, feed mechanisms were initially developed using ethanol which were capable of delivering working fluid to the enhanced surface in the event that nucleate boiling commenced. This was mostly done as a precaution to ensure against catastrophic failure of the delivery mechanisms in the event of momentary instances of nucleate boiling. The enhanced surfaces are not likely to perform well in the capillary fed configuration during boiling. This is due to the likelihood that microchannels are obstructed by forming bubbles, which prevents capillary feed to the downstream portions of the channel. This is illustrated in Figure 84 below. It was confirmed from visual observation during feed development that boiling caused significant dry out in capillary channels. This dry out occurs at varying distances from the feed mechanism as heat flux and refrigerant flow rate changes.

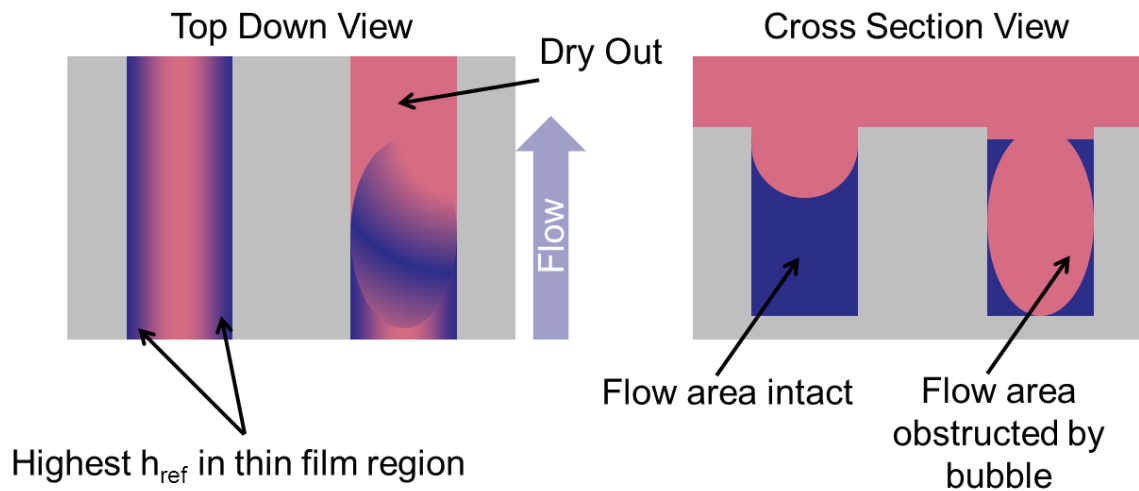


Figure 84: Illustration of channel dry out caused by bubble nucleation.

Correlations were applied to a representative data set from the horizontal ISTF small casing test in order to assess the likelihood that boiling was occurring on the surface during tests using the independent ammonia loop. It can be confirmed from multiple predictions that boiling was almost certainly present, as is shown in Figure 85. The correlations selected include a study which intentionally focused on onset of nucleate boiling in microchannels [38] and a couple of other well established correlations. Details about each of these correlations, including step by step

derivations, are given in the appendix. As a validation, the same correlations were also used to predict the onset of boiling for water in an independent study [44], and predictions correlated well with results as shown in Figure 86. These results, in conjunction with visual observations of surface wetting during boiling, provide evidence that the surfaces were underperforming in this study and additional tests may provide better results.

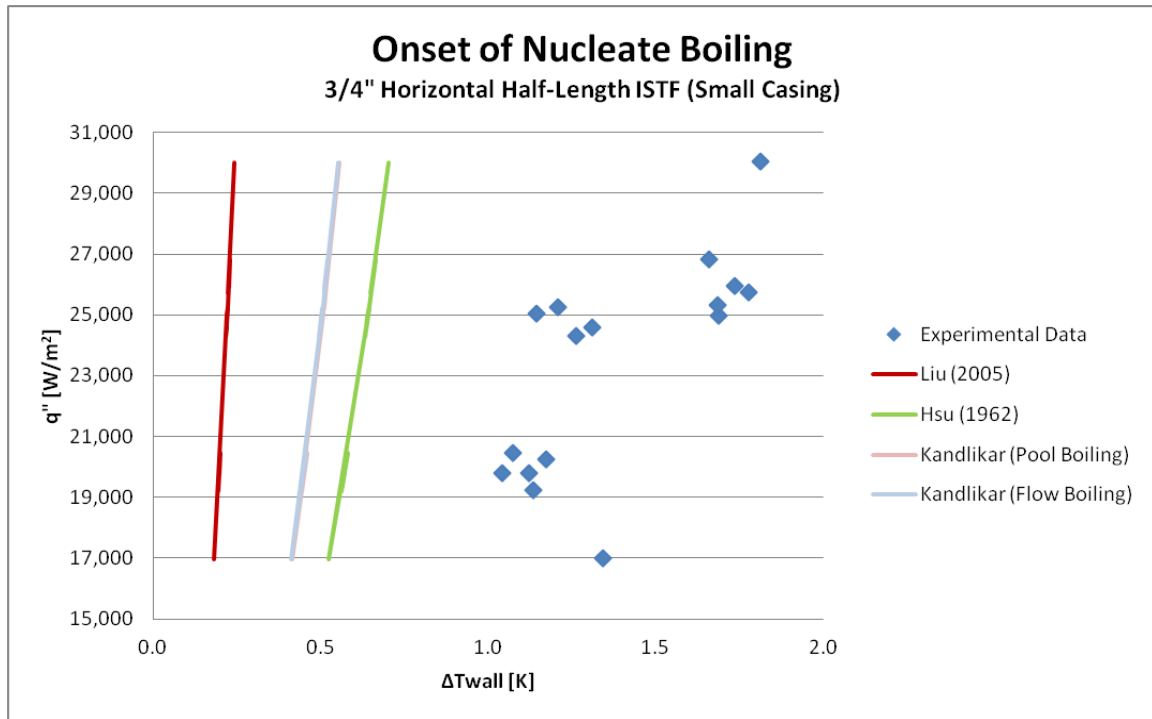


Figure 85: Onset of nucleate boiling prediction.

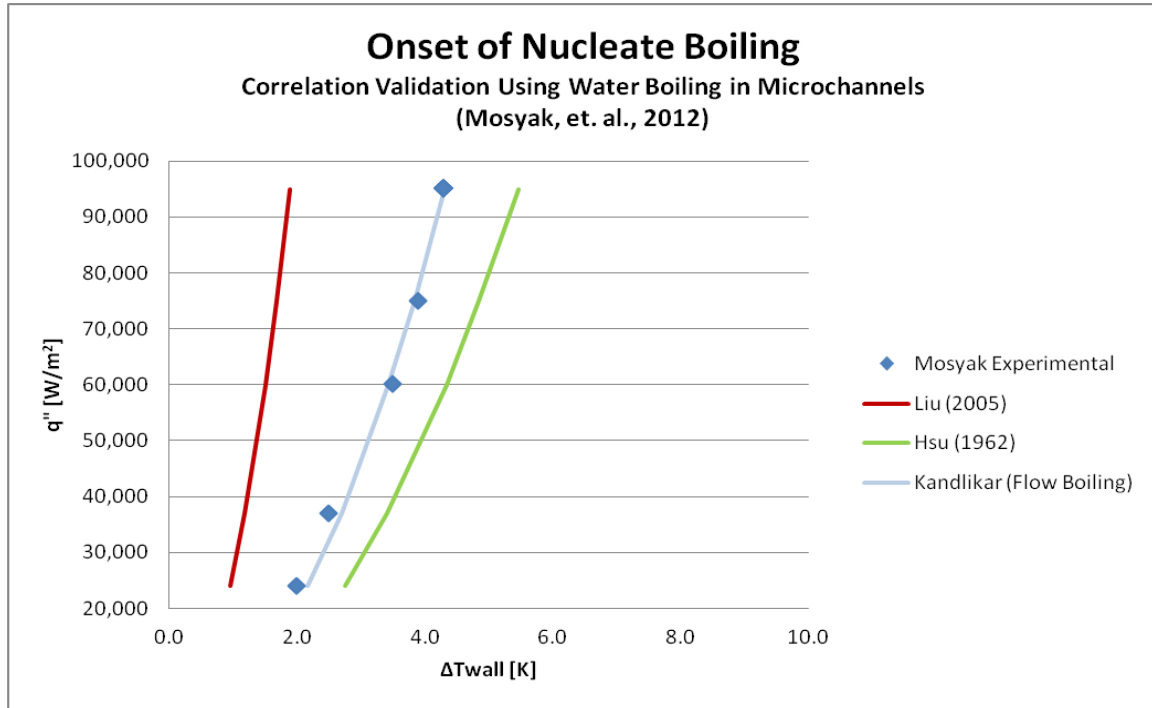


Figure 86: Onset of nucleate boiling prediction validation.

As a precaution, data was also compared with two critical heat flux correlational predictions. This is shown in Figure 87. As suspected, surfaces were operating well below the critical heat flux threshold. Details of these two correlations are also provided, along with derivations, in the appendix.

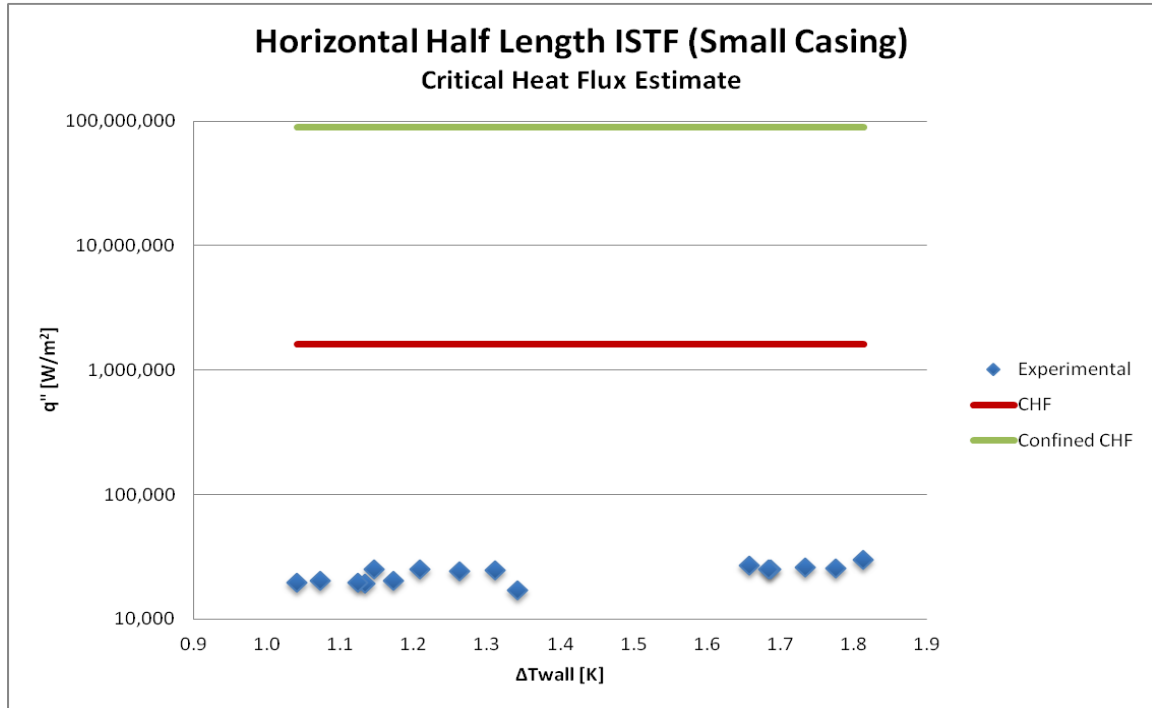


Figure 87: Critical heat flux assessment.

In addition to boiling, it is of interest to approximate the dominant mechanism of heat transfer in the channels. By plotting correlations for pool boiling, flow boiling, and thin film evaporation in the specific geometry and operating conditions of a given, we may gain some insight into the level of surface flooding and average relative performance being produced. Below, established correlations are plotted against actual test data. Details about the correlations and derivations are given in the appendix. Figure 88 applies to the horizontal half-length ISTF tube in the small test casing, and Figure 89 the horizontal plain fin tube.

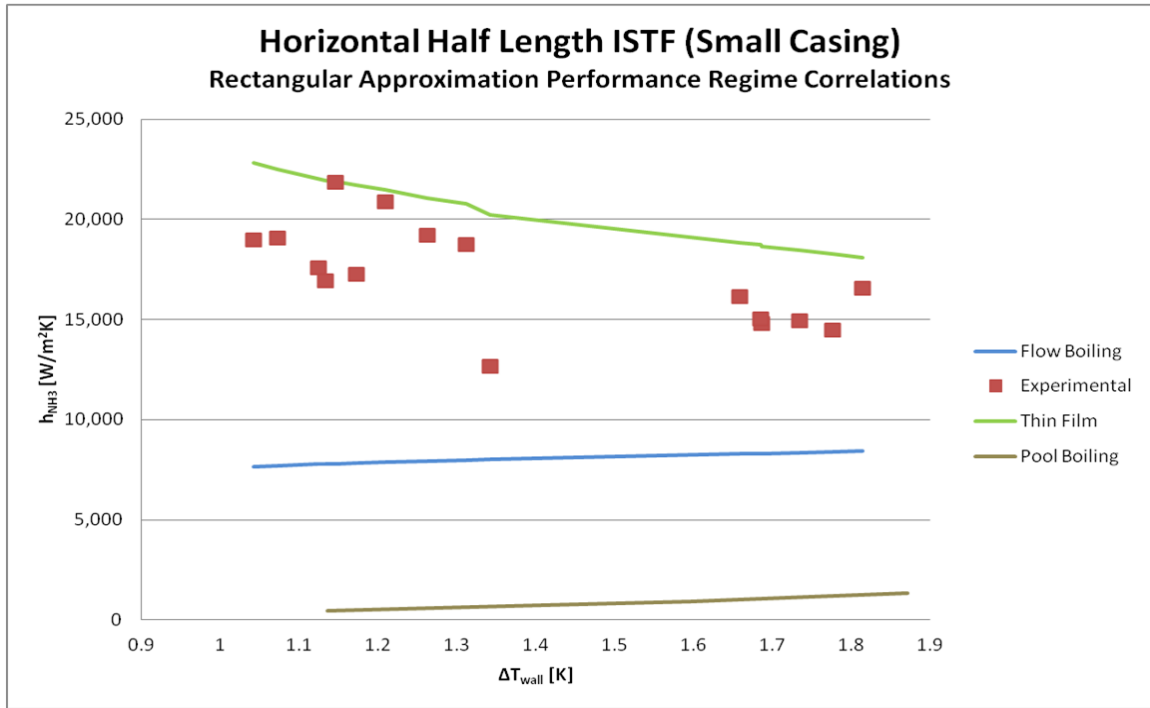


Figure 88: Heat transfer regime analysis for horizontal ISTF small casing.

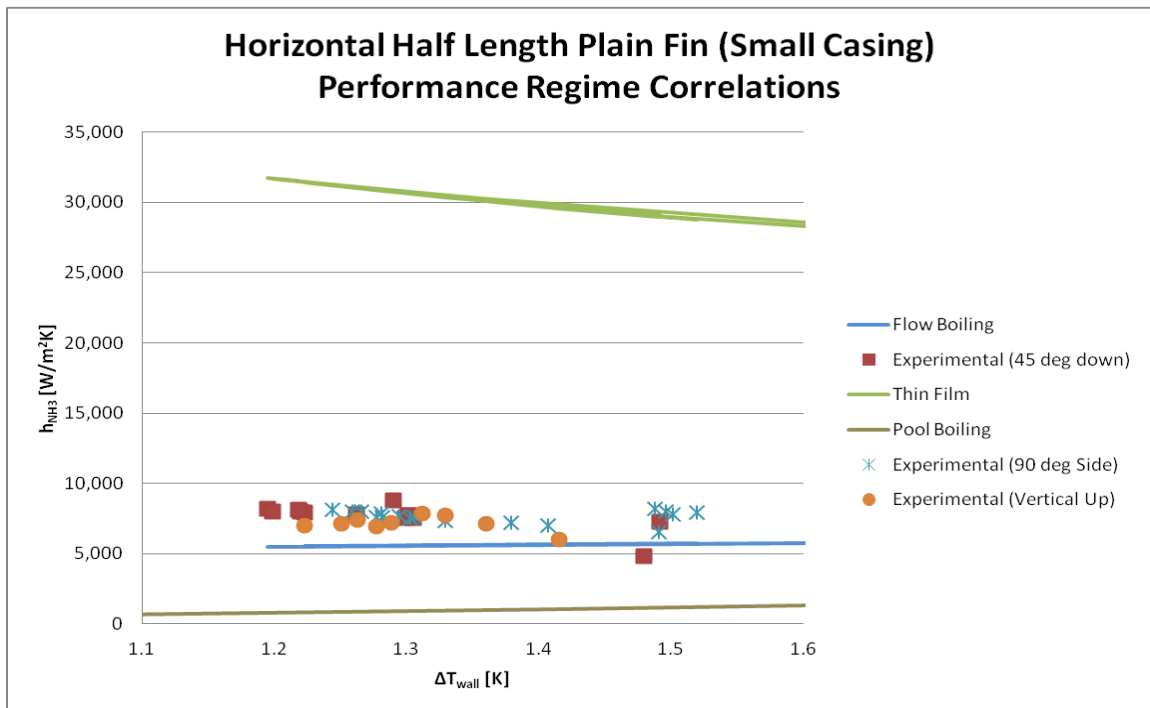


Figure 89: Heat transfer regime analysis for horizontal plain fin.

This analysis provides some evidence that the thin film evaporation dominated regime, which the capillary feed was envisioned for, has not been fully realized. In both cases, results correlate fairly well with flow boiling predictions, which indicates

that the surface is boiling or that areas of dry out are resulting in a reduced average performance. It is important to note that in the ISTF chart, thin film correlation is likely strongly under-predicted. This is because a rectangular fin approximation has been used to simplify the very complex geometry of the surface. This approximation neglects a significant portion of surface feature which would lie near the point of the meniscus – wall interface, and result in a higher heat transfer coefficient. It is unlikely though that the thin film prediction for the ISTF tube would, if better approximated, produce results as relatively high as in the plain fin tube. This is because plain fin channel density is higher than the ISTF and the increased number of thin film profiles results in a higher surface flux.

A brief description of some important assumptions made for these correlations is warranted. In the case of flow boiling, an optimum feed condition was approximated. Here, it was assumed that all mass entering the channel travelled 180° around the circumference of the tube where it met fluid coming from the other side. Channel inlet velocity was approximated by conservation of mass and channel cross section. This results in a constant channel velocity; in reality, fluid velocity would decrease from the inlet to the point where all mass had evaporated. In the case of thin film, the assumption is that the channels are all wetted properly, and that a meniscus had formed and not been disturbed by boiling. It also assumes that the meniscus is intact and unchanged throughout the channel length.

In sum, actual performance is likely the result of an average of several conditions occurring at any given time. Regions of dry-out, boiling, thin film evaporation, and flooding are all possible. The final measured values, which are based on global measurements, are the result of all of these conditions combined. The preceding analysis, therefore, should not be strictly interpreted; but, does likely serve as a useful guide as to how well the surface is performing and where improvements could be made.

Chapter 6: Conclusion

LGTE resources are seeing increased interest in recent years, but the inherently small overall thermal gradient between the heat source and sink poses specific challenges for technologies which seek to economically harness the available energy. Most LGTE technologies utilize a closed organic Rankine cycle (ORC); for these applications, the heat exchangers have been identified as the component in the cycle where the most impact can be made toward realizing maximum efficiency [3, 12, 15]. Both flat-plate and tubular evaporators could be considered for this application, but tubular evaporators provide a more leak resistant geometry with good fluid distribution capability. Accordingly, a tubular evaporator is desired with a high overall heat transfer coefficient, good performance at low heat flux and low wall superheat, practical bundling capability, and minimal pumping power requirements. In this research, a novel capillary-fed enhanced tubular evaporator was employed which was deemed suitable for LGTE applications.

In literature, there are several existing feed mechanisms available for use in the LGTE ORC for administering working fluid to an enhanced evaporator surface. Falling film, pool boiling, and forced-fed manifold configurations have shown refrigerant side heat transfer coefficients above 100 [kW/m²K] in certain cases (see Figure 5 and Figure 6); however, most results are more modest – at least half – and usually vary significantly with test conditions. In general, test conditions with significant impact on evaporator feed administration include refrigerant selection (see Figure 9), surface enhancement selection (see Figure 12), saturation temperature (see Figure 10), heat flux (see Figure 7), refrigerant flow rate (see Figure 6), and feed mechanism (see Figure 11). It is important to note the fundamental differences between the capillary feed mechanism utilized in this research, and the existing feed options just described.

These existing feed configurations work by providing either a vast or moving layer of liquid working fluid to the surface of the evaporator. This results in a configuration which is capable of handling high heat flux and high wall superheat (see Figure 76 and Figure 77) due to the utilization of nucleate boiling heat transfer. It is usually true that in these configurations increased heat flux or wall superheat results in a higher refrigerant side heat transfer coefficient (see Figure 8), until the onset of surface dry-out or the critical point of the working fluid is approached (see Figure 7). The high refrigerant side heat transfer coefficients reported with these existing delivery mechanisms are attractive; however, bundle considerations and required refrigerant side flow rates should be addressed when considering LGTE applications, and are discussed shortly.

The capillary feed mechanism functions in a fundamentally different way than falling film, pool boiling, or forced-fed manifold tubular evaporators. In the capillary feed mechanism, fluid is delivered to an isolated zone on the enhanced surface, and capillary action provides the pumping pressure required to distribute working fluid over the remainder of the evaporator. Surface enhancement features induce liquid

meniscus formation, and thin film evaporation dominates the refrigerant side heat transfer [19]. In order to induce thin film evaporation, surface flooding and dry out must be avoided; as a result, capillary forces are relied upon to replace evaporating fluid rather than bubble buoyancy (as in pool boiling) or fluid motion (as in falling film or forced-fed manifold designs). The resulting scenario is one which requires approximately only enough working fluid to replace the evaporating mass, as is evident in the optimum feed rate shown in Figure 72 and mass balance described in the same section. Test results can be compared to findings from literature which shows a 98% reduction in required delivery fluid mass flow rate when compared with falling film technology, and a 96% reduction in refrigerant side pressure drop when compared with forced-fed manifold designs (as discussed in the “Applications for the Capillary Feed Concept” section to follow, and compares required flow rate to reach normal operating conditions for a similar heat flux). The resulting pumping power savings will vary with working fluid and the refrigerant system design, but should be considered when extrapolated to a large scale power plant evaporator bundle.

In addition to the reduced pumping power, the capillary feed can be attractive for LGTE applications because of its reliance on thin film evaporation rather than nucleate boiling. Whereas the existing feed mechanisms previously discussed rely on nucleate boiling, which generally improves refrigerant side heat transfer as heat flux and wall super heat increase, thin film evaporation exhibits the opposite behavior (see Figure 88, Figure 89, and [19]). This is advantageous for many LGTE applications where the minimal exergy potential of the ORC can only afford low heat flux or low wall super heat. In these applications, nucleate boiling based evaporator feeds suffer a reduction in heat transfer performance, whereas the capillary feed improves. Consequently, the capillary fed evaporator should choose a working fluid and enhancement geometry which suppresses the onset of nucleate boiling. Nucleate boiling not only decreases the performance of the capillary fed evaporator relative to other existing options; but, there is evidence that it can also lead to channel dry out due to capillary flow obstruction caused by bubbles (see Figure 84 and related discussion).

Ultimately, the capillary fed concept was developed for this research instead of other existing options. The reasons include lower refrigerant flow rate, benefits of thin film evaporation at low heat flux and low wall super heat, and lower refrigerant pressure drop which were discussed above; additionally, practical limitations related to bundling of evaporator tubes was also a factor. Due to the nature of LGTE, a large number of evaporators are required to produce power for a [MW] scale power plant. Resultantly, tubes must be easy and cheap to manufacture and assemble. This factor eliminated most other existing feed options as practical OTEC plant candidates. Falling film and pool boiling configurations face issues with pressure vessel size. Falling film heat transfer performance is influenced by tube spacing which can require a large pressure vessel; pool boiling requires a relatively large refrigerant charge. The saturation pressure, at the operating conditions for OTEC, is around 10 [bar], so large pressure vessels require very robust structural components. Developing tightly packed bundles both optimizes plant design space and reduces construction and operating costs. Finally, forced-fed manifolds are capable of

producing very high refrigerant side heat transfer coefficients; however, high refrigerant pressure drop, and the need to fabricate and install manifolds for each individual evaporator tube, deemed this option impractical.

In this research, the most valuable test results were generated by the independent ammonia loop. Three evaporator surfaces were used to assess a total of five test configurations. These configurations are shown in Table 17. As the 2" one foot tube was tested as a proof of concept for the capillary feed mechanism, it will be excluded from the following discussion. The major test variables assessed included evaporator orientation, refrigerant feed rate, level of liquid immersion (outlet orientation), test casing, and surface enhancement geometry.

The effect of evaporator orientation is best exemplified in Figure 73 where the $\frac{3}{4}$ " half-length ISTF tube was tested in the large test casing in both horizontal and vertical orientations. In this result, the overfeeding of the surface is examined for both orientations, and notable differences in refrigerant side heat transfer response are evident. First, the pronounced dry-out of the evaporator is clear as over-feed approaches zero. As the working fluid delivery rate increases beyond that which is required to replace evaporating mass, the two orientations respond differently. The horizontal orientation exhibits a decrease in refrigerant side heat transfer, and exhibits a more erratic behavior. The decrease in heat transfer is likely due to flooding of the surface and its deleterious effects on meniscus induced thin film evaporation. The cause of the erratic behavior is not entirely clear; but, may be due to erratic flow patterns in the liquid pool at the bottom of the large casing. The vertical orientation exhibits a smooth and minimal decrease in heat transfer as over-feed increases. The vertical feed tube channel allows excess fluid, not removed by capillary action from the surface, to pass unhindered from the bottom of the test section to the outlet. As a result, increasing the delivery feed rate has a minimal impact on increasing actual surface flooding. In general, refrigerant side heat transfer in the horizontal orientation was higher than in the vertical by about 30%.

Refrigerant feed rate had a pronounced impact on refrigerant side heat transfer for all tests. Most notably, when a surface was under-fed, large portions of the surface dried out and were not utilized. Similarly, flooded portions of the surface experienced reduced heat transfer due to the loss of thin film evaporation. Most surfaces exhibited an optimum, with respect to heat transfer rate, at the point where delivery flow rate was similar to the rate of evaporating mass. A well-defined bell curve which exemplifies this optimum is clearly demonstrated in Figure 72 where the $\frac{3}{4}$ " horizontal half-length plain fin tube results are displayed along with delivery and bi-pass fluid data. Notice that when the surface is under-fed or optimally fed, there is no bi-pass fluid, but as delivery flow rate increases, so does bi-pass fluid flow rate, and consequently flooding. It is also noteworthy that in this graphic, it is clear that outlet orientation in the plain fin tube had little effect on heat transfer performance. Varying the outlet port orientation axially was pursued as a method to control the level of the delivery liquid pool in the test casing. It is clear that either there is not a strong correlational relationship between outlet variation and liquid level, or that flooding has a minimal effect on performance.

The effect of test casing is best demonstrated by comparing Figure 68 and Figure 69. In these results, the $\frac{3}{4}$ " half-length horizontal ISTF tube was tested using the small and large casing. Changes in overall heat transfer coefficient and heat flux are demonstrated between the two casings as LMTD is increased for the same waterside flow rate. As expected, heat flux increased with increasing LMTD in both casings; however, overall heat transfer coefficient did not. In the small test casing, overall heat transfer exhibited a slight decrease as LMTD increased; whereas a strong increasing trend was evident in the large test casing. It is likely that this difference can be explained by assuming different heat transfer modes were present between the two tests. In the large casing, increasing overall heat transfer coefficient with increasing heat flux and LMTD (also wall super heat) indicates a nucleate boiling environment. The trend displayed in the small test casing is reminiscent of thin film evaporation (see Figure 88). It is of interest to note that the small test casing was the better performer in this comparison, with overall heat transfer coefficients up to 2.5 times higher. The effect of test casing should be further evaluated so that the cause of this variation can be taken into account for deployment of the tubular evaporator into a bundled configuration.

Finally, the effect of surface enhancement geometry on heat transfer performance is evident in Figure 78. This graph shows the refrigerant side heat transfer performance of all five test configurations. It is easy to see, by observing the plain fin tube relative to the ISTF, that the plain fin tube underperformed every test conducted with the exception of the horizontal ISTF tube in the large test case which it matched. The comparison between the $\frac{3}{4}$ " horizontal half-length plain fin and $\frac{3}{4}$ " horizontal half-length ISTF tests enables the most direct assessment of the effect of surface enhancement. In this direct comparison, the ISTF tube produced a refrigerant side heat transfer coefficient nearly 2.5 times higher than the plain fin tube under the same test conditions. It is also important to point out that in every test conducted the evaporator was refrigerant side limited, with only the $\frac{3}{4}$ " horizontal half-length ISTF tube approaching balanced heat transfer coefficients (h_{H_2O} was 23,900 [W/m²K] in these tests).

Results from this pilot study show promise, with an overall heat transfer coefficient as high as 10,900 [W/m²K] using the $\frac{3}{4}$ " horizontal half-length ISTF tube the small test casing (h_{H_2O} was 23,900 [W/m²K] and h_{NH_3} was 21,800 [W/m²K]); however, there are many opportunities for improvements and additional research for this novel feed concept. Studies are recommended which investigate various enhancement geometries, feed tube optimization, and test casings and are discussed next.

Chapter 7: Potential Applications and Future Work

Applications for the Capillary Feed Concept

The capillary enhanced tubular evaporator concept is an excellent choice for LGTE applications which require minimal refrigerant pumping power losses. Falling film evaporators often provide higher heat transfer coefficients at comparable heat flux values to those tested in this study; however, required refrigerant flow rates are much higher.

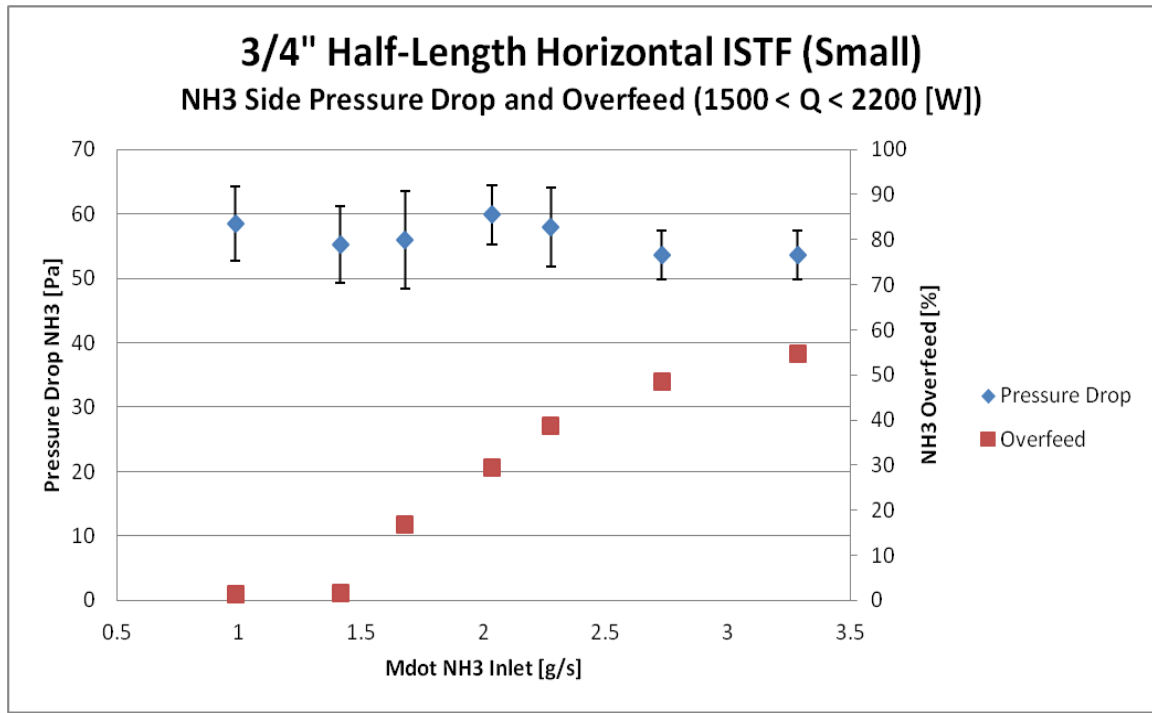


Figure 90: Pressure drop and over feed demands on the 3/4" half-length horizontal ISTF (small case) tube.

Figure 90 shows the refrigerant side pressure drop and overfeed which was required for the top performing horizontal half-length ISTF tube in the small test casing. These negligible requirements, which produced up to 2200 [W] of heat transfer, can be compared to results from falling film in Figure 91 and Figure 92. As a reference, research in this study encompassed refrigerant flow rates from $.00042 < [\text{kg/ms}] < .001$; this shows a 98% reduction in required refrigerant delivery rate for fully wetted operation when compared with Figure 91.

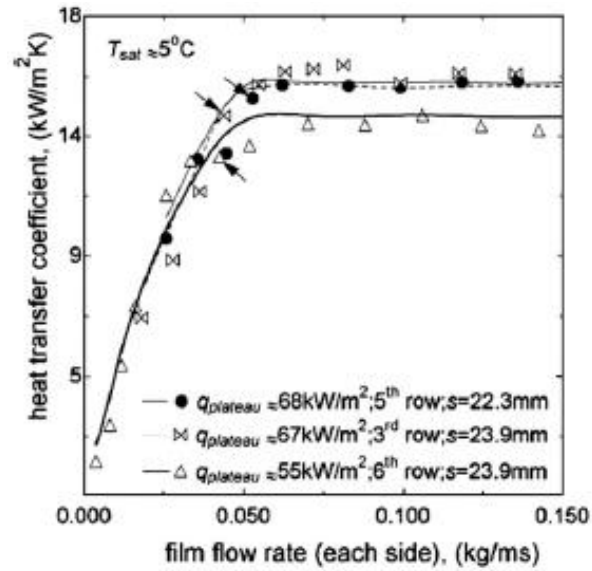


Figure 91: Flow rate in falling film using R134a [29].

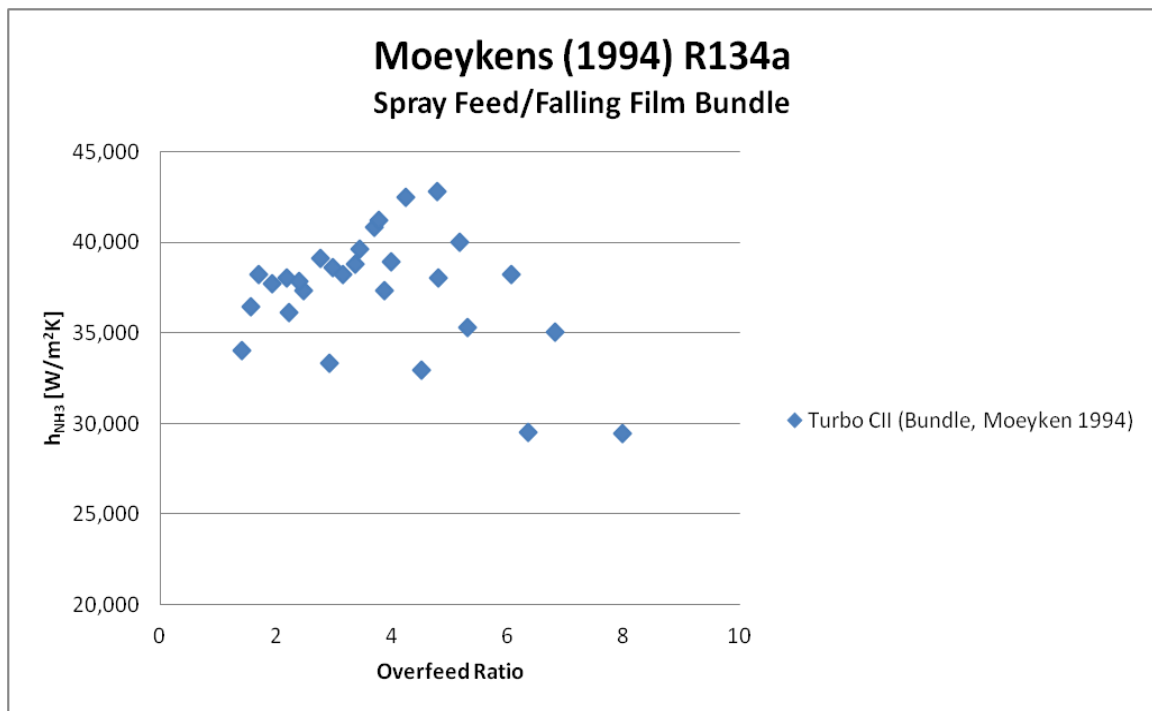


Figure 92: Falling film over feed requirements for Moeykens' top performer [15].

Furthermore, pressure drop results shown in Figure 90 demonstrate a 96% reduction from typical values demonstrated using the force-fed manifold shown in Figure 93. Feed delivery systems for falling film can be complex and sensitive to distribution non-uniformity [19]. As a result, low LGTE applications which require simplicity and reliability may benefit from the capillary feed.

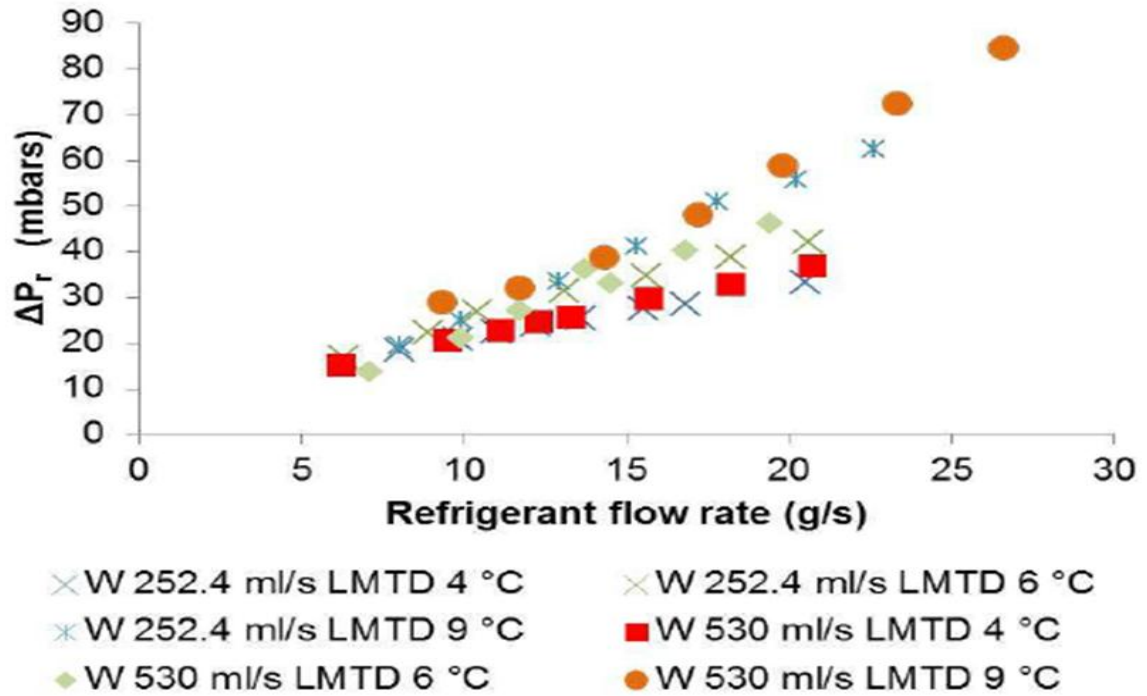


Figure 93: Refrigerant pressure drop for the forced-fed microchannel configuration [23].

The original intent of the capillary feed concept was to deliver admirable performance in LGTE applications where LMTD and heat flux were too low to induce boiling. In these conditions, other feed configurations such as falling film, flow boiling, and pool boiling revert to single phase convective heat transfer largely. With low refrigerant delivery rates, the ability of the capillary feed to induce thin film evaporation makes it likely to be a clear choice for this application. Unfortunately, it was not possible to conduct testing under these conditions for reasons of large uncertainty and test condition constraints. A future study which assesses performance of this concept in the absence of boiling is likely to show valuable results.

Future Work Suggestions

Feed Tube Optimization:

The current feed tubes developed for this study were the first of their kind. During development, various general concepts were tested and it was deduced visually that the channel feed mechanism is the best design of those tested. Variables such as fluid selection, operating flow rates, tube length, expected heat flux, material compatibility, temperature, and surface curvature influence the specific dimensions of the optimal feed tube. There is likely much to be gained from additional work which optimizes feed tube geometry for various test conditions, and possibly to develop correlations which produce a simple model for designing a feed tube for a specific application.

Test Casing Variation and Bundle:

There is some reason to suspect that the evaporator surfaces may have been flooding at times, especially in the horizontal test configuration, for some evidence see Figure 73 and the surrounding discussion. It is possible that if this is true it could be due flow distribution issues or other variables related to the test casing and small vapor flow gap between the tube and casing wall. It is reasonable to suspect that high velocity vapor could be disturbing the horizontal liquid feed pool and creating localized surface flooding. A bundle test is both more valuable to larger scale LGTE applications, such as OTEC, as more energy can be transferred; but, there is also some evidence that switching to a bundle – and consequently larger test casing – could improve numbers (Figure 16). Also, a test casing with a larger vapor flow volume is less sensitive to flooding due to fluctuations in delivery flow rate and heat flux.

Additional Surface Geometry Tests:

The surface enhancements tested in this research were selected because it was believed that they would perform well for the given test conditions. However, only two surface variations for the $\frac{3}{4}$ " tube were tested, and a unique 2" tube as well. A study which tests and reports performance of the capillary feed with various enhancement and working fluid combinations would be of great value to literature. Proprietary issues prevented this author from reporting the details of the surfaces used. There is ample evidence, as promulgated in the literature review section of this work, which shows that tube enhancement geometry can have a profound effect on performance.

Below Nucleate Boiling Application Test:

The capillary fed enhanced tubular evaporator was designed to deliver thin film evaporation in low refrigerant delivery rate LGTE applications below the onset of nucleate boiling. The high density of intricate surface features results in a large net area of fluid meniscus. Thin film evaporation occurs at the points where the meniscus contacts the solid surfaces of the microstructure. With the low heat flux experienced in many LGTE applications, small microstructures which promote meniscus formation and short fluid conduction lengths, will also often still be able to provide capillary fluid delivery for adequate wetting and should therefore be sought out. In contrast to the capillary feed, an evaporator tube installed in a sub-nucleate boiling falling film configuration would experience flooding of the enhanced surface features, resulting in a thick film with no meniscus formation, and heat transfer would predominately take place by way of single phase convection only. It was not possible to test sub-boiling applications in this research due to high uncertainty and certain test operational constraints; therefore, a future study which focuses on sub-boiling flow would be very illuminating.

Appendix

Illustrations

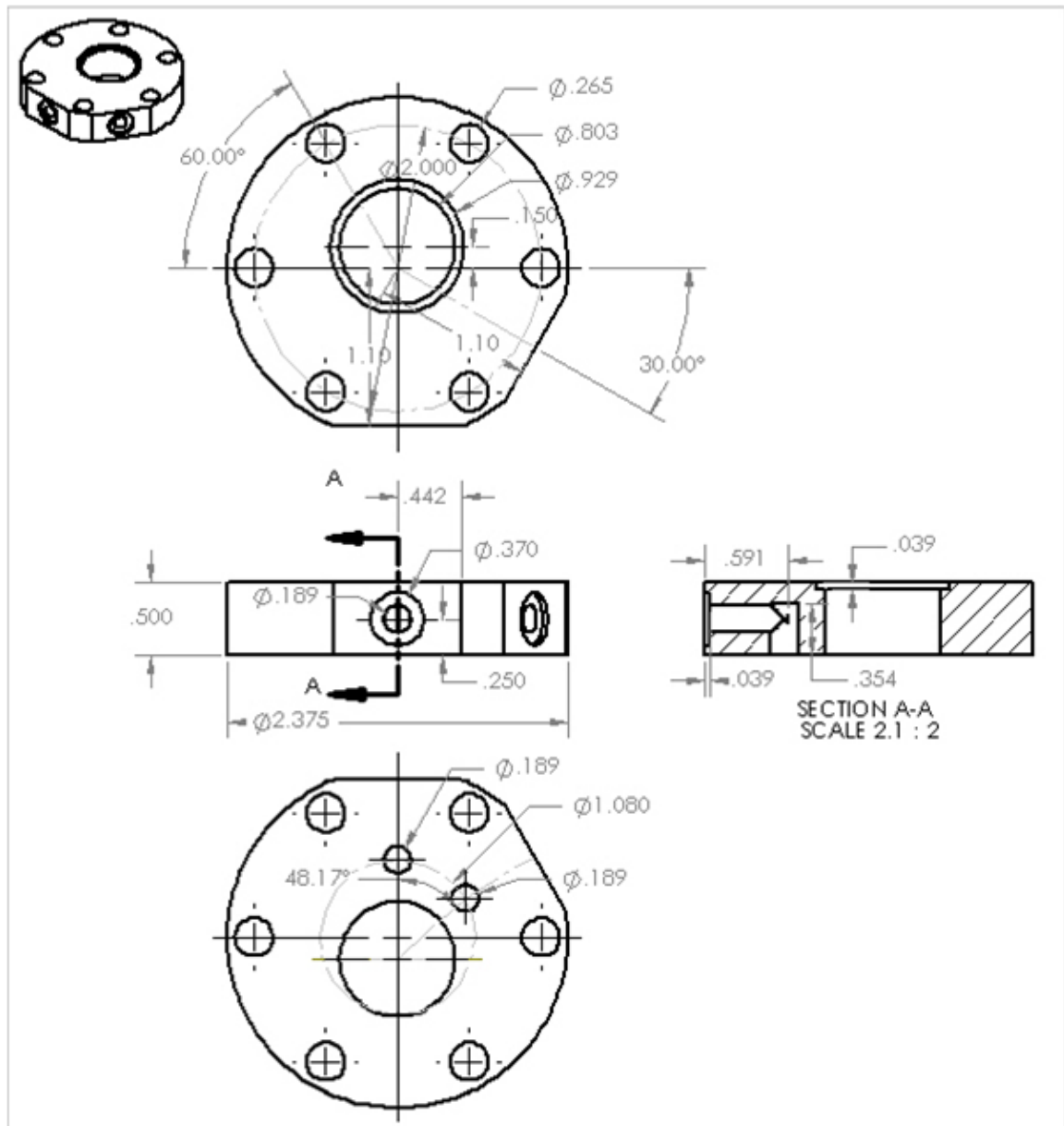


Figure 94: Large test casing top manifold showing liquid inlet and vapor outlet ports.

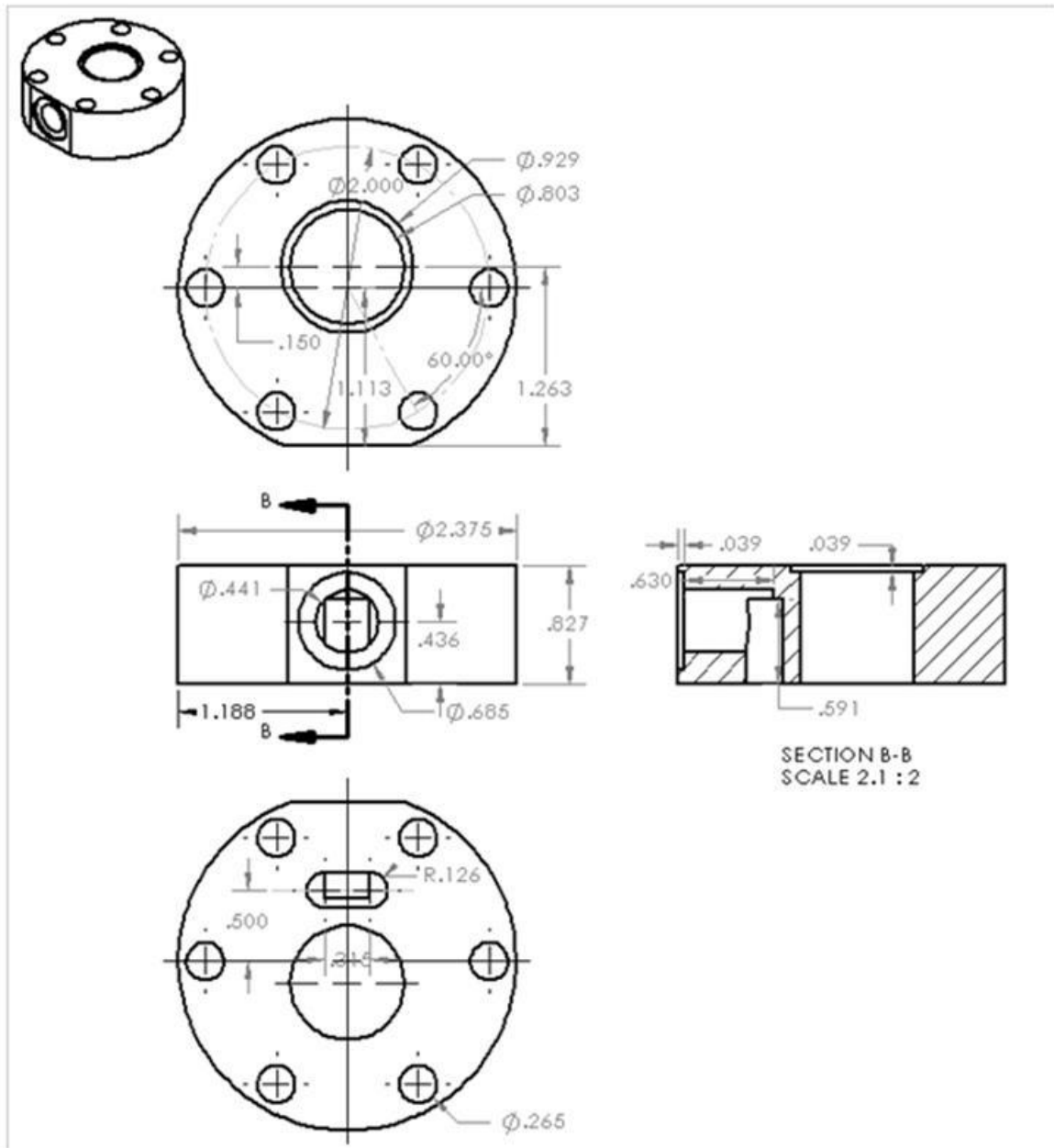


Figure 95: Large test casing bottom manifold showing bi-pass liquid outlet port.

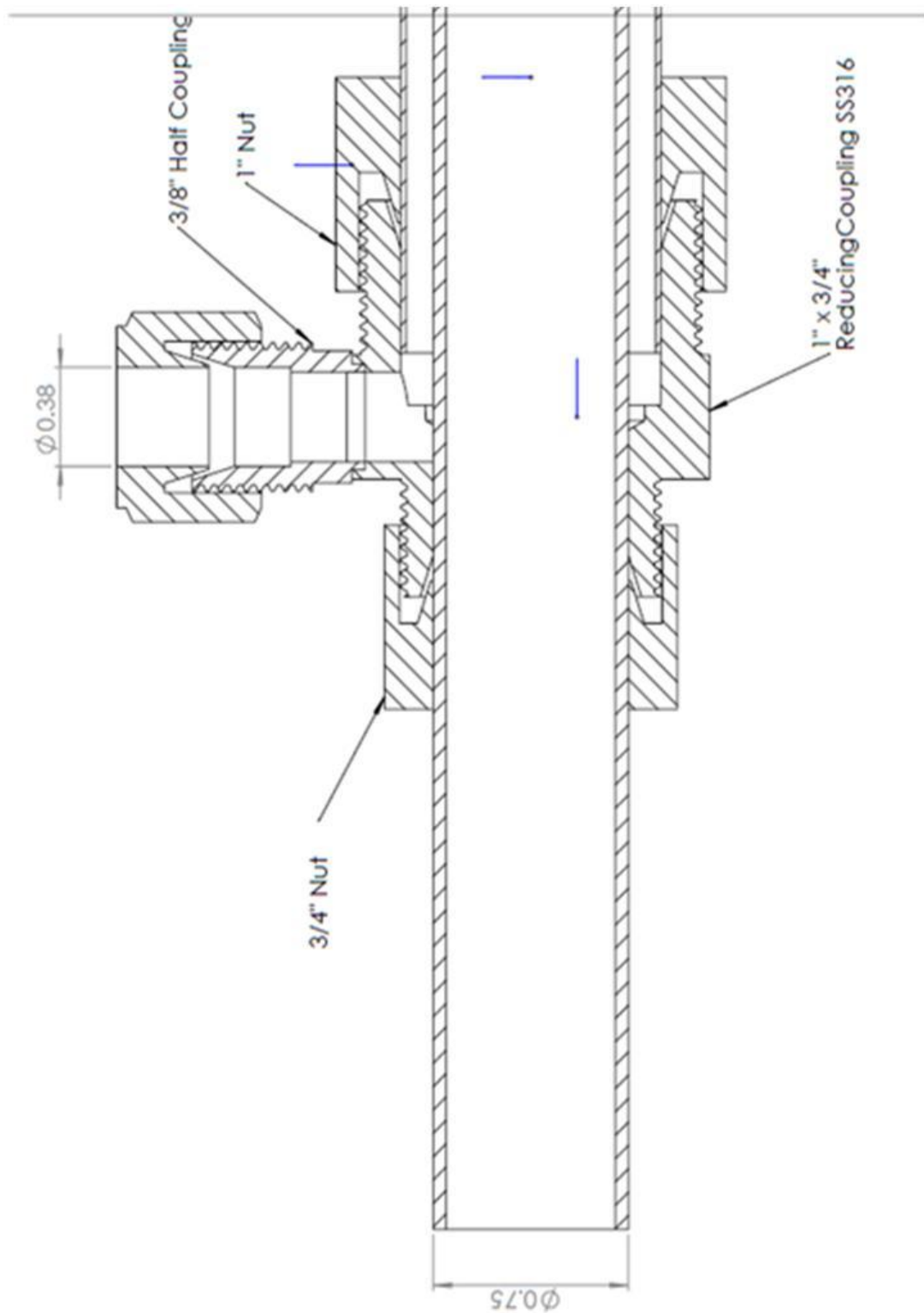


Figure 96: Small test casing inlet cross section drawing.

Variable±Uncertainty	Partial derivative	% of uncertainty
hNH3 = 17110±3132		
$D_i = 0.01614 \pm 0.0002$ [m]	$\partial h_{NH3} / \partial D_i = -1.552E+06$	0.98 %
$D_o = 0.01818 \pm 0.0002$ [m]	$\partial h_{NH3} / \partial D_o = -320955$	0.04 %
$hH2O = 23935 \pm 831.6$	$\partial h_{NH3} / \partial hH2O = -0.5754$	2.33 %
$L = 1.524 \pm 0.005$ [m]	$\partial h_{NH3} / \partial L = -21143$	0.11 %
$\dot{m}H2O_{cool} = 0.0913 \pm 0.004565$	$\partial h_{NH3} / \partial \dot{m}H2O_{cool} = 352928$	26.46 %
$\dot{m}H2O_{warm} = 0.5 \pm 0.005$	$\partial h_{NH3} / \partial \dot{m}H2O_{warm} = 0$	0.00 %
$P_{atm} = 101325 \pm 500$ [Pa]	$\partial h_{NH3} / \partial P_{atm} = -0.00003622$	0.00 %
$P_{satHX} = 1.050E+06 \pm 2649$ [Pa]	$\partial h_{NH3} / \partial P_{satHX} = 0.4569$	14.93 %
$TH2O_{incool} = 17.46 \pm 0.237$	$\partial h_{NH3} / \partial TH2O_{incool} = -6987$	27.95 %
$TH2O_{inwarm} = 29.13 \pm 0.032$	$\partial h_{NH3} / \partial TH2O_{inwarm} = -6434$	0.43 %
$TH2O_{outcool} = 22.07 \pm 0.229$	$\partial h_{NH3} / \partial TH2O_{outcool} = 6986$	26.09 %
$TH2O_{outwarm} = 28.33 \pm 0.031$	$\partial h_{NH3} / \partial TH2O_{outwarm} = -8185$	0.66 %
Q = 1761±153.6 [W]		
$D_i = 0.01614 \pm 0.0002$ [m]	$\partial Q / \partial D_i = 0$	0.00 %
$D_o = 0.01818 \pm 0.0002$ [m]	$\partial Q / \partial D_o = 0$	0.00 %
$hH2O = 23935 \pm 831.6$	$\partial Q / \partial hH2O = 0$	0.00 %
$L = 1.524 \pm 0.005$ [m]	$\partial Q / \partial L = 0$	0.00 %
$\dot{m}H2O_{cool} = 0.0913 \pm 0.004565$	$\partial Q / \partial \dot{m}H2O_{cool} = 19292$	32.87 %
$\dot{m}H2O_{warm} = 0.5 \pm 0.005$	$\partial Q / \partial \dot{m}H2O_{warm} = 0$	0.00 %
$P_{atm} = 101325 \pm 500$ [Pa]	$\partial Q / \partial P_{atm} = -0.00000198$	0.00 %
$P_{satHX} = 1.050E+06 \pm 2649$ [Pa]	$\partial Q / \partial P_{satHX} = 0$	0.00 %
$TH2O_{incool} = 17.46 \pm 0.237$	$\partial Q / \partial TH2O_{incool} = -381.9$	34.72 %
$TH2O_{inwarm} = 29.13 \pm 0.032$	$\partial Q / \partial TH2O_{inwarm} = 0$	0.00 %
$TH2O_{outcool} = 22.07 \pm 0.229$	$\partial Q / \partial TH2O_{outcool} = 381.9$	32.41 %
$TH2O_{outwarm} = 28.33 \pm 0.031$	$\partial Q / \partial TH2O_{outwarm} = 0$	0.00 %
U = 9623±922.9 [W/m²K]		
$D_i = 0.01614 \pm 0.0002$ [m]	$\partial U / \partial D_i = -280378$	0.37 %
$D_o = 0.01818 \pm 0.0002$ [m]	$\partial U / \partial D_o = -280378$	0.37 %
$hH2O = 23935 \pm 831.6$	$\partial U / \partial hH2O = 0$	0.00 %
$L = 1.524 \pm 0.005$ [m]	$\partial U / \partial L = -6314$	0.12 %
$\dot{m}H2O_{cool} = 0.0913 \pm 0.004565$	$\partial U / \partial \dot{m}H2O_{cool} = 105397$	27.18 %
$\dot{m}H2O_{warm} = 0.5 \pm 0.005$	$\partial U / \partial \dot{m}H2O_{warm} = 0$	0.00 %
$P_{atm} = 101325 \pm 500$ [Pa]	$\partial U / \partial P_{atm} = -0.00001082$	0.00 %
$P_{satHX} = 1.050E+06 \pm 2649$ [Pa]	$\partial U / \partial P_{satHX} = 0.1364$	15.34 %
$TH2O_{incool} = 17.46 \pm 0.237$	$\partial U / \partial TH2O_{incool} = -2086$	28.71 %
$TH2O_{inwarm} = 29.13 \pm 0.032$	$\partial U / \partial TH2O_{inwarm} = -1922$	0.44 %
$TH2O_{outcool} = 22.07 \pm 0.229$	$\partial U / \partial TH2O_{outcool} = 2086$	26.80 %
$TH2O_{outwarm} = 28.33 \pm 0.031$	$\partial U / \partial TH2O_{outwarm} = -2444$	0.67 %

Figure 97: Uncertainty propagation for a typical case, independent NH3 loop.

Correlational Derivations

Onset of Nucleate Boiling – Liu (2005):

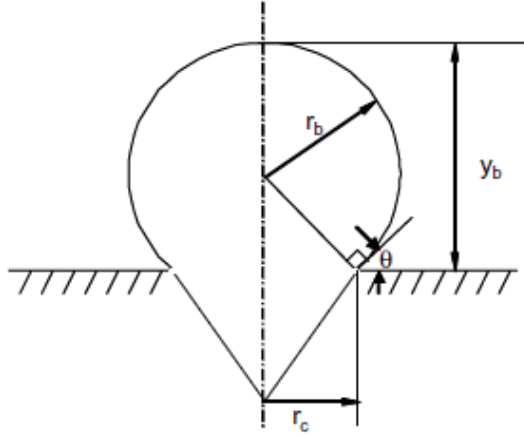
This correlation, specifically designed to estimate the onset of nucleate boiling in microchannels, comes from Liu, et al. [31]. Empirical test result data was used as inputs for saturation pressure; and, Wilson plot results were used in conjunction with the two-dimensional resistance circuit equation to estimate wall temperature. Test data provided estimates of temperature and pressure which were used, along with the inlet and outlet quality assumptions for saturated flow, to find necessary input properties. Ultimately, the following equation was used to find the heat flux at the onset of boiling given the measured wall superheat.

$$T_{wall} - T_{sat} = \frac{2\sigma C}{\rho_{vap} h_{fg} k_{liq}} q''_{wall} + 2 \sqrt{T_{sat} \frac{2\sigma C}{\rho_{vap} h_{fg} k_{liq}} q''_{wall}}$$

Where:

$$C = 1 + \cos \theta$$

Also known as the “shape factor”, and is a function of the θ which is shown below; for our purposes, $\theta \approx 90^\circ$:



$$q''_{wall} = \left(\frac{\alpha}{1 + 2\eta_{fin}\alpha} \frac{W_{chan} + t_{fin}}{H_{fin}} \right) q''$$

Where the fin efficiency was calculated from [32] as follows:

$$\eta_{fin} = C_2 \frac{K_1(mr_1)I_1(mr_{2c}) - I_1(mr_1)K_1(mr_{2c})}{I_0(mr_1)K_1(mr_{2c}) + K_0(mr_1)I_1(mr_{2c})}$$

Where:

$$C_2 = \frac{\frac{2r_1}{m}}{(r_{2c}^2 - r_1^2)}$$

$$r_{2c} = r_2 + \frac{t_{fin}}{2}$$

$$m = \sqrt{\frac{2h_{ref}}{k_{fin}t_{fin}}}$$

I and K are modified Bessel functions and values were looked up using table in Appendix B5 of [32]. Here, r_1 is the radius from the tube center to the fin base, and r_2 is the radius from the tube center to the top of the fin.

h_{ref} was calculated by using the average Nusselt number for the microchannels:

$$\bar{h}_{ref} = \frac{\overline{Nu}_{k_{liq}}}{L}$$

The average Nusselt number, for laminar flow through a microchannel, was found in correlational tables available in [33] using the channel aspect ratio and the Knudsen number. The Knudsen number is defined:

$$Kn = \frac{\lambda_{MFP}}{D_h}$$

In order to find the mean free path was found by using [34] according to the following equations:

$$\lambda_{MFP} = \frac{1}{\pi n \sigma^2 \sqrt{2}}$$

$$n = \frac{\rho}{\bar{m}}$$

$$\bar{m} = \text{Molecular weight}$$

$$\sigma = \text{effective molecular diameter}$$

The effective molecular diameter is found from [17].

Onset of Nucleate Boiling – Hsu (1962):

This is one of the earliest correlations for predicting the onset of nucleate boiling for a fluid, and is still one of the most widely used. It is based on a simple pool boiling analogy. It has also been modified in several subsequent works which produced correlations for predicting the onset of boiling while accounting for additional variables. As was done using Liu's (2005) correlation, measured temperatures from experimental data were input into this model, and the expected heat flux at the onset of nucleate boiling was calculated. Hsu's correlation is as follows [35]:

$$q'' = \frac{k_{liq} h_{fg} \rho_{vap} (T_{wall} - T_{sat})^2}{12.8 \sigma T_{sat}}$$

Onset of Nucleate Boiling – Kandlikar Pool Boiling:

Kandlikar's pool boiling correlation uses empirically measured temperature inputs and calculates expected heat flux at the onset of boiling as follows [36]:

$$T_{wall} - T_{sat} = \sqrt{\frac{8 \sigma T_{sat} \nu_{vap} q''}{h_{fg} k_{liq}}}$$

Onset of Nucleate Boiling – Kandlikar Flow Boiling:

Kandlikar's flow boiling correlation uses empirically measured temperature inputs and calculates expected heat flux at the onset of boiling as follows [36]:

$$T_{wall} - T_{sat} = \sqrt{\frac{8 \sigma T_{sat} (\nu_{vap} - \nu_{liq}) q''}{h_{fg} k_{liq}}}$$

Pool Boiling:

This correlation, from Gorenflo et. al, 2010, is based on empirical research and the observation that enhanced and smooth tubes perform the same at heat flux of 100 [kW/m²] and a pressure of .1 [bar] [37]. This is apparent in Figure 98 where plain and finned tubes are shown of the same dimension and using the same refrigerant.

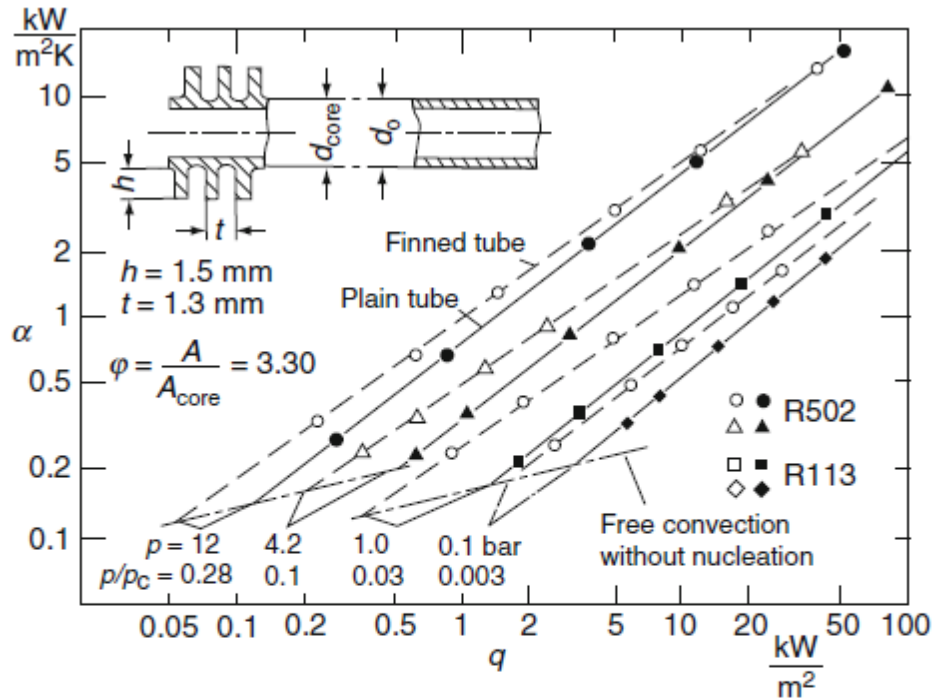


Figure 98: h_{ref} for finned and plain tubes is equivalent for 100 [kW/m²] and .1 [bar] [37].

The method works by calculating the heat transfer coefficient at known reference conditions for a smooth tube, using well established empirical results, for the chosen working fluid. Next, a series of corrections are applied to account for surface enhancements, operating pressure, and heat flux for the actual configuration.

The reference conditions are:

$$q_{ref} = 20 \left[\frac{kW}{m^2} \right]$$

$$P_{ref} = .1 [bar]$$

The heat transfer coefficient for ammonia on a smooth tube at the reference conditions is calculated below:

$$h_{smooth,ref} = 3.58 P_f^{.6}$$

Where:

$$P_f = \frac{h_{lv} \rho_{liq} \rho_{vap}}{\sigma T_{sat,ref} (\rho_{liq} - \rho_{vap})}$$

$$h_{lv} = a h_{fg}$$

$$a = \frac{2\hat{\sigma}}{2 - \hat{\sigma}} \sqrt{\frac{\bar{M}}{2\pi \bar{R} T_{sat,ref}}} \frac{P_{ref} \bar{M} h_{fg}}{\bar{R} T_{sat,ref}^2}$$

$$\hat{\sigma} = 1 \text{ (homogenous liquid)}$$

$$\bar{M} = \text{Molar mass}$$

$$\bar{R} = \text{Ideal gas law}$$

Next, a slope correction is made to the reference heat transfer coefficient in order to account for a different heat flux. This estimates the heat transfer coefficient for a smooth tube at 100 [kW/m²] and .1 [bar], the conditions at which we know smooth and finned tubes are equivalent.

$$h_{smooth,100,Pref} = h_{smooth,ref} \left(\frac{q_{100}}{q_{ref}} \right)^{n_{ref}} Fp_{ref}$$

Where:

$$n_{ref} = .95 - .3 P_{ref}^{.3}$$

$$Fp_{smooth,ref} = .7 * P_{ref}^{.2} + 4 * P_{ref} + \frac{1.4 * P_{ref}}{1 - P_{ref}}$$

Above, n is an exponent which can be used to account for surface geometry, and Fp is a term which can be used to account for operating pressure. These terms are manipulated below, along with additional heat flux corrections, in order to produce the heat transfer coefficient for pool boiling on the target surface, at the target heat flux, and at the target operating pressure.

As previously justified:

$$h_{smooth,100,Pref} = h_{finned,100,Pref}$$

Thus:

$$h_{finned,100,Pref} = h_{smooth,ref} \left(\frac{q_{100}}{q_{ref}} \right)^{n_{ref}} Fp_{smooth,ref}$$

For a finned tube at the reference conditions:

$$h_{finned,ref} = h_{finned,100,Pref} \left(\frac{q_{ref}}{q_{100}} \right)^{n_{fref}}$$

Where the finned surface correction at the new reference pressure is given:

$$n_{fref} = n_{ref} - .1 * \left(\frac{H_{fin}}{W_{chan}} \right)$$

Next, the finned tube pressure is corrected to the target operating pressure:

$$h_{finned,q_{ref}} = h_{finned,ref} \left(\frac{Fp_{fin}}{Fp_{fin,ref}} \right)$$

Where:

$$Fp_{fin} = .7 * P_{fin}^{.2} + 4 * P_{fin} + \frac{1.4 * P_{fin}}{1 - P_{fin}}$$

$$Fp_{fin,ref} = .7 * P_{fin,ref}^{.2} + 4 * P_{fin,ref} + \frac{1.4 * P_{fin,ref}}{1 - P_{fin,ref}}$$

$$P_{fin,ref} = \frac{P_{ref}}{\sqrt{\psi}}$$

$$P_{fin} = \frac{P_{sat}}{\sqrt{\psi}}$$

Where a geometric correction factor for the enhancement is used:

$$\psi = \frac{2H_{fin} + W_{chan} + t_{fin}}{W_{chan} + t_{fin}}$$

Finally, the pressure corrected value for the finned surface is brought to the target heat flux:

$$h_{finned} = h_{finned,q_{ref}} \left(\frac{q''}{q_{ref}} \right)^{n_f}$$

Where:

$$n_f = n - .1 * \left(\frac{H_{fin}}{W_{chan}} \right)$$

$$n = .95 - .3P_{sat}^{.3}$$

This derivation was tested against reported pool boiling values from the same reference in literature [37], using different refrigerants and geometries, and results were in perfect agreement.

Flow Boiling:

This correlation is based on an empirically derived model from Li, et. al., (2010) [38]. It is based on 3700 data points, and is in very good agreement with other results reported in literature for saturated flow boiling in microchannels. The correlation is as follows:

$$q'' = \frac{q_{wall}''}{\frac{\alpha}{1 + 2\eta_{fin}\alpha} \frac{W_{chan} + t_{fin}}{H_{fin}}}$$

Where η_{fin} , is fin efficiency, and is calculated the same was as shown above in the Liu (2005) correlation using [32]. The heat flux equation shown above is manipulated in order to find the wall heat flux in the microchannel, and then heat transfer coefficient for the flow boiling in microchannels at the input heat flux is calculated as follows:

$$h_{ref} = 334Bl^{.3}(BoRe_{liq}^{.36})^{.4} \frac{k_{liq}}{d_h} = \frac{q_{wall}''}{T_{wall} - T_{sat}}$$

$$Bl = \frac{q_{wall}''}{Gh_{fg}} = A_{c,chan} \text{ (Assumes all mass evaporates } \dot{m}_{liq} = \dot{m}_{vap} = \dot{m})$$

$$G = \frac{\dot{m}}{A_{c,chan}}$$

$$\dot{m} = \frac{q_w''}{h_{fg}}$$

$$Bo = \frac{g(\rho_{liq} - \rho_{vap})d_h^2}{\sigma}$$

$$g = 9.81 \left[\frac{m}{s^2} \right]$$

$$Re_{liq} = \frac{Gd_h}{\mu_{liq}} = \frac{q_{wall}'' d_h}{h_{fg}\mu_{liq}A_{c,chan}}$$

Thin Film Evaporation:

This correlation is based on a short history of analytical studies which derive models for the evaporating thin film region of a meniscus in a microchannel. The correlation used here draws primarily from a study published by Wang, et. al., in 2008 [39]; however, it was necessary for this author to obtain additional clarifications and cross checks in order to develop a working understanding of Wang's model. As a result, additional references were made to works by Wang, et. al. (2007) [40] and Ha,

et. al. (1996) [41]. The subject of model thin film evaporation in microchannels is a complex and in depth subject that goes beyond the scope of this writing; however, a brief description of the physics which contributed to the referenced correlation is now given.

When liquid refrigerant enters a microchannel, a disjoining pressure develops between the solid surfaces of the channel and the liquid. This pressure, which varies with fluid properties, creates a very thin layer of fluid which is known as the “non-evaporating layer”. It is in this non-evaporating layer that disjoining pressure is most strong; however, disjoining pressure is not strong enough to create a scenario where all of the fluid in the microchannel is drawn into this ultra-thin layer along the solid surfaces only. As a result, this layer must eventually begin to thicken between the dry solid surface at the top of the channel walls and the fully flooded region at the bottom of the microchannel. As this non-evaporating layer thickens, disjoining pressure decreases and soon capillary pressure becomes dominant. The interaction between capillary forces and disjoining forces dictate the rate at which the layer of fluid thickens, and the resulting angle of thickening fluid sets the radius of a fluid meniscus which results between the two walls.

The vast majority of heat transfer in the microchannel takes place in the thin film region, a region between the meniscus and non-evaporating layer. Here, fluid is free to evaporate, but the conduction distance between the microchannel wall and the evaporating surface is very small, so overall thermal resistance is also very small. For this reason, many thin film models neglect heat transfer in the meniscus and non-evaporating layer in order to simplify the complexity of differential equations resulting from the governing equations that describe the physics in this context. The correlation which is used here, solves for the thickness of the non-evaporating layer, and uses fluid properties in order to set the thin film profile. Mass flux into the thin film region, from the meniscus, is estimated using a simplified evaporative model. The suppression of evaporation in the non-evaporating region due to disjoining pressure is neglected, and it is shown that the resulting effect is negligible. A model of the thin film region, as described above, is shown in Figure 99.

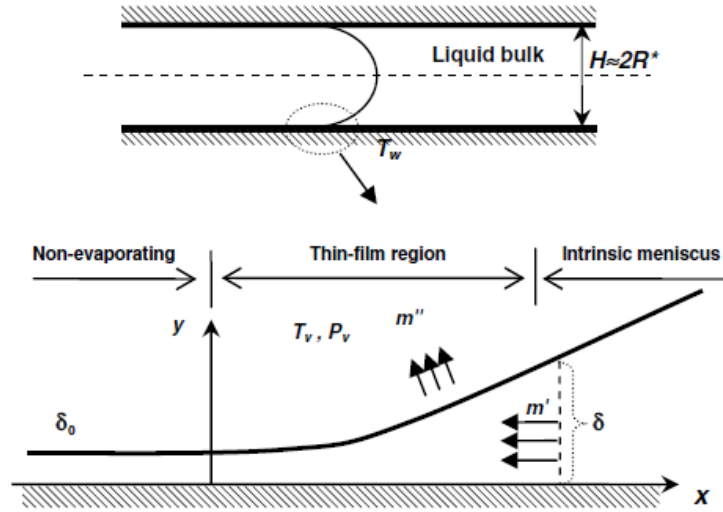


Figure 99: Microchannel thin film profile and dynamics [39].

The following derivation predicts the total heat transfer, q_t , from the thin film region on one side of the microchannel. The total heat transfer for a surface is thus found by multiplying this value by two and then again by the total number of channels on the surface. This total heat transfer equation was found by integrating the simplified governing equations (a function of x as shown in Figure 99) for the thin film region and then solving the result from the thickness of the non-evaporating layer to infinity. Please see [39] for details of this integration. By using this method the entire meniscus region is accounted for; however, only the physics which apply to thin film evaporation are extrapolated here and at some point beyond the true thin film region this approach begins to under-predicts heat transfer. As a result, the results from this correlation may be slightly lower than actual values; but should provide a good rule of thumb so long as there is no nucleate boiling on the actual surface.

$$q_t = \sqrt{\frac{2Ah_{fg}h_{lv}(T_{wall} - T_{sat})}{v_{liq}} \ln\left(\frac{k_{liq}}{h_{lv}\delta_0} + 1\right)}$$

The non-evaporating layer thickness is found here:

$$\delta_0 = \sqrt[3]{\frac{\bar{V}_{liq}T_{sat}A}{\bar{M}h_{fg}(T_{wall} - T_{sat})}}$$

Where:

\bar{M} = Molar mass

\bar{V}_{liq} = Liquid molar volume

A = Hamaker dispersion coefficient

A reasonable approximation for the Hamaker constant was found using [42] for the interaction between water and aluminum oxide. The heat transfer coefficient for the liquid-vapor interface could be computed as follows:

$$h_{lv} = ah_{fg}$$

$$a = \frac{2\hat{\sigma}}{2 - \hat{\sigma}} \sqrt{\frac{\bar{M}}{2\pi\bar{R}T_{sat}}} \frac{P_{sat}\bar{M}h_{fg}}{\bar{R}T_{sat}^2}$$

Where:

$$\hat{\sigma} = 1 \text{ (homogenous liquid)}$$

$$\bar{R} = \text{Universal gas constant}$$

Critical Heat Flux

Two methods for computing critical heat flux were executed in order to ensure that the effect of microchannel confinement did not call the result from the standard method into question. The traditional method for calculating critical heat flux, which neglects surface confinement, was performed as follows [32]:

$$q''_{crit} = .149\rho_{vap}h_{fg} \sqrt[4]{\frac{\sigma 9.81(\rho_{liq} - \rho_{vap})}{\rho_{vap}^2}}$$

The modified method, which uses the critical heat flux calculated above but incorporates confinement, is executed as follows [44]:

$$q''_{crit,modified} = q''_{crit} \frac{1.14\lambda_D^2}{D_h}$$

Where:

$$\lambda_D = s\pi \sqrt[4]{\frac{3\sigma}{9.81(\rho_{liq} - \rho_{vap})}}$$

$$s = \frac{1}{1 + 2.56E^{-6}(Re_{liq}F^{1.25})^{1.17}}$$

$$F = 1$$

Works Cited

- [1] Ammar, Y., Joyce, S., Norman, R., Wang, Y., Roskilly, A. P., 2012, “Low Grade Thermal Energy Sources and Uses from the Process Industry in the UK,” *Applied Energy*, 89, pp. 3 – 20.
- [2] Moran, M. J., Shapiro, H. N., 2008, *Fundamentals of Engineering Thermodynamics 6th Edition*, John Wiley & Sons, Inc., USA.
- [3] Tchanche, B. F., Lambrinos, G., Frangoudakis, A., Papadakis, G., 2011, “Low-Grade Heat Conversion Into Power Using Organic Rankine Cycles – A Review of Various Applications,” *Renewable and Sustainable Energy Reviews*, 15, pp. 3963–3979.
- [4] Chan, C. W., Ling-Chin, J., Roskilly, A. P., 2013, “A Review of Chemical Heat Pumps, Thermodynamic Cycles, and Thermal Energy Storage Technologies for Low Grade Heat Utilisation,” *Applied Thermal Engineering*, 50, pp. 1257 – 1273.
- [5] Wang, D., Ling, X., Peng, H., Liu, L., Tao, L., 2013, “Efficiency and Optimal Performance Evaluation of Organic Rankine Cycle for Low Grade Waste Heat Power Generation,” *Energy*, 50, pp. 343 – 352.
- [6] Hung, T. C., Wang, S. K., Kuo, C. H., Pei, B. S., Tsai, K. F., 2010, “A Study of Organic Working Fluids on System Efficiency of an ORC Using Low-Grade Energy Sources,” *Energy*, 35, pp. 1403 – 1411.
- [7] Takahashi, P. and Andrew Trenka. 1996. *Ocean Thermal Energy Conversion*. Chichester: John Wiley and Sons, Ltd.
- [8] Natural Energy Laboratory of Hawaii Authority, 2013, from <http://www.nelha.org/about/history.html>
- [9] United States Department of Energy, 2013, from http://www.eere.energy.gov/basics/renewable_energy/ocean_thermal_energy_conv.html
- [10] Rajagopalan, K., Nihous, G. C., 2013, “Estimates of Global Ocean Thermal Energy Conversion (OTEC) Resources Using an Ocean General Circulation Model,” *Renewable Energy*, 50, pp. 532 – 540.
- [11] Wu, C., 1987, “A Performance Bound for Real OTEC Heat Engines,” *Ocean Engineering*, 14 (4), pp. 349-354.
- [12] Coleman, W. H., 1980, “Westinghouse OTEC Power Systems,” *Energy*, 5, pp. 493-501.
- [13] Sun, F., Ikegami, Y., Jia, B., Arima, H., 2012, “Optimization Design and Exergy Analysis of Organic Rankine Cycle in Ocean Thermal Energy Conversion,” *Applied Ocean Research*, 35, pp. 38-46.

- [14] Ganic, E. N., Wu, J., “On the Selection of Working Fluids for OTEC Power Plants,” *Energy Conversion and Management*, 20, pp. 9 – 22.
- [15] Moeykens, S. A., 1994, “Heat Transfer and Fluid Flow in Spray Evaporators with Application to Reducing Refrigerant Inventory,” Ph.D Thesis, Mechanical Engineering, Iowa State University.
- [16] Centers for Disease Control and Prevention, 2013, from <http://www.cdc.gov/niosh/npg/npgd0028.html>
- [17] Kammeyer, C. W., Whitman, D. R., 1972, “Quantum Mechanical Calculation of Molecular Radii. I. Hydrides of Elements of Periodic Groups IV through VII,” *The Journal of Chemical Physics*, **56**(9), pp. 4419-4421.
- [18] Garret-Price, B. A., Smith, S. A., Watts, R. L., 1985, *Fouling of Heat Exchangers*, Noyes Publications, Park Ridge, NJ, USA.
- [19] Wang, R. Z., Xia, Z. Z., Wang, L. W., Lu, Z. S., Li, S. L., Li, T. X., Wu, J. Y., He, S., 2011, “Heat Transfer Design in Adsorption Refrigeration Systems for Efficient Use of Low-Grade Thermal Energy,” *Energy*, 36, 5425 – 5439.
- [20] Rose, J. W., 2004, “Heat-Transfer Coefficients, Wilson Plots, and Accuracy of Thermal Measurements,” *Experimental Thermal and Fluid Science*, 28 pp. 77 – 86.
- [21] Fernandez-Seara, J., Uhia, F. J., Sieres, J. A., 2007, “General Review of the Wilson Plot Method and its Modifications to Determine Convection Coefficients in Heat Exchange Devices,” *Applied Thermal Engineering*, 27, pp. 2745 – 2757.
- [22] Fava, J. A., Thomas, D. L., 1978, “Use of Chlorine to Control OTEC Biofouling,” *Ocean Engineering*, 5, pp. 269 – 288.
- [23] Jha, V. C., 2012, “High-Performance Tubular Evaporator Utilizing High Aspect Ratio Manifold Microchannels,” Ph.D Thesis, Mechanical Engineering, University of Maryland, College Park.
- [24] Thome, J. R., 2010, *Wolverine Engineering Data Book III*, Swiss Federal Institute of Technology Lausanne, Switzerland.
- [25] Christians, M., Thome, J. R., 2012, “Falling Film Evaporation on Enhanced Tubes, Part 1: Experimental Results for Pool Boiling, Onset-of-Dryout and Falling Film Evaporation,” *International Journal of Refrigeration*, 35, pp. 300-312.
- [26] Mukherjee, A., 2009, “Contribution of Thin-Film Evaporation During Flow Boiling Inside Microchannels,” *International Journal of Thermal Sciences*, 48, pp. 2025 – 2035.
- [27] Cetegen, E., 2010, “Force Fed Microchannel High Heat Flux Cooling Utilizing Microgrooved Surfaces,” Ph.D Thesis, Mechanical Engineering, University of Maryland, College Park.

- [28] Habert, M., 2009, "Falling Film Evaporation on a Tube Bundle with Plain and Enhanced Tubes," Ph.D Thesis, Heat and Mass Transfer, Ecole Polytechnique Federale De Lausanne.
- [29] Ribatski, G., Thome, J. R., 2007, "Experimental Study on the Onset of Local Dryout in an Evaporating Falling Film on Horizontal Plain Tubes," *Experimental Thermal and Fluid Science*, 31, pp. 483–493.
- [30] Christians, M., Thome, J. R., 2012, "Falling Film Evaporation on Enhanced Tubes, Part 2: Prediction Methods and Visualization," *International Journal of Refrigeration*, 35, pp. 313 – 324.
- [31] Liu, D., Lee, P., Garimella, S. V., 2005, "Prediction of the Onset of Nucleate Boiling in Microchannel Flow," *International Journal of Heat and Mass Transfer*, 48, pp. 5134–5149.
- [32] Incropera, F. P., Dewitt, D. P., 2002, *Fundamentals of Heat and Mass Transfer* 5th Edition, John Wiley & Sons, USA, pp. 141, Chap. 3.
- [33] Kuddusi, L., Cetegen, E., 2007, "Prediction of Temperature Distribution and Nusselt Number in Rectangular Microchannels at Wall Slip Condition for all Versions of Constant Heat Flux," *International Journal of Heat and Fluid Flow*, 28, pp. 777–786.
- [34] Chapman, S., Cowling, T. G., 1958, *The Mathematical Theory of Non-Uniform Gases*, Cambridge University Press, New York City, pp. 26, 89-91.
- [35] Hsu, Y. Y., 1962, "On the Size Range of Active Nucleation Cavities on a Heating Surface," *Journal of Heat Transfer*, 84, pp. 207-216.
- [36] Kandlikar, S. G., 2006, "Boiling," *Multiphase Flow Handbook*, C. T. Crowe, eds., Taylor & Francis, New York, pp. 6-16.
- [37] Gorenflo, D., Kenning, D., 2010, "Pool Boiling," *VDI Heat Atlas* 2nd Edition, P. Stephan, S. Kabelac, M. Kind, et. al., eds., Springer, New York, pp. 757-792.
- [38] Li, W., Wu, Z., 2010, "A General Correlation for Evaporative Heat Transfer in Micro/Mini-Channels," *International Journal of Heat and Mass Transfer*, 53, pp. 1778–1787.
- [39] Wang, H., Garimella, S. V., Murthy, J. Y., 2008, "An Analytical Solution for the Total Heat Transfer in the Thin-Film Region of an Evaporating Meniscus," *International Journal of Heat and Mass Transfer*, 51, pp. 6317–6322.
- [40] Wang, H., Garimella, S. V., Murthy, J. Y., 2007, "Characteristics of an Evaporating Thin Film in a Microchannel," *International Journal of Heat and Mass Transfer*, 50, pp. 3933–3942.
- [41] Ha, J. M., Peterson, G. P., 1996, "The Interline Heat Transfer of Evaporating Thin Films Along a Micro Grooved Surface," *Journal of Heat Transfer*, 118, pp. 747-755.

- [42] Butt, H. J., Cappella, B., Kappl, M., 2005, "Force Measurements with the Atomic Force Microscope: Technique, Interpretation and Applications," *Surface Science Reports*, 59, pp. 1–152.
- [43] Shooshtari, A., 2013, "Introduction to Boiling," *ENME765 Thermal Issues in Electronic Systems*, University of Maryland, College Park.
- [44] Mosyak, A., Rodes, L., Hetsroni, G., 2012, "Boiling Incipience in Parallel Micro-Channels with Low Mass Flux Subcooled Water Flow," *International Journal of Multiphase Flow*, 47, 150–159.
- [45] Zeng, X., Chyu, M. C., Ayub, Z. H., 2001, "Experimental Investigation on Ammonia Spray Evaporator With Triangular-Pitch Plain-Tube Bundle, Part II: Evaporator Performance," *International Journal of Heat and Mass Transfer*, 44, pp. 2081 – 2092.
- [46] Ribatski, G., Jacobi, A. M., 2005, "Falling-Film Evaporation on Horizontal Tubes—a Critical Review," *International Journal of Refrigeration*, 28, pp. 635–653.